Alma Mater Studiorum – Università di Bologna

DOTTORATO DI RICERCA IN

Biotecnologie Mediche

Ciclo XXIV

Settore Concorsuale di afferenza: 05/E1

Settore Scientifico disciplinare: BIO/10

SPECTROSCOPIC STUDY OF BIOCERAMICS FOR ENDODONTICS AND ORTHOPAEDICS

Presentata da: **Dr. Enrico Modena**

Coordinatore Dottorato **Relatore**

Prof.ssa Marialuisa Zerbini **Prof.ssa Paola Taddei**

Esame finale anno 2012

Contents

Part II

Part I

CHAPTER 1 - INTRODUCTION

1.1 Bioceramics

A widely accepted definition of the term ‘biomaterial’ was proposed in 1987 by the Consensus Conference of the European Society for Biomaterials [1]: ‘it is a non-viable material used in a medical device, intended to interact with biological systems’ for prolonged periods of time, exhibiting few, or any, adverse reactions.

With the aim to develop artificial materials and devices that can be used to replace various components of the human body, several types of materials, different in chemical composition and thus properties, have been developed so that many materials are often classified as biomaterials: metals, ceramics, polymers, glasses, carbons and composite materials. Different materials with different physico-mechanical, chemical and biochemical properties have been designed depending on the biomedical application. For each biomedical application, the material ensuring the best performance will be employed: it represents the most ‘biocompatible’ material. Therefore, a concept complementary to that of ‘biomaterial’ is ‘biocompatibility, defined as ‘the ability of a material to perform with an appropriate host response in a specific application’ [1]. The biocompatibility involves two aspects: a general aspect of bio-safety, which concerns the exclusion of deleterious effects of a biomaterial on the organism, as well as a specific aspect of bio-functionality which concerns the need for a material to not only be devoid of adverse effects, but also to elicit a beneficial response to the medical device.

These characteristics are strictly related to the body-implant interface, thus to the chemical/morphological structure of the involved surfaces.

Bioceramics represent an important class of biomaterials. The term ‘bioceramics’ refers to biocompatible ceramic materials used for repair and replacement of diseased and damaged parts of the musculoskeletal system.

The insertion of a synthetic material within the human body triggers an interaction between the implant and the surrounding tissues involving also the immune system. On the basis of the tissue response to the implant surface three classes of bioceramics have been defined.

- Bioinert materials;
- Bioresorbable materials;
- Bioactive materials.

A bioinert material exhibits minimal interaction with the surrounding tissue (i.e does not initiate a response) when introduced in the human body.

Bioresorbable materials can be defined as materials that when implanted in the living system, start to dissolve (i.e. to be resorbed); they are progressively eliminated from the body via natural pathways being thus replaced by advancing tissues.

The term bioactive refers to a material, which upon being placed within the human body, interacts with the surrounding environment. The interaction between the bioactive implant and surrounding body fluids, results in the formation of a biologically active apatite layer on the implant that is chemically and crystallographically equivalent to the mineral phase of bone.

In Table 1.1 several examples of bioceramics are reported.

Type	Characteristics	Examples
Bioinert	Coexistence of the material without noticeable change. Isolation of the implant by formation of a fibrous capsule	Alumina, zirconia, pyrolitic carbon
Bioresorbable	Progressive dissolution of the material in the body fluid without toxicity and rejection	Tricalcium phosphate, calcium phosphate salts, bioglasses, porous hydroxyapatite
Bioactive	Direct interaction with the hard tissues by formation of a natural-like coating	High density hydroxyapatite, tricalcium phosphate, calcium silicates, bioglasses

Table 1.1: Types of Bioceramics

1.1.1 Bioactivity

Hydroxyapatite (HA), $Ca_{10}(PO_4)_6(OH)_2$, is the primary inorganic component of bone; it has a Ca/P molar ratio of 1.67 and a structure very similar to that of natural apatite.

Apatites are present in hard tissues such as bone, dentin and tooth enamel, while other calcium phosphates have been identified as constituents of pathological calcifications. These calcifications are metastable calcium phosphates in physiological conditions and tend to transform into more stable phases: around pH 7.2, in a supersaturated solution of Ca^{2+} and PO_4^{3-} ions, the first precipitated products are dicalcium phosphate dihydrate, DCPD ($CaHPO_4 \cdot 2H_2O$) and octacalcium phosphate $Ca_8(HPO_4)_2(PO_4)_4$, requiring a low formation energy. Hydroxyapatite can be formed as a result of these metastable precursors. [2-5]. As reported in Figure 1.1, the solubility of calcium phosphate decreases at increasing pH: HA represents the most stable phase over pH 4.8.

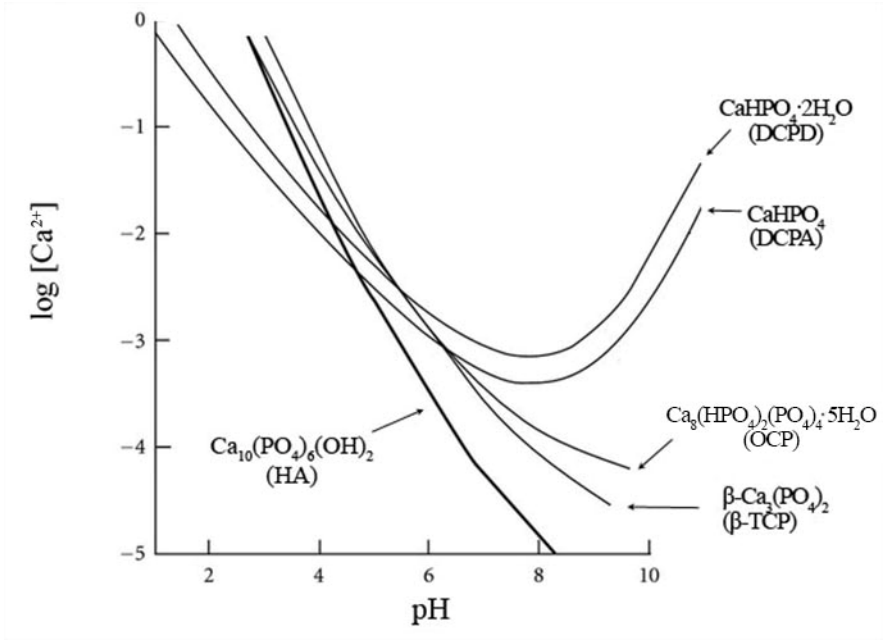

Figure 1.1: Solubility isotherms of calcium phosphates at 37°C, depending on pH in aqueous solutions. HA: Hydroxyapatite ($Ca_{10}(PO_4)_6(OH)_2$), β-TCP: β-tricalcium phosphate (β-$Ca_3(PO_4)_2$), OCP: octacalcium phosphate ($Ca_8(HPO_4)_2(PO_4)_4{\cdot}5H_2O$), DCPA: dicalcium phosphate anhydrous ($CaHPO_4$), DCPD: dicalcium phosphate dihydrate ($CaHPO_4{\cdot}2H_2O$).

Calcium phosphates are characterized by different Ca/P molar ratios. Actually, there are differences in composition and chemical properties between stoichiometric HA and biological apatites. Biological apatites show variable Ca/P values, i.e. in the 1.54 - 1.73 range, and often incorporate other ions like Na^+, K^+, Mg^{2+}, F^-, HPO_4^{2-}, CO_3^{2-}.

The most commonly reported precursors in the *in vivo* formation of HA are amorphous tricalcium phosphate (ATCP: $Ca_3(PO_4)_2$) and octacalcium phosphate (AOCP: $Ca_8(HPO_4)_2(PO_4)_4$) characterized by a Ca/P atomic ratio of 1.50 and 1.33, respectively..

Initially, these metastable amorphous phases are transformed into a poorly crystalline apatite that slowly increases its Ca/P ratio and crystallinity.

The deposition of calcium phosphates is a heterogeneous nucleation process triggered by biological macromolecules with a space-oriented mechanism, i.e. epitaxy. Epitaxy is the oriented overgrowth of bone mineral on certain well crystallized areas of the organic matrix. To obtain oriented-grown HA crystals, the organic substrates must be characterized by a specific superficial pattern to interact with HA. This role in bone and dentin is primarily played by collagen fibers. [6]

The HA structure (Figure 1.2) can be considered as a packed lattice of PO_4^{3-} and Ca^{2+} ions crossed by channels (whose walls are formed by metal ions) in which the OH^- ions are housed. The apatite structure allows ample isomorphic substitution. Carbonate is one of the most common substitutes. There are two types of carbonate substitution: in A-type carbonated apatites, the carbonate ion substitute the OH^- group in the channels, while in B-type carbonated apatites, the carbonate ion substitute the PO_4^{3-} group in the tetrahedral site.

B-type carbonated apatite represents the main mineral component of dentin and bone while an example of A-type substitution is the fluorapatite present in the tooth enamel.

The ion substitution in the lattice greatly influences the physical-chemical properties of apatites such as reactivity and solubility. The inclusion of carbonate groups produces an increment in apatite solubility and a decrease in thermal stability [7]. An opposite effect is induced by the substitution of OH^- anions by fluoride ions, which in low amounts stabilize the lattice structure as in enamel apatite that shows a higher acid resistance [8]. The distribution of carbonate ions in A- and B-type sites is strongly affected by fluoride ions.

A-type carbonate is always present in bone, but decreases with increasing bone fluoride content [9-12].

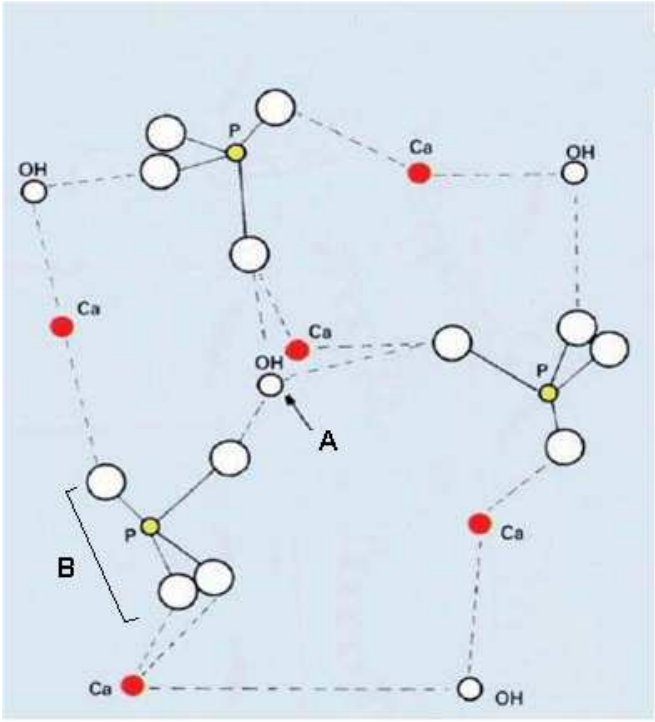

Figure 1.2: Structure of hydroxyapatite: A- and B-type substitutional sites are indicated.

Hydroxyapatite is biocompatible and osteoconductive, but not osteoinductive.

Osteoconduction is the process by which the osteogenic cells migrate to the surface of the biomaterial. The new bone formation occurs on the surface of the material, which should provide a suitable environment for the adhesion and the proliferation of bone cells and bone morphogenetic proteins [13]. Osteoinduction is the process by which stem cells are collected in a site for bone repairing and stimulate the beginning of the osteogenic differentiation (osteogenesis).

Thanks to these characteristics, HA constitutes an initial support with poor mechanical

properties, which allows its use as a filling in the case of bone defects or to coat metallic implants to improve the surface properties from the point of view of biocompatibility.

Hydroxyapatite has proven to be able to conduct the formation of bone tissue and to form chemical bonds with bone without the interposition of a fibrous layer (osteointegration). Several materials such as bioactive ceramics show the ability to form bone-like apatite on its surface when implanted in the living body.

It is believed that an essential requirement for an artificial material to bond to living bone is the formation of bone-like apatite on its surface. Apatite formation on bioactive ceramics in the living body has been shown to be reproducible in an acellular simulated body fluid (SBF) with ion concentrations approximately equal to those of human blood plasma (Table 1.2). The *in vivo* bone bioactivity of a material can be predicted by examining the apatite formation on its surface in SBF [14].

SBF solutions are widely used for *in vitro* assessment of the bioactivity of artificial materials also because the number of animals used and the duration of animal experiments can be reduced remarkably by using this method.

	Ions concentration (mM)							
	Na^+	K^+	Mg^{2+}	Ca^{2+}	Cl^-	HCO_3^-	HPO_4^{2-}	$H_2PO_4^-$
Human blood plasma	142.0	5.0	1.5	2.5	103.0	27.0	1.0	-
Standard SBF	142.0	5.0	1.5	2.5	148.8	4.2	1.0	-
DPBS	152.9	4.18	-	-	139.5	-	8.06	1.5
HBSS	141.6	5.8	0.81	1.27	144.7	4.17	0.336	0.44
DMEM	155.5	5.37	0.81	1.80	118.5	44.0	-	0.91

Table 1.2: Ion concentration in human blood plasma and other media used for bioactivity tests.

Once the apatite nuclei are formed, they spontaneously grow by consuming the calcium and phosphate ions from the surrounding fluid, since the body fluid is already supersaturated with respect to apatite.

Actually, the standard SBF is richer in Cl^- ion and poorer in HCO_3^- with respect to the physiological concentration. A modified SBF was introduced to correct this difference but the higher concentration of HCO_3^- introduced an excess of calcium carbonate precipitation [15]. For this reason a formulation with decreased Cl^- ion concentration with respect to the level of human blood plasma, and a HCO_3^- ion concentration equal to that of the corrected SBF was proposed [16].

Several types of SBF have been formulated exhibiting some differences in formulations and also cell culture media have been employed as fluids to test the apatite formation ability of biomaterials.

The Dulbecco's Phosphate-Buffered Saline (DPBS) is a calcium-free and phosphate-rich solution used as buffer in cell culture: phosphate groups are present both in HPO_4^{2-} form and $H_2PO_4^-$ form (8.06 and 1.5 mM, respectively). The absence of calcium ions allows toobtain natural-like phosphate mineral phase deposition only from calcium-releasing materials. The high amount of phosphate can mime the continuous replenishment of phosphate ions from tissue fluids.

Differently, Hank's Balanced Salt Solution (HBSS) contains calcium (1.27 mM) and lower amounts of phosphate ($H_2PO_4^-$ 0.44 mM and HPO_4^{2-} 0.336 mM). Sulphate anions are also present with a concentration of 0.81 mM. Using this medium, the bioactivity of materials that do not release calcium can be assessed.

Dulbecco's Modified Eagle's Medium (DMEM) is a cell culture medium containing salts (calcium chloride, potassium chloride, magnesium sulphate, sodium chloride, sodium bicarbonate and monosodium phosphate) and rich in vitamins (folic acid, nicotinamide, riboflavin and B-12), amino acids and glucose. DMEM supplemented with 10% of foetal bovine serum (FBS) allows to test the materials in solutions of increased complexity containing ionic concentrations similar to blood plasma and proteins common to blood.

In this thesis, commercial media were selected for bioactivity tests because they are standardised and readily available on the market.

1.2 Dental Materials

Bioceramics in dentistry are utilized in a wide range of dental applications both in implants, restoration procedures and endodontic treatments.

The term dental ceramics usually defines a general class of materials that include endodontic cements, glasses (porcelains), structural ceramics (alumina and zirconia) and glass-ceramics used for different applications as inlays and onlays, crowns and bridges, metal implant fixture abutments and ceramic implants. Their aesthetic quality represents one of the key factors that make dental ceramics suitable for tooth restoration. In order to achieve a high functional device, the excellent aesthetic properties of porcelains must be combined with structural support provided by high-strength ceramics (alumina) for use in crowns or bridges. Structural ceramics suffer from a lack of translucency and must be of white colour to be considered. Alumina and zirconia-based structural ceramics are utilized as crowns, cores and bridge frameworks, but require the application of an aesthetic veneering ceramic for clinical use in replacement of tooth structure.

Endodontic materials constitute an important family of bioceramics used in dental restoration. Endodontics is the branch of dentistry that deals with diseases of the tooth root, dental pulp, and surrounding tissues.

A simplified structure of a tooth is shown in Figure 1.3. The outer layer consists of enamel, which is a hard crystalline shell of fluorapatite. It is resistant to grinding and abrasion and to acid and chemical attacks during the process of digestion, but the entire basic tooth structure is not made up of enamel, because enamel is very rigid and brittle.

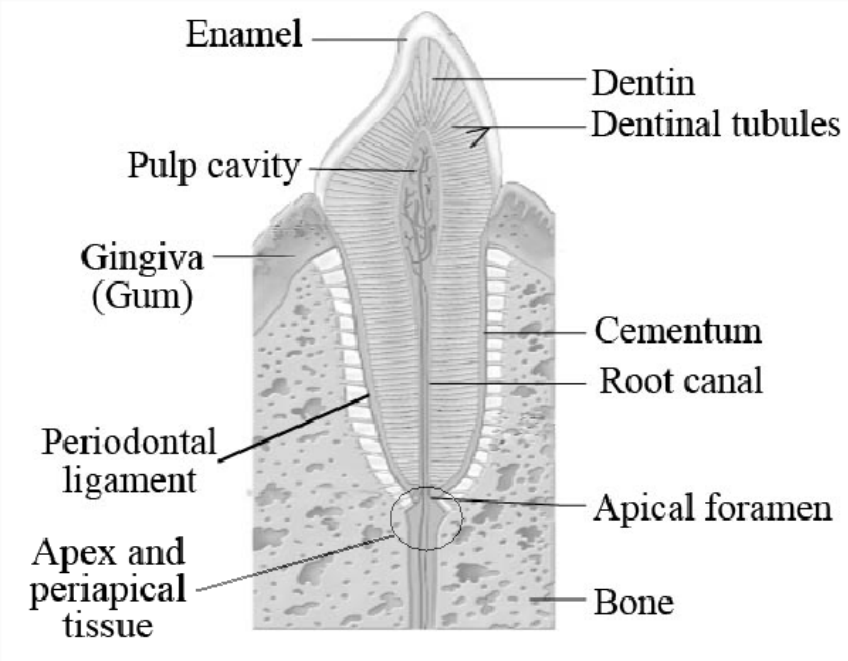

Figure 1.3: Schematic tooth structure

The enamel is a thin shell protecting the rest of the basic tooth structure from the outside environment. Dentin tubules are located inside the enamel shell which is continuous with the root structure. Dentin is a complex system composed of 70% by weight of hydroxyapatite integrated in an organic matrix of collagen (20%). A tenth of its weight is water. The entire inner part of the tooth develops over time with millions of tubules that run throughout the entire inner part of the tooth, from the inner blood flow to the outer environment of the tooth structure. These tubules carry calcium and other minerals from the blood delivery system into the large surface area of the tooth root for the root growth and development. The pulp is located in the centre of the tooth, i.e. in the root canals. Pulp includes connective tissue, nerves and blood vessels that nourish the tooth.

If injury or disease damages the pulp, it cannot repair itself and bacteria can infect the pulp causing its death. If the tooth is not treated, an abscess can form at the tip of the root or otherwise the bone anchoring the tooth in the jaw can be harmed. Without treatment, the

tooth may require extraction, but in several cases, injured or diseased teeth can be saved through endodontic treatments avoiding removal.

Root canal treatment consists in the elimination of the infection of pulp tissues followed by the protection of the decontaminated tooth from future microbial penetration.

.

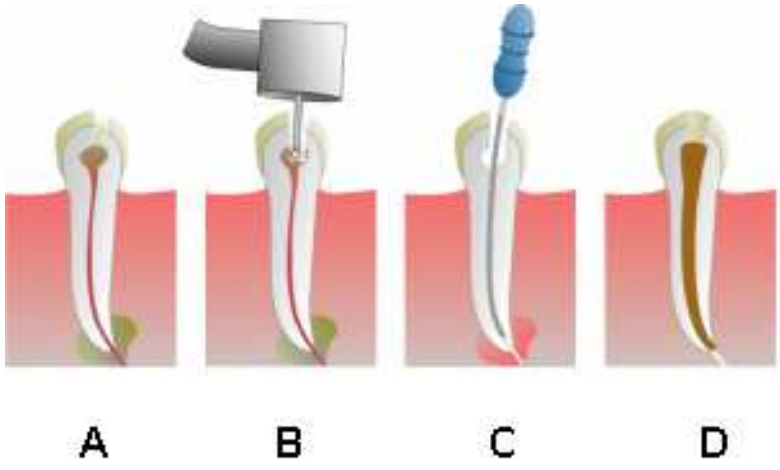

Figure 1.4: Schematic representation of the phases of root canal treatments.

As shown in Figure 1.4 the restoration of a damaged tooth (A) is performed firstly removing the decayed tooth material (B). After cleaning (C), the pulp chamber and the root canal are filled with a filling material (D).

1.2.1 - Filling materials

Because of the complexity of root canal systems, a filling material should possess several characteristics, as proposed by Grossman in 1982 (ideal characteristics) [17]:

1. It should be tacky when mixed to provide a good adhesion to the canal wall when set.
2. It should make a hermetic seal.
3. It should be radiopaque so that it can be visualized on the radiograph.
4. The powder particles should be very fine so that they can easily mix with the liquid.
5. It should not shrink upon setting.
6. It should not discolour tooth structure.
7. It should be bacteriostatic or at least not encourage bacterial growth.
8. It should set slowly.
9. It should be insoluble in tissue fluids.
10. It should be well tolerated by the periapical tissue.
11. It should be soluble in common solvents if it is necessary to remove the root canal filling.

A wide variety of materials are used as fillings, very different in chemical composition, physical and technological properties. The materials used for endodontic filling procedures are listed in Table 1.3.

Filling materials can be metallic or non-metallic and are used to restore diseased or damaged teeth to health and function. These materials have been greatly improved, although a universally ideal restorative material has not yet been developed. The corrosive nature of saliva and the expansion and contraction of tooth structure with changes in temperature make great demands upon filling materials as well as the stress brought by

masticatory forces. Filling materials must be biocompatible with living tissues. Biocompatibility of filling materials refers to their coexistence with the biological equilibrium of the tooth and body systems. Since fillings are in close contact with mucosa, tooth, and pulp, biocompatibility is fundamental. Common problems with some of the current dental materials include chemical leakage from the material, pulpal irritation and, less commonly, allergy. Some of the by-products of the chemical reactions occurring during material hardening need to be considered.

Materials	Main composition
Amalgam	Mercury, silver, tin, copper
Gutta-percha	Gutta-percha, zinc oxide, metals, colophonium, pigments
Thermoplastic polymers	Polyester, bioactive glass, bismuth oxychloride, barium sulphate
Zinc oxide eugenol	Zinc oxide, eugenol, bismuth, barium
Polyketones	Zinc oxide, propionylacetophenone, vinyl copolymer
Epoxy resins	Bisphenol-A diglycidylether, bismuth oxide/zirconia
Calcium hydroxide	$Ca(OH)_2$, colophonium, different oxides, salicylate-based activator
Calcium Phosphate Cement (CPC)	Tetracalcium phosphate and dicalcium phosphate
Composites	Bis-GMA, UDMA, HEMA, TEGDMA, silica and alumina, glasses, calcium phosphate, $Ca(OH)_2$, barium sulphate
Glass ionomer cements (GIC)	Calcium aluminosilicate glass, polyacrylic acid
Resin modified GIC	Fluoraluminosilicate glass, polyacrylic acid, methacrylate (HEMA) monomer
Mineral Trioxide Aggregate (MTA)	Calcium/Aluminum silicates, bismuth oxide

Table 1.3: Filling materials and their main composition. The abbreviations reported refer to: bisphenol A-glycidylmethacrylate (Bis-GMA), urethane dimethacrylate (UDMA), 2-hydroxyethyl methacrylate (HEMA), and triethyleneglycoldimethacrylate (TEGDMA).

If used in a visible region of the mouth, the materials must also be aesthetically pleasing. Filling materials, used when and where indicated, help to ensure the placement of a successful restoration and preservation of the tooth.

Filling materials should enhance periodontal tissue regeneration around the margins of fixed prosthetic restorations, reducing the marginal gap between the tooth and the fixed prosthesis; this gap can be responsible for cement dissolution, secondary caries and eventually the failure of the restoration. In any repair of a tooth with permanent restorative materials, the interface is always a sensitive region and the good marginal adaptation (i.e. the degree of proximity and interlocking of the filling material to the wall of the tooth cavity) provided by the composite material represents a great advantage in dental restorations.

It is desirable for a filler to have good adaptation at the interface between the material and tissue in order to stimulate the adhesion and prevent micro-leakage and ingress of bacteria

A good marginal adaptation of the filling material can be reached in several modes: it can be achieved by the formation of a bond between the tooth mineral phase and the filler through the formation of an apatite deposit (bioactivity) or by the binding of the organic matrix of dentin with a resin compound present in the formulation of the material. The use of materials as bioactive glasses, glass ceramics and wollastonite as filling materials has been suggested since they have shown extraordinary performance to bind hard tissues through the formation of an apatite mineral phase as an interfacial layer [14, 18-19]. Furthermore, nearly complete conversion to apatite-like mineral was observed with the degradation of β-tricalcium phosphate (TCP) [20].

1.2.1.1.Root-end filling materials

Different types of materials have been proposed and clinically used as root-end fillings, such as amalgam, zinc-oxide cements, glass-ionomer cements (GIC), calcium phosphates, composites and MTA.

Most endodontic failures occur as a result of leakage of irritants from pathologically involved root canals. When non-surgical attempts prove unsuccessful or are contraindicated, surgical endodontic therapy is needed to save the tooth. The root-end filling material should provide an apical seal to an otherwise unobturated root canal or improve the seal of existing root canal filling material. [21]

The ideal healing response after periradicular surgery is the re-establishment of an apical attachment apparatus and osseous repair. The deposition of cementum on the cut root face is considered a desired healing response and a prerequisite for the reformation of a functional periodontal attachment [22-23]. The formation of an apatite deposit on the surface of the root-end filler (bioactivity) can help the healing through the direct bonding of the mineral phase of the tooth.

1.2.2 Metal Trioxide Aggregate (MTA)

Mineral trioxide aggregate (MTA) was developed and recommended initially because existing root-end filling materials did not fulfill completely the ‘‘ideal’’ characteristics and was then proposed for different endodontic applications. The first calcium silicate cement (Mineral Trioxide Aggregate, MTA) was developed in the 1990s [24]. The first patented material was composed of type 1 Portland cement with a 4 : 1 addition of bismuth oxide added for radiopacity and was marketed as ProRoot MTA.

MTA is available in two different forms: grey (GMTA) and white (WMTA) . The first MTA developed was grey, but because of the potential discoloration of GMTA, WMTA was introduced. WMTA contains lower amounts of iron, aluminum, and magnesium than in GMTA [25].

White Portland cements (PC) are principally composed of alite (tricalcium silicate, $3CaO•SiO_2$), belite (dicalcium silicate, $2CaO•SiO_2$) and lower amounts of tricalcium aluminate ($3CaO•Al_2O_3$) and calcium sulphate ($CaSO_4$). Grey PC also contains a ferrite phase (tetracalcium aluminoferrite $4CaO•Al_2O_3•Fe_2O_3$). Minor amounts of metalloids (As) and transition metals (Cr and Mn) may be present in either materials [26].

The similarity between MTA and PC as regards the basic elemental composition has been reported using several investigation techniques as inductively coupled plasma atomic emission spectroscopy (ICP-AES) [27] and X-Ray micro analysis **[**28]. The range of crystal sizes observed in WMTA is distinctly smaller than those observed in white PC. The main compositional differences between MTAs and PC are the lack of potassium and the presence of bismuth oxide in the former.

The most important characteristic of MTA is its ability to set in presence of water or moisture that allows its use in contact with blood or body fluids.

The hydration of PC and MTA involves a number of chemical reactions, which take place simultaneously [29-31].

In water, calcium silicates undergo hydrolysis producing calcium hydroxide (portlandite) and a less basic calcium silicate hydrate (CSH).

The alite and belite reactions are as follows:

$2(3CaO{\bullet}SiO_2) + 6\ H_2O \rightarrow 3CaO{\bullet}SiO_2{\bullet}3H_2O + 3\ Ca(OH)_2$

$2(2CaO{\bullet}SiO_2) + 4\ H_2O \rightarrow 3CaO{\bullet}SiO_2{\bullet}3H_2O + \ Ca(OH)_2$

The resulting hydrate is poorly crystallized and produces a porous solid, which may be defined as a rigid gel. The silicate hydrate gel has typical Ca/Si ratios of approximately 1.5 which is lower than the 3 : 1 ratio in tricalcium silicate. The excess calcium is precipitated as calcium hydroxide. The presence of calcium hydroxide makes the hydrated cement highly alkaline [32] and leads to a calcium release in the surrounding environment [33**].**

Tricalcium aluminate reacts with water in the presence of gypsum ($CaSO_4{\bullet}2H_2O$) resulting in the formation of a high-sulphate calcium sulphoaluminate known as ettringite ($3CaO{\bullet}SiO_2{\bullet}3CaSO_4{\bullet}32H_2O$). Ettringite continues to form until all the sulphate ions are used up in the reaction. Once depleted, further hydration of tricalcium aluminate results in the conversion of ettringite into a low-sulphate sulphoaluminate called monosulphate ($3CaO{\bullet}SiO_2{\bullet}CaSO_4{\bullet}12H_2O$).

Industrially, gypsum is added to PC to retard the setting time of the cement clinker. Without gypsum, silicates hydration would cause PC to set almost immediately after

adding water [34]. Less hydrated forms of calcium sulphate such as anhydrite ($CaSO_4$) and hemi-hydrate ($CaSO_4 \bullet 1/2H_2O$) are present in MTA formulations and are characterized by a higher rate of hydration. The extended setting time represents one of the main disadvantages of MTA.

Bismuth is present both as bismuth oxide unreacted filler in the hydrated MTA and also forms part of the structure of the amorphous CSH phase. [35**]**

MTAs are successfully used to repair root perforations that adversely affect the tooth prognosis: the inadequacy of the previously developed repair materials has been a contributing factor to the poor outcome of the repair procedure [36-37].

MTA also resists bacterial leakage and may provide protection for the pulp, allowing repair and continued pulp vitality in pulp capping procedures (i.e. in the covering of an exposed dental pulp with a material that protects it from external influences), when used in combination with a sealed restoration [38].

It has been also demonstrated that MTA conceivably could replace calcium hydroxide as the material of choice for pulpotomy procedures [39]. Thanks to the release of hydroxyl ions in aqueous solutions, calcium hydroxide shows anti-microbial properties: several bacterial species commonly found in infected root canals are unable to survive in the highly alkaline environment and are eliminated in a short period [40]. A basic pH also activates alkaline phosphatase that plays an important role in hard tissue formation [41].

Because of its success as a root end filling material, some investigators have also suggested the use of MTA to obturate the entire root canal system.[42-44]

1.2.3 Composite Materials

Nowadays a wide use of tooth-coloured materials is made in restorative dentistry, such as composites, GIC, compomers, giomers and sealants. A composite material is generally defined as composed of two or more distinct phases. “Dental composites” consist of a polymerisable resin base containing a ceramic filler. From a strictly chemical point of view, also other classes of materials represent “composites”: GIC are a combination of silicate and polyacrylate cement systems; compomers and giomers combine some of the benefits of composites (aesthetics and handling characteristics) and GIC (long-term fluoride release); giomers are resin-based and contain pre-reacted glass-ionomer particles. The particles are made of fluorosilicate glass previously reacted with polyacrylic acid prior to being incorporated into the resin [45-47].

The composites combine the mechanical resistance of the inorganic phase (filler) with the adhesion ability of the resin matrix. This combination also exhibits low polymerization shrinkage and low coefficients of thermal shrinkage, which allows them to be placed in bulk while maintaining good marginal adaptation.

These materials show excellent biocompatibility properties, durability and high resistance to wear and distortion; moreover, their tooth coloured appearance is more cosmetically appealing.

The filler materials are of inorganic nature: silica glass (SiO_2), alumina glass (Al_2O_3), aluminium silicate glasses, calcium phosphates are commonly used. The combination of fluorine containing components assures a source of fluoride ions. Fluoride plays an important role in tissue mineralization supplying clinical benefits. The hydroxyl ions of HA are readily substituted by fluoride ions. The fluoride ion is smaller than the hydroxyl

and allows a more stable packing of the crystal lattice forming fluorapatite. The cariostatic effect of fluoride is due to the this structural stabilization that enhances the resistance to acid attacks of enamel fluorapatite. Fluoride can remineralize enamel and softened dentin reducing caries formation [48].

The radiopacity of the composites is obtained adding to the filler formulation barium, strontium, lithium or ytterbium compounds.

The matrix is composed of organic resins. A wide variety of different aromatic and diacrylate monomers and oligomers is used, such as bisphenol A-glycidylmethacrylate (Bis-GMA), 2-hydroxyethyl methacrylate (HEMA), triethyleneglycoldimethacrylate (TEGDMA) and urethane dimethacrylate (UDMA).

The incorporation of the filler particles is assured by their coating with silane coupling agents (such as trialkoxysilane) providing covalent coupling between the filler and the resin matrix. The silane molecules bind to the filler particles as well as to the resin monomer during polymerization of the composite.

For most composite systems in current use, light energy (ultraviolet or visible light) is used for polymerization. Depending on the curing method, various polymerisation initiators and accelerators are required. Initiators for light curing systems are normally camphorquinone used in conjunction with an aliphatic tertiary amine as accelerator.

After the preparation of a cavity in dentin, a thin layer called smear layer is formed; the removal of the smear layer by the use of acids (conditioner) also removes a thin layer of apatite, while does not damage the collagen fibers. The resin penetrates through these fibers to form, after polymerization, a hybrid layer made of resin and collagen which

ensures a micromechanical bond [49**]**. This interaction allows to obtain excellent adhesion properties.

Moreover, demineralized dentin remineralizes when placed in solutions that are metastable with respect to HA that does not spontaneously precipitate. The ability of dentin to remineralize under these conditions was attributed to the abundant availability of reactive amino groups in dentin collagen that induce heterogeneous precipitation [50].

An extra amount of calcium should lead to a supersaturation with respect to HA in the region close to the material-tissue interface, The excess of calcium can help the deposition of new mineral tissue supporting dentin remineralization.

Combining the good marginal adaptation with the dentin remineralization potentiality, the development of composite materials containing calcium-releasing fillers, represents a very interesting attraction in the field of remineralization treatments.

1.3 Hip joint Prostheses

As a result of the progressive ageing of the population, degenerative joint disease represents an increasing problem for society. The degeneration of joints often makes surgical repair or replacement necessary to allow patients to return to a healthy and functional lifestyle.

Arthritis (i.e. joint inflammation) is the most diffuse cause of joint replacement procedures. There are several forms of arthritis, most of which affect the joints of the body. One of the most common form is osteoarthritis that is the degeneration of the articular surface of the joint that leads to the consumption of the articulating cartilage leaving exposed the underlying bone. Exposed bone results in a painful joint during movements and weight bearing.

Rheumatoid arthritis and avascular necrosis (injury and loss of blood supply to the bones, respectively) are other joint issues that produce similar symptoms .

Osteoarthritis represents the primary diagnosis leading to joint replacement especially over-65 aged patients. In the light of the population ageing, a growth of the market for joint replacement products is expected for the future.

Total hip arthroplasty (THA), or total hip replacement (THR), is a surgical procedure to replace the hip joint with an artificial prosthesis. When a hip replacement is performed, the arthritic, damaged hip joint is removed. The ball-and-socket hip joint is then replaced with an artificial implant.

As shown in Figure 1.5 a prosthesis for THA consist of four components:

- the stem: a stiff prosthesis inserted into the femoral canal;
- the head: a ball on the top of the femoral stem neck;
- the cup: an acetabular component or acetabular shell fixed into the acetabulum (the concave surface of the pelvis);
- the liner: the inner material placed inside the metal cup

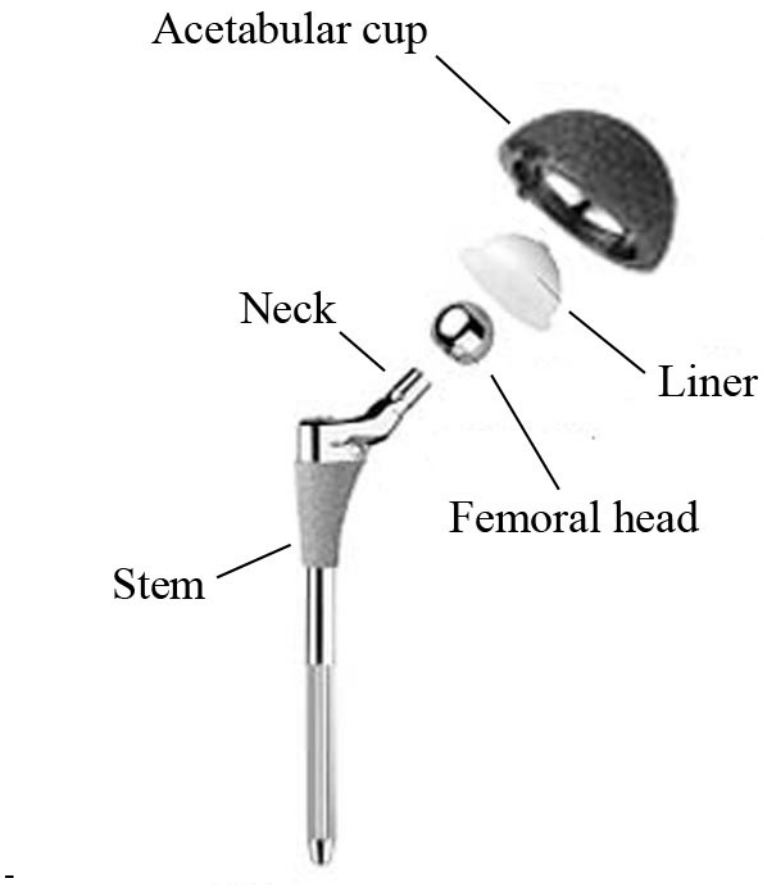

Figure 1.5: Components of a THR prosthesis

Several types of biomaterials have been used for this surgical procedure. Metal-on-plastic THR was introduced in the 1960s. It consisted of a femoral head of a metal alloy (usually

cobalt-chrome alloy or stainless steel) combined with an ultra-high molecular weight polyethylene (UHMWPE) liner that however did not have the sufficient strength for weight-bearing joint replacements and showed the problem of PE wear debris. Metal-on-Metal (MOM) joints were developed to improve wear rates and joint strength. Ceramic-on-ceramic (COC) couplings represented an alternative choice: alumina and, more recently, zirconia ceramics and their composites have been used in THR to overcome the problems related to the production of PE wear debris [51].

1.3.1 Alumina ceramics

Physical and mechanical properties

Many applications of ceramics are based upon their unique physical, mechanical and thermal properties. Density, biocompatibility, strength and wear resistance are the main important issues for their biomedical applications [52].

Alumina consists primarily of aluminium oxide (Al_2O_3). High-purity alumina (99.99%) has been introduced as an alternative to metal alloys for orthopaedic surgical applications such as THR. Alumina exhibits high hardness, low friction and excellent wear and corrosion resistance; therefore, it represent an ideal material for replacing articulating surfaces in orthopaedic applications.

Metals under load show the movement of defects or dislocations through their structure: this property makes them easily modelled by casting from molten state. As most ceramics,

alumina is intrinsically hard, due to its strong chemical bonds: as a consequence, the enormous lattice resistance to the motion of dislocations avoids the possibility of shaping ceramics by melting and casting. This hardness and strength of ceramics can be exploited in articulating joints in orthopaedic applications where wear resistance is required.

Fracture toughness is a property that describes the ability of a material containing a crack to resist fracture. Most ceramics, including alumina, have values of fracture toughness significantly lower of more ductile materials as metals.

Thanks to the strong lattice bonds, alumina ceramics show very high melting temperature: for this reason, the production of alumina ceramics can only be achieved with high-temperature sintering. The sintering process consists in heating ceramic powders to about two-thirds of their melting temperature. In this condition, particles bond together to form necks between the particles, which subsequently reduce the surface area and lead to consolidation of the powders.

Medical-grade alumina

A medical grade bioceramic should be bioinert in the human body offering a high resistance against corrosion and wear [53]. The condition to obtain this characteristic is the use of a high-purity oxide ceramic, based on purified raw materials that are free of impurities (e.g. silicates and alkaline oxides normally less than 0.5 wt%). With regards to the mechanical properties, the material should not deform when loaded in physiological conditions. The mechanical strength of the ceramic components strictly affects its safety. The development of implant materials deal with the improvement of all properties that are correlated with mechanical strength.

Hot isostatic pressing (HIP) is a manufacturing process used to increase the density of many ceramic materials. The HIP process subjects the ceramic to both elevated temperature and isostatic gas pressure in a high pressure containment vessel.

HIP technology applied subsequently to the process of sintering allows to obtain bioceramics with improved mechanical strength and density.

Moreover, a high surface finish is an important requirement for the articulating surfaces such as the femoral head and liner. If the ceramic material is homogeneous, has no porosity and its microstructure consists of small fine grains, an excellent surface finish can be achieved. Magnesium oxide (MgO) is used as sintering aid in manufacturing process of alumina ceramic.

The required properties of medical-grade alumina used in orthopaedics are stated in the standard ISO 6474 introduced for the first time in 1980 and afterwards implemented. This standard lists the requirements that an alumina ceramic must satisfy to be used in biomedical devices: the principal parameters considered are purity, allowed constituents, compression strength, wear resistance, fatigue strength, bulk density, grain size and flexural strength.

A standard regulation is necessary to ensure the production of a high-quality material for biomedical applications. The physical-chemical and mechanical requirements serve as criteria for a high-purity, consistent product suitable for implantation in the human body. The ISO 6474 and further upgrade provide also specifications for biocompatible grades of alumina for use in physiological environments.

Alumina bioceramics in orthopaedics

Thanks to their high hardness, low friction coefficient and excellent corrosion resistance, alumina bioceramics exhibit a very low wear rate at the articulating surfaces in orthopaedic applications. Moreover, alumina has the ability to be polished obtaining a high surface finish.

The microstructure of medical-grade alumina is characterized by a narrow grain-size distribution with a very small grain size (less than 7 µm) that allows to inhibit static fatigue and slow crack growth under load conditions. The average grain size of current medical-grade alumina is 1.4 µm, and surface finish is usually controlled to a roughness of less than 0.02 µm.

Alumina was introduced in THA more than 40 years ago to reduce the wear rate of the implants. A decrease in wear by 25–30% was noted when comparing alumina/UHMWPE couplings to metal/UHMWPE couplings both in hip simulator tests and clinical results [54]. Moreover, the nearly elimination of wear using alumina/alumina combinations in THA was observed in a hip simulator test [55].

Alumina-on-alumina bearings in total hip replacements have been successfully used since the early 1970s. Since their introduction [56], more than 2.5 million femoral heads and nearly 100000 liners have been implanted worldwide. The excellent tribologic properties of alumina and its low debris generation make it ideal to reduce osteolysis. [57].

A comparative study on ceramic-on-ceramic and metal-on-polyethylene bearing implants has reported that alumina ceramics perform as well as metal-on-polyethylene coulplings in clinical scores, but fewer revisions and less osteolysis characterize patients with implanted

ceramic bearings[58]. As a conclusion, the use of alumina ceramic bearings as a safe option for younger and more active patients has been proposed.

With alumina-on-alumina THA, minimal wear rates and limited osteolysis can be expected up to twenty years after the operation, provided that sound acetabular component fixation is obtained [59].

1.*3.2 Zirconia ceramics*

The zirconia ceramics were introduced in THA to solve the problem of alumina brittleness and the consequent potential failure of implants [60].

In the 1970s it was demonstrated that zirconia exhibits a transformation toughening mechanism (see below) acting to resist crack propagation [61].On the other hand, phase transformation may also occur at the surface of the implants in the presence of body fluids, leading to a progressive degradation of the material.

The clinical results reported before 2000 were satisfactory exhibiting low failure rates: in 2001 a high number of femoral heads failed in a very short period stimulating retrieval analysis that showed the occurrence of *in vivo* ageing and constitutes the main issue for the lifetime of zirconia implants [62].

Recently the development of orthopaedic implants is focused on materials alternative to pure zirconia such as alumina–zirconia composites.

1.3.3 Transformation toughening mechanism

To explain the mechanical properties and durability of zirconia ceramics, their crystallographic structure has to be considered. The so-called transformation toughening mechanism is responsible for the high mechanical properties and sensitivity to low-temperature degradation of zirconia ceramics: it is based on the evolution from one metastable polymorph (tetragonal phase) to the stable one (monoclinic phase).

Three crystal phases of pure zirconia (ZrO_2) exist at atmospheric pressure: monoclinic phase is stable at low temperatures (below 1170 °C); tetragonal and cubic phases are stable at higher temperatures.

The latter polymorphs can be stabilised at room temperature by the addition of oxides.

Zirconia can be stabilised under two different forms depending on the stabilizer solubility at high temperature:

1) The so called partially stabilised zirconia (PSZ) is obtained by the addition of slightly soluble stabilizers as MgO or CaO that at room temperature formed a precipitated system. Magnesia partially stabilised zirconia (Mg-PSZ) was the first zirconia introduced in orthopaedics.

2) The so called tetragonal zirconia polycrystal (TZP) is obtained by the addition of soluble stabilizer as ceria (Ce-TZP) or yttria (Y-TZP) inducing the formation at high temperatures of a solid solution that was retained at low temperature. Nowadays, only 3Y-TZP (stabilised with 3 mol% Y_2O_3) is used in clinical applications.

The tetragonal phase retained at room temperature is metastable and can convert to the monoclinic phase (t-m tranformation): this transition is accompanied by a volume expansion (4%).The development of zirconia as toughened ceramic is based on the metastable nature of the tetragonal polymorph. 3Y-TZP ceramics were introduced in

orthopaedics to overcome the problem of alumina brittleness and especially its sensitivity to delayed failure.

The mechanical strength of zirconia is improved by the t-m transformation at the vicinity of an advancing crack. The large stresses appearing around a crack lead to the t–m transformation and the stress field associated with the volume expansion due to the conversion opposes the tensile applied stress field at the crack tip preventing its propagation.

1.3.4 Low temperature degradation

A negative consequence of the tetragonal-monoclinic phase transformation is ageing. The presence of water molecules as well as body fluids on the surface of zirconia implants can progressively convert tetragonal phase to monoclinic polymorph: the process is defined low temperature degradation [63-64].

Even if ageing is faster at relatively higher temperature (250°C) it occurs even at physiological temperature. Water is able to penetrate the zirconia lattice during exposure to a humid atmosphere [65] leading to a lattice contraction [66], which results in the formation of tensile stresses in the surface grains that destabilise the tetragonal phase. These stresses trigger the transformation of superficial grains that represent the so-called nucleation stage. The process proceeds by the stress propagation to the neighbours induced by the volume expansion that can cause microcracking offering a path for the water to penetrate the material (Figure 1.6). The overall transformation can be considered as a nucleation and growth process described by the Mehl–Avrami– Johnson model [67]: this model will be discussed in chapter 10.

The ageing process influences the long-term performance of zirconia implants since it is associated with roughening and micro-cracking.

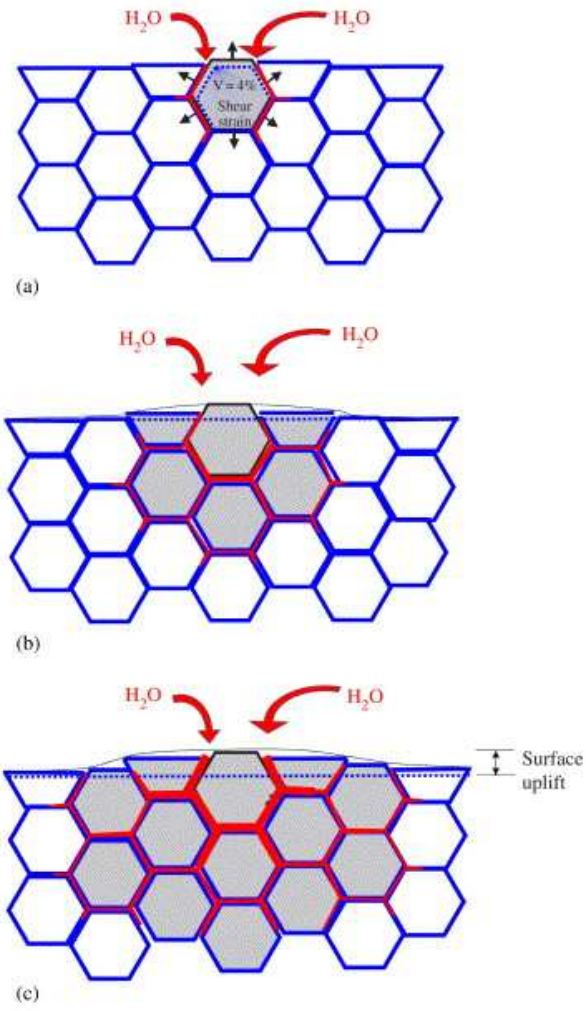

Figure 1.6: "Scheme of the ageing process (a) Nucleation on a particular grain at the surface, leading to microcracking and stresses to the neighbours. (b) Growth of the transformed zone, leading to extensive microcracking, surface roughening and (c) uplift. Transformed grains are grey. Red path represents the penetration of water due to microcracking around the transformed grains.". (from Chevalier 2006 **[**62**]**)

The transformation of the surface induces volume expansion that produces grains uplift and then roughening. The wear performance of hip joint heads is compromised by roughening since it will increase the wear rate of the coupled part of the implant. The combined effect of surface microcracking and wear can also lead to pull-out of zirconia grains.

Moreover, micro-cracking around the transformed zone generates defects that may grow until they reach a threshold size that can induce slow crack propagation and a consequent fracture of the prosthesis.

The morphology and microstructure of the implants (i.e. density, grain size and homogeneity) hardly influence the ageing.

The production of implants characterized by high density is a fundamental requirement to limit ageing phenomena. Low density and porous ceramics allow the penetration of water molecules to the bulk of the material: since the internal surfaces (pores and cracks) are exposed to water contact, internal ageing occurs and the material rapidly loses its cohesion leading to a worsening of the mechanical properties.

The important influence of grain size on ageing and the positive effect on low temperature degradation rate has been demonstrated [68]. On the other hand, small grains influence negatively the mechanical properties leading to a lower toughness and slow crack propagation threshold, due to the lower efficiency of the phase transformation toughening.

In this thesis three successive generations of retrieved ceramic femoral heads were studied with the aim to investigate at molecular level the *in vivo* wear mechanisms.

The retrievals have been obtained from the archive of Istituto Ortopedico Rizzoli in Bologna thanks to the collaboration with Dr. Saverio Affatato of the Laboratorio di Tecnologia Medica of the Institute.

1.4 References

1. D.F. Williams. Proceedings of a Consensus Conference of the European Society for Biomaterials. Elsevier: New York, 1987

2. E. D. Eanes, J. D. Termine, A. S. Posner. *Clin Orthop.* 1967, **53**, 223.

3. J. D.Termine, A. S. Posner. *Science* 1966, **153**, 1523.

4. J. D. Termine, A. S. Posner. *Calcif. Tissue Res.* 1967, **1**, 8.

5. W. E. Brown, *Clin. Orthop.* 1966, **44**, 205.

6. C. Rey, M. Freche, M. Heughebaert. *Bioceramics,* 1991, **4**, 57.

7. F.C.M. Driessens, J.W.E.van Dijk, J.M.P.M. Borggreven, *Calcif. Tissue Res.* 1978, **127**, 26.

8. Y. Chen, X. Miao, *Biomaterials* 2005, **26,** 1205.

9. M.D. Grynpas, C.Rey. *Bone* 1992, **13,** 423.

10. R. A. Young, M. L. Bartlett, S . Spoonerm, P . E. Mackie. *J. Biol. Phys.* 1981, **9**, 1.

11. A. A. C ampbell, M. Lore and G. H. Nancollas. *Colloids Surf.* 1991, **54,** 25.

12. N. Okazaki, Y. M. oriwaki, T. Aoba, Y. Doi And J. Takahashi. *Caries Res*. 1981, **15**, 477.

13. T. Albrektsson, C. Johansson. *Eur. Spine J.* 2001, **10**, S96

14. T. Kokubo. *Biomaterials* 1991, **12,** 155.

15. A. Oyane, H.M. Kim, T. Furuya, T. Kokubo, T. Miyazaki, T. Nakamura. *J. Biomed Mater. Res.* 2003, **65A,** 188.

16. H. Takadama, M. Hashimoto, M. Mizuno, T. Kokubo. *Phos Res Bull*, 2004, **17,** 119.

17. L. Grossman. Obturation of root canal. L. Grossman (Ed.), Endodontic Practice (10th ed), Lea and Febiger, Philadelphia p. 297. 1982.

18. L. Hench. *J Mater Sci: Mater Med*, 2006, **17,** 967.

19. W.C. Xue, X.Y. Liu, X.B. Zheng, C.X. Ding. *Biomaterials* 2005, **26,** 3453.

20. H. Ramay, M. Zhang. *Biomaterials* 2004, **25,** 5171.

21. S.K. Vasudev, B.R.Goel, S. Tyagi. *Endodont.*, 2003, **15,** 12,

22. J.O. Andreasen. *Acta Odontol. Scand.* 1973, **31,** 211.

23. K.R. Craig, J.W. Harrison. *J. Endod.* 1993, **19,** 339.

24. M. Parirokh, M. Torabinejad, *J. Endod.* 2010, **36**, 16.

25. Asgary S, Parirokh M, Eghbal MJ, Brink F. *J. Endod.* 2005, **31,** 101.

26. I. Islam, H.K. Chng, A.U. Yap. *Int. Endod. J.* 2006, **39,** 220.

27. Funteas UR, Wallace JA, Fochtman EW *Aust. Dent. J.* 2003, **29,** 43.

28. SAsgary, M Parirokh, M.J. Eghbal, F. Brink. *Aust. Endod. J.* 2004, **30,** 89.

29. G.K. Moir. Cements. In: Newman J, Choo BS, eds. Advanced Concrete Technology; Constituent Materials. Oxford, UK: Elsevier Butterworth Heinemann, (2003) pp. 3–45.

30. I. Odler. Hydration, Setting and Hardening of Portland Cement; in Lea's Chemistry of Cement and Concrete. London: Arnold, Ed. Hewlett PC, pp. 241–84. 1998.

31. H.F.W. Taylor. Cement Chemistry. London: Thomas Telford, (1997) pp. 113–225.)

32. F.R. Tay, D.H. Pashley, F.A. Rueggeberg, R.J. Loushine, R.N. Weller. *J. Endod.* 2007, **33,** 1347.

33. R. Holland, V. de Souza, M.J. Nery, F.E. Bernabı, J.A. Filho, E.D. Junior. *J. Endod.* 2002, **28,** 173.

34. J. Camilleri, F.E. Montesin, L. Di Silvio, T.R. Pitt Ford. *Int. Endod. J.* 2005, **38,** 834.

35. J. Camilleri. *Int. Endod. J.* 2007, **40,** 462.

36. C. Main, N. Mirzayan, S. Shabahang, M. Torabinejad. *J. Endod.* 2004, **30,** 80.

37. S.J. Lee, M. Monsef, M. Torabinejad, *J, Endod.* 1993, **19,** 541.

38. G. Bogen, J.S. Kim, L.K. Bakland. *J. Am. Dent. Assoc.* 2008, **139,** 305.

39. D.E.Witherspoon, J. C. Small, G.Z. Harris. *J Am Dent Assoc*, 2006, **137,** 610.

40. A. Bystrom, R. Claesson, G. Sundqvist. *Endod. Dent. Traum.* 1985, **1,** 170.

41. C. Stock. *Br. Dent. J.* 1985, **158,** 325.

42. E.T. Koh, T.R. Ford, S.P. Kariyawasam. *J. Endod.* 2001, **27,** 540.

43. T.R. Pitt Ford, M. Torabinejad, C.U. Hong, S.P. Hariyaswasm. *Oral. Surg. Oral.Med. Oral. Pathol. Oral. Radiol. Endod.* 1995, **79,** 759.

44. S.M. O'Sullivan, G.R. Hartwell. *J. Endod*. 2001, **27,** 703.

45. W.J. O'Brien. Dental materials and their selection, Chicago: Quintessence Publishing Co Inc. 2002.

46. J. Powers, J. Wataha. Dental Materials: Properties and Manipulation. New York: Mosby 2007.

47. J. Roeters, H.de Kloet. Handboek voor Esthetische Tandheelkunde. Nijmegen: STI; (1998)

48. L. Seppa. *Caries Res.* 1994, **28,** 406.

49. N. Nakabayashi, K. Kojima, E. Masuhara. *J. Biomed Mater Res.* 1982, **22,** 265

50. C. Solomons, W. Neuman. *J. Biol Chem.* 1960, **235,** 2502.

51. H. Oonishi, Y. Takayaka, I. C. Clarke, H. Jung, *J. Long-Term. Effects. Med. Implants*, 1992, **2,** 37.

52. B. Ben-Nissan, A.H. Choi, R.L.Cordingley, 'Alumina ceramics' in Kokubo, T (eds), Bioceramics and their clinical applications, Woodhead Publishing Ltd, Cambridge UK, pp. 223-242. 2008.

53. Willman G. 'Biolox® forte heads and cup inserts for THR – what a surgeon should know', in *Bioceramics in Orthopaedics – New Application*, Enke, Stuttgart. 1997

54. H. Oonishi, I.C. Clarke, V. Good, H. Amino, M. Ueno, S. Masuda, K. Oomamiuda, H. Ishimaru, M. Yamamoto, E. Tsuji 'Needs of bioceramics to longevity of total joint arthroplasty', in Ben-Nissan B, Sher D and Walsh W, *Bioceramics 15*, Switzerland, Trans. Tech. Publications, 735–754. 2003.

55. L. Sedel. 'Tribology and clinical experience of alumina–alumina articulations', in Proceeding of the 66th Annual Meeting of the American Academy of Orthopaedic Surgeons, Anaheim, CA, 120. 1999.

56. P. Boutin, P. Christel, J.M. Dorlot, A. Meunier, A. de Roquancourt, D. Blanquaert, S. Herman, L. Sedel, J. Witvoet. *J. Biomed. Mater. Res.* 1988, **22,** 1203.

57. Willman G, 'Biolox® forte heads and cup inserts for THR – what a surgeon should know', in Bioceramics in Orthopaedics – New Application, Enke, Stuttgart. 1997.

58. J. D. Antonio, W. Capello, M. Manley, M. Naughton, K. Sutton. *Clin. Ortho. Relat. Res*. 2005, **436,** 164.

59. M. Hamadouche, P. Boutin, J. Daussange, M.E. Bolander, L. Sedel. *J. Bone. Joint. Surg. Am.* 2002, **84,** 69.

60. P. Christel, A. Meunier, J.M. Dorlot, J.M. Crolet, J. Witvoet, L. Sedel, et al. *Ann. NY. Acad. Sci.* 1988, **523,** 234.

61. R.C. Garvie, R.H. Hanninck, R.T. Pascoe. *Nature*. 1975, **258,** 703.

62. J. Chevalier, *Biomaterials* 2006, **27,** 533.

63. J. Chevalier, L. Gremillard, S. Deville. *Ann. Rev. Mater. Sci.*, 2007, **37,** 1.

64. K. Kobayashi, H. Kuwajima, T. Masaki. *Solid State Ionics.* 1980, **3/4,** 489.

65. M. Yoshimura, T. Noma, K. Kawabata, S. Somiya. *J. Mater. Sci. L.* 1987, **6,** 465.

66. H. Schubert, F. Frey. *J. Europ. Ceramic Soc.* 2005, **25,** 1597.

67. J. Chevalier, B. Cales, J.M. Drouin. *J. Am. Ceram. Soc.* 1999, **82,** 2150.

68. S. Lawson. *J. Europ. Ceramic Soc*. 1995, **15,** 485.

CHAPTER 2 - INSTRUMENTAL METHODS FOR STRUCTURAL INVESTIGATION

2.1 Spectroscopic Techniques

When an electromagnetic wave interacts with matter, it always gives origin to several physical phenomena as absorption, emission and diffusion.

With the term spectroscopy we refer to the analytic use of these interactions for determining, identity, structure and eventually quantity, of studied species: the study of the frequencies and the intensities of the photons, before and after the interaction with matter, represent the basis of optic spectroscopic techniques.

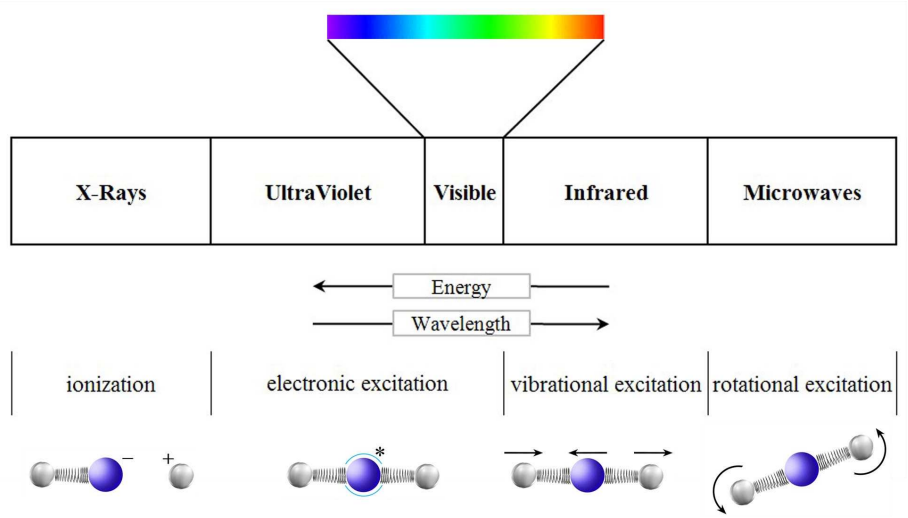

Figure 2.1: The electromagnetic spectrum and light-matter interactions: the IR radiation has sufficient energy to interact with the oscillations of the molecular bonds.

Different spectroscopic techniques operate over different, defined frequency ranges depending on the physical processes involved and magnitudes of the energy changes.

In this work vibrational spectroscopic techniques and fluorescence spectroscopy were used to obtain structural information.

Depending on the frequency of the radiation used (and therefore its energy) different effects on matter are induced (see Figure 2.1). Using an infrared radiation (i.e. with a wavelength in the range 0.7-500 μm), this energy is enough to cause a vibrational transition: vibration is defined as an oscillation in the meaning that atoms periodically change their position relative to an equilibrium position.

2.2 Vibrational Spectroscopy

A molecular vibration can be easily visualized by imagining a diatomic molecule A-B as two balls connected by a spring. The two atoms A and B can approach and move away periodically with a frequency ν that can be calculated from Hooke's law:

$$\nu_{vib} = 1/2\pi\sqrt{k/\mu}$$

where ν_{vib} is the frequency of vibration, μ is the reduced mass of the atoms ($m_A m_B$ / (m_A+ m_B)), k is the force constant of the A-B bond. The frequency of vibration will be greater the greater the bond strength and the lower the mass of the atoms involved.

The force constant k is a function of both the nature of the bond between A and B, and the interactions between the molecule and the medium: therefore, vibrational spectroscopy can provide information on the properties both of the single molecule, and of any intermolecular interactions (such as the existence and strength of hydrogen bonds).

The potential energy for harmonic oscillation of two particles is represented by a parabolic function. Although this is a continuous function, the total vibrational energy of a molecule is quantized: the permitted values for the energy are defined by the expression:

$$E_{vib}=h(v+½)\,\nu_{vib}$$

where h is Planck's constant, v is the vibrational quantum number (it can take positive integers: 0, 1, 2, 3 ...) which defines the level of energy and ν_{vib} is the vibration frequency. The vibrational levels are equally spaced (red curve in Figure 2.2) and the separation between levels is equal to hν. The harmonic oscillator model is a simplification if compared to real vibrational motion, because the molecules show anharmonic vibrations.

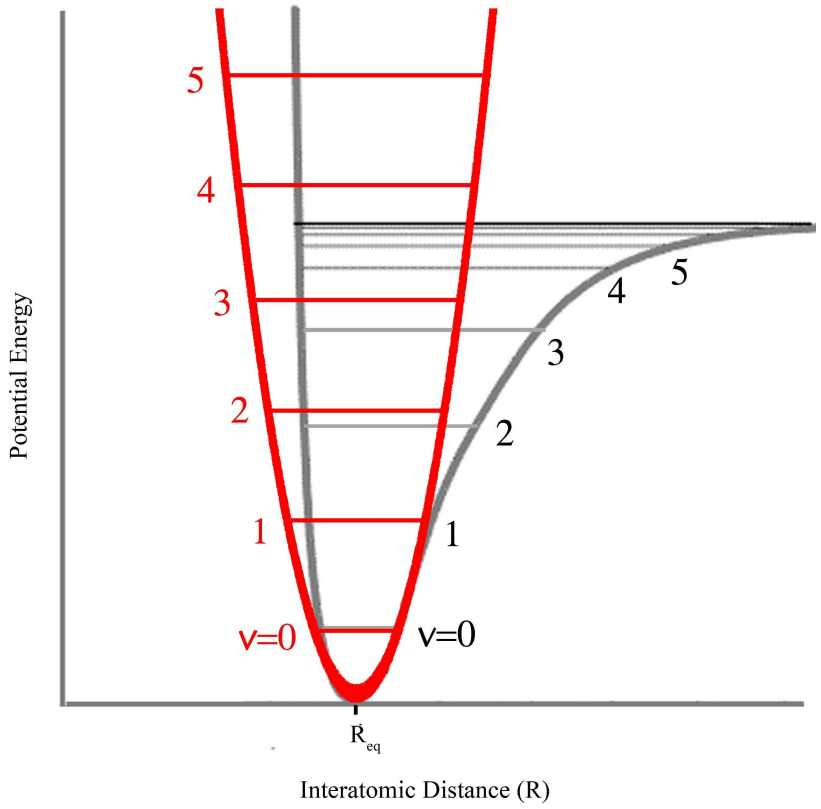

Figure 2.2: Vibrational potential energy curves and levels as function of interatomic distance according to the harmonic (red) and anharmonic (grey) models.

In the anharmonic oscillator real model, vibrational energy is quantized according to the expression:

$$E_{vib} = h\,[(v + ½)\,\nu_{vib} - (v + ½)^2\,X_e\,\nu_{vib}].$$

Where X_e is a constant of anharmonicity. The formula shows that the energy levels tend to an asymptote with increasing vibrational quantum number (grey curve in Figure 2.2). The possible vibrations of a polyatomic molecule consisting of N atoms depend on the number of vibrational degrees of freedom (or modes) of the molecule: it possesses 3N degrees of freedom including 3 translational and 3 rotational (2 in linear molecules): the molecular vibrational modes are therefore 3N-5 if the molecule is linear and 3N-6 if it is not linear.

There are two modes of molecular vibration (Figure 2.3): *stretching* and *bending*. The first is a rhythmic movement along the bond axis resulting in change in the interatomic distance, while the second is due to a variation of the bond angle or a movement of a group of atoms with respect to the rest of the molecule. For example, the *twisting* (torsion), *rocking* (in plane oscillation) and *wagging* (out of plane swing) vibrations cause a change in bond angles with respect to the arbitrarily fixed coordinates within the molecule. In particular, the number of stretching vibrations of a molecule is N-1, while the bending vibrations are 2N-5. Usually, the values of the stretching frequencies are higher than those of bending because more energy is required to stretch the bonds than to bend them; multiple bonds also have higher frequencies than single bonds because of the increased force constant of the multiple bond. (e.g. νC-C: 700-1200 cm^{-1}; νC=C: 1600-1680 cm^{-1} νC≡C: 2250-3000 cm^{-1}).

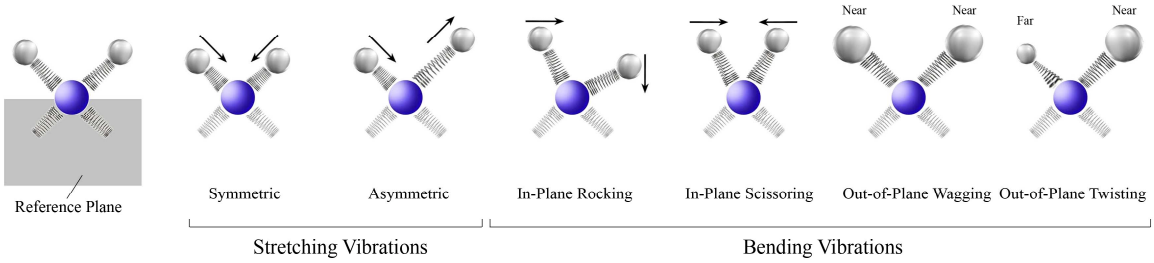

Figure 2.3: Molecular vibration modes

When two oscillating bonds share a common atom, rarely act as independent oscillators as there is an interaction of mechanical coupling between oscillators. The coupling of two fundamental modes of vibration will produce two new vibrational modes, with higher and lower frequency values than those observed when the interaction is absent.

Coupling is observed if there is an atom shared by two groups that adsorb, individually, at frequency very close; the coupling is negligible when the groups are separated by one or more atoms.

2.2.1 Infrared Spectroscopy

IR spectroscopy is a vibrational absorption spectroscopy. The infrared radiation used is the part of the electromagnetic spectrum between the regions of the visible and microwave (20 to 14000 cm^{-1}), although the practical interest is limited to the area of the middle IR (400 - 4000 cm^{-1}). The absorption of IR radiation by molecules leads to a jump between two vibrational levels. The necessary but not sufficient condition, so that a molecule absorbs infrared radiation is that radiation energy is equal to the difference between two

vibrational levels of the molecule. In fact, in infrared absorption, only those vibrations leading to a variation of the dipole moment of the molecule are observed. The alternating electric field, produced by the change of the charge distribution that accompanies the vibration, coupled to oscillating electric field of radiation and absorption is observed.

Each functional group can have more vibrational modes that correspond to different energies (such as stretching and bending); the same functional group in different molecules presents specific vibrational motions, which result in absorption bands located at characteristic frequencies (the so called group frequencies), only marginally affected by the complexity of molecular structure.

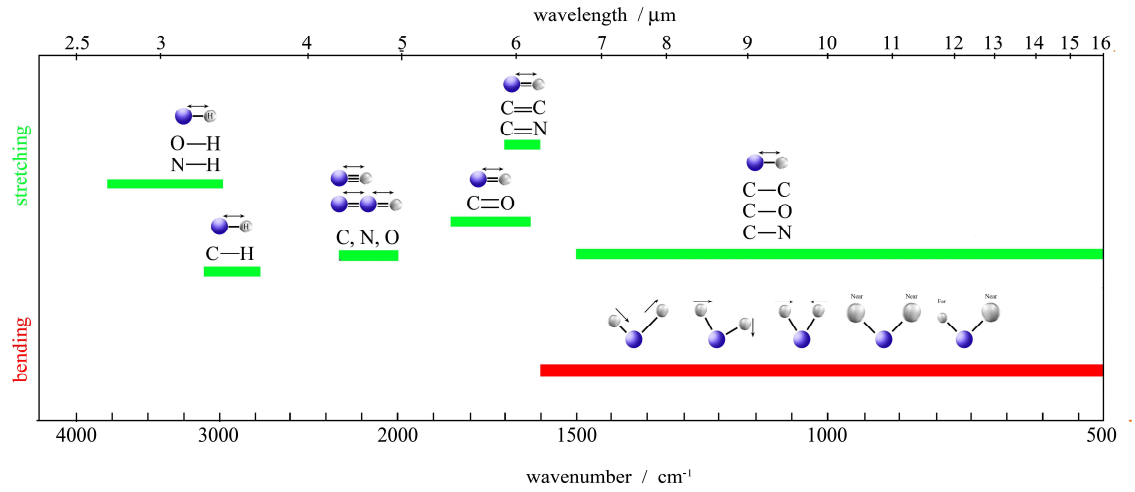

Figure 2.4: Group frequencies in IR spectroscopy.

An IR spectrum is obtained by irradiating the sample with a rather wide range of infrared radiations and observing, at each wavelength, if the radiation is absorbed by the sample according to the functional groups present in the molecule. An important parameter

of the IR spectra is given by the resolution, i.e. the ability of the instrument to discriminate two adjacent peaks; typically most spectra are recorded with a resolution of 4 cm^{-1}. The variation of the resolution has important consequences not only on the spectral quality but also on the timing of recording spectra: in fact, an increase in resolution will significantly increase the time required to obtain a spectrum.

For many years the infrared spectrum has been recorded by passing the IR radiation through the sample and scanning the spectrum by rotating a dispersing element (prism or diffraction grating); absorption bands (peaks) were detected and printed as a graphic intensity as a function of frequency. The monochromator could be inserted before or after the sample. Figure 2.5 shows an example of a dispersive double beam, where the radiation is divided into two portions: one passes through the sample, the other through the reference cell. By subtracting the two signals, the resulting spectrum contains only the absorption peaks of the sample.

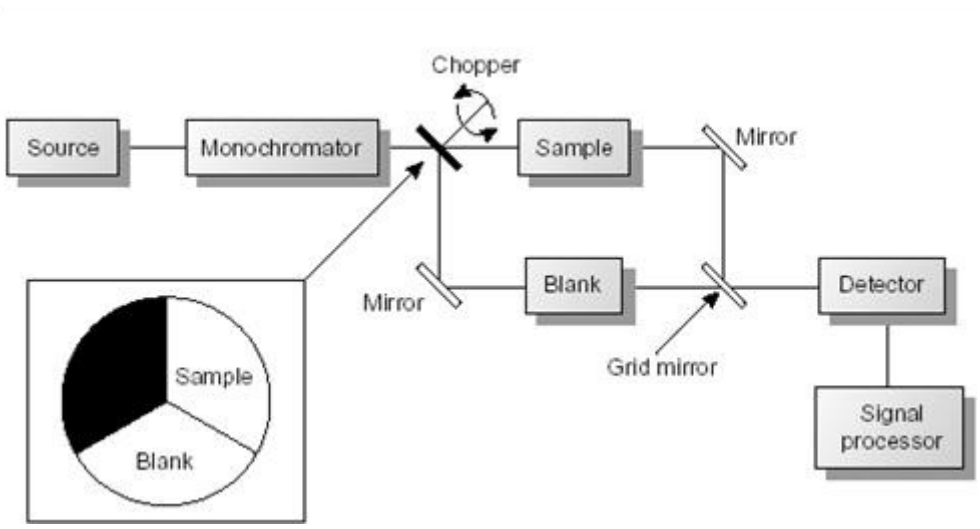

Figure 2.5: Block diagram of a dispersive IR dual-beam spectrophotometer.

The infrared spectroscopy has experienced a revival in recent years, thanks to the development of Fourier transform IR spectrometers (FT-IR), which have many advantages if compared to traditional dispersive spectrometers. The radiation, which contains all IR wavelengths, is divided into two rays (Figure 2.6) by a beam splitter (which reflects 50% of the light and transmits the remaining 50%). A ray travels a fixed distance, being reflected by a fixed mirror, while the other a variable distance, being reflected from a moving mirror.

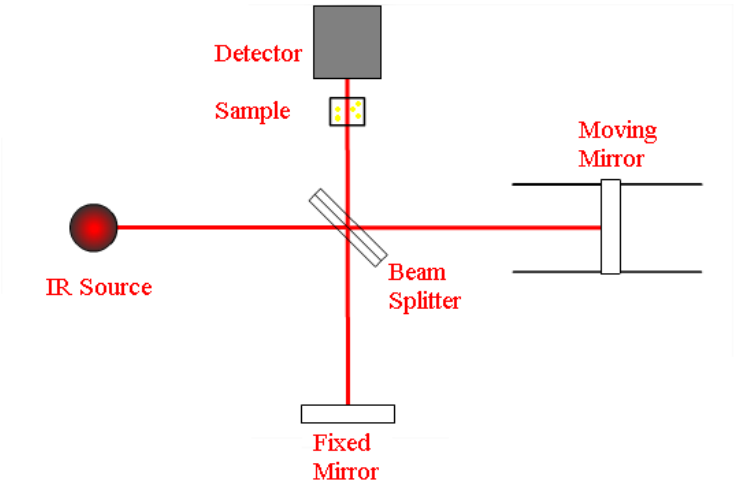

Figura 2.6: FT-IR spectrometer diagram.

Then the two radiations return to the beam splitter where they recombine and are reflected back to the sample. The different lengths of the two paths lead to a sequence of constructive and destructive interference and, consequently, to changes in intensity.

In this way we obtain an interferogram (set of maximum and minimum), which is however difficult to interpret and is transformed into a spectrum by a mathematical process called Fourier transformation.

The advantages of FT-IR instruments are many. Since a monochromator is not used, all frequencies of radiation pass simultaneously through the sample, and there is a considerable saving in time with the ability to accumulate in a reasonable time a large amount of spectra, with a consequent improvement of the signal / noise ratio.

The FT-IR instruments can have an extremely high resolution, and since a data conversion from analogue to digital is performed, they can be easily processed. All IR spectra shown in this thesis were obtained with a FT-IR spectrophotometer.

With regards to sampling, spectra of gases, liquids and solids can be measured: the solids can be analyzed in transmission in the case of samples not too thick (e.g. thin films). In transmission, the sample (e.g. a powder) is intimately mixed with a suitable amount of anhydrous KBr (transparent to IR radiation) in an agate mortar. The mixture is then compressed to obtain a transparent disk in which the solid sample is evenly dispersed. The spectrum can be interpreted in two ways: considering the sample transmittance or its absorbance. The transmittance can be defined as the ratio between the intensity of transmitted light with the intensity of incident light: a transmittance of 100 is obtained for the wavelengths that are not absorbed by the sample and 0 for the completely absorbed ones.

The absorbance is instead the decimal logarithm of the inverse of the transmittance: the two modes are equivalent.

Many materials can be positioned in close contact with a suitable substrate and the spectra could be recorded exploiting the internal reflection using an instrumental setup called Attenuated Total Reflectance (ATR). Working in ATR mode, the sample is positioned on a stand made of a crystal with a high refractive index (ZnSe, Ge, or diamond): the IR beam

is reflected several times in the inner surface of the crystal and then on the sample (Figure 2.7), originating an evanescent wave that is projected orthogonally onto the sample placed in close contact with the crystal, generating the reflectance spectrum (which is calculated in a similar way to the transmittance). To obtain the spectrum, it is therefore necessary to place the sample in close contact with the ATR crystal. The analytical response comes from a surface layer of sample whose thickness depends on the material of the ATR crystal device (for example, using a diamond crystal, the incident radiation penetrates the sample for a depth of about 2 μm). The depth of penetration is also a function of the wavelength.

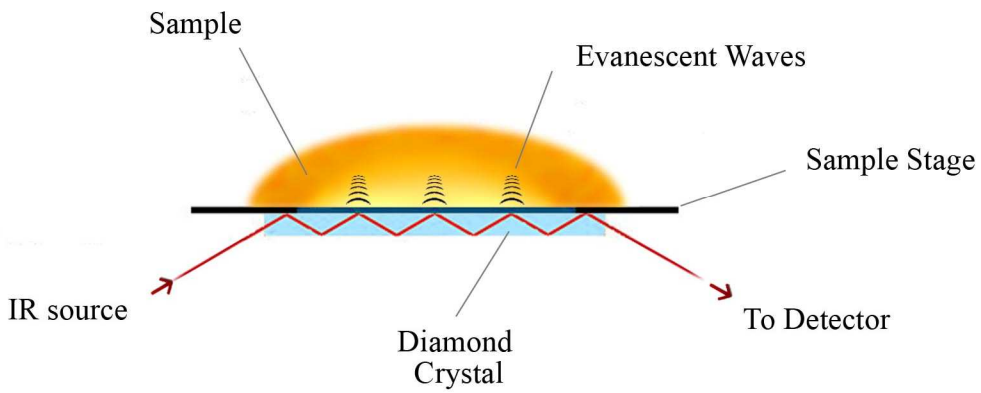

Figure 2.7: Scheme of the reflections within the ATR crystal.

The IR spectra in the ATR mode are similar to those recorded in transmittance (and thus absorbance). There are subtle differences: particularly low frequency bands have absorbance values higher than those at high frequencies, but usually the instruments management software are able to compensate for these differences.

The IR spectra discussed in this thesis were recorded on a Nicolet 5700 FT-IR spectrometer (Thermo Electron Scientific Instruments Corp., Madison, WI, USA) equipped with a Smart Orbit diamond attenuated total reflectance (ATR) accessory and a Deuterated Tri-Glycine Sulphate detector; the spectral resolution was 4 cm^{-1}, and 64 scans were made for each spectrum. The ATR area had a 2 mm diameter and the IR radiation penetration was about 2 microns.

2.2.2 Raman Spectroscopy

Raman spectroscopy is based on the Raman effect, described as the diffusion (scattering) of inelastic photons by molecules. It can provide information on the molecular composition, the chemical environment, the phase and the crystalline structure of the sample, and is suitable for the non destructive and non invasive analysis of materials in several forms: gases, liquids and solids (amorphous or crystalline). The Raman effect is a physical phenomenon discovered in 1928 by the Indian physicist C.V. Raman: that discovery earned him the Nobel Prize in Physics in 1931. He noted that a small fraction of the radiation scattered by certain molecules was characterized by energy different from that of the incident radiation: that energy difference was related to the chemical structure of the molecules responsible for the scattering.

A monochromatic coherent radiation emitted from a laser source with frequency ν_0 can interact with a molecule in different ways: it may be absorbed if it has energy equal to a possible transition between two electronic, vibrational (as in the case of IR) or rotational energy levels, may be reflected (if there are no interactions) or diffuse, if the interactions do not cause energy transitions.

Assume an interaction between radiation and a molecule in its fundamental vibrational level or in an excited vibrational level. The photon of $h\nu_0$ energy can be absorbed by the molecule, which increases its energy by an amount equal to the photon energy (Planck's law $E = h\nu$). In general, molecules, after the interaction with electromagnetic radiation, are in a virtual excited state as usually the energy supplied is not sufficient to cause electronic transitions and tend to return quickly (after about 10^{-14} seconds) either to the vibrational level that occupied or to another vibrational level. In the first case (elastic scattering, see

Figure 2.8 a) the scattered radiation has the same energy and hence the same frequency ν_0 of the exciting incident light (Rayleigh scattering).

In the second case (inelastic scattering) the light can be scattered with a lower frequency, $\nu_0 - \nu_1$ (Stokes Raman effect, Figure 2.8 b), or with a higher frequency, $\nu_0 + \nu_1$ (anti-Stokes Raman effect, Figure 2.8 c) with respect to the exciting radiation. Due to Raman effect, part of the ν_0 incident frequency after scattering becomes $\nu_0 \pm \nu_1$, where ν_1 depends on the energy separation between vibrational levels and is therefore characteristic of a specific vibration of the molecule under investigation; the inelastic scattering is an event much less likely than the elastic scattering (about 10^6 times) and its signal is therefore also less intense. In general, for indicating the energy in Raman spectroscopy, the frequency difference (Raman shift) with respect to the absolute frequency of the exciting radiation is used instead of absolute frequency.

As displayed in Figure 2.9, the Stokes bands are considerably more intense than anti-Stokes and therefore experimentally measured: this asymmetry can be explained considering that the fundamental vibrational state population is greater than in the excited vibrational levels (Boltzmann distribution), so you will have a greater probability of transitions of Stokes type. Raman bands are due to transition that involve vibrational states of the molecule as discussed for IR spectroscopy (albeit with different selection rules) and placed in similar spectral regions. It is interesting to note that Raman spectroscopy allows easy access to wavenumbers region below 400 cm^{-1}, allowing for example to analyze the bands of the crystal lattice, otherwise hardly accessible to the IR spectrometers.

The intensity of the scattered light depends on the wavelength of the scattered radiation (inversely proportional to λ^4) while the Raman shift does not. For example, using an

exciting green light at 514 nm or blue at 488 nm, in both cases a band with the same ν_1 Raman shift is obtained, since the difference between the fundamental and the excited vibrational levels remains the same.

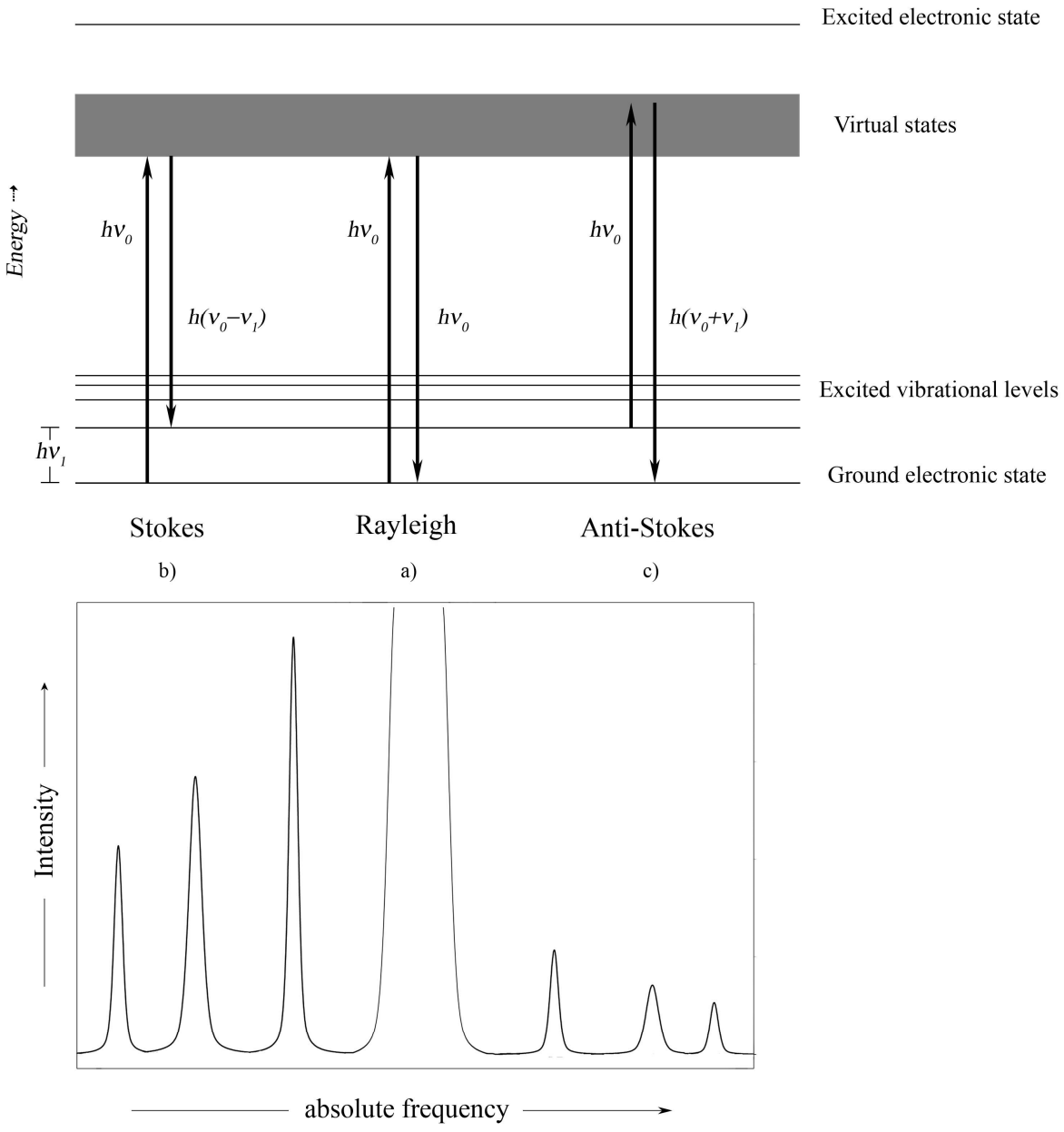

Figure 2.8: Comparison between elastic scattering (a) and Raman-Stokes (b) and Raman-Anti-Stokes inelastic scattering. Note the symmetry between the Stokes and anti-Stokes bands with respect to Raleigh radiation and their relative intensities.

However, it is important to note that in some applications, the choice of the laser is extremely important: in fact, the most common interference found in the Raman spectra is given by fluorescence (especially present in organic samples of biological origin) that involves an increase of the baseline spectrum. Fluorescence is a physical phenomenon by which the electrons return to the fundamental energetic state after being excited, with emission of radiation. Fluorescence, which can also be due to trace impurities, is much more intense than Raman signals and can sometimes make it undetectable. The use of a laser source at lower frequencies decreases the possibility of inducing electronic transitions and then to have fluorescence. It is necessary to seek the best compromise between minimizing the intensity of fluorescence and the maintenance of a sufficient Raman intensity (which scales with ν^4). There are lasers that emit in the UV, visible and near IR regions: in this thesis an Argon-Krypton laser emitting at different wavelengths (488, 514 and 647 nm), and a Nd^{3+} : YAG (yttrium aluminium garnet doped with neodymium) emitting in the near-IR at 1064 nm, were used.

Raman and IR spectroscopy are complementary techniques because the transition involved obey to different selection rules. While the IR spectroscopy is based on the change of the electric dipole moment during the transition, in order to observe the Raman effect, the incident light must induce a change in polarizability during the vibration of the molecule (distortion of the electron cloud of the molecule). It may therefore happen that not much intense or absent Raman bands are intense in IR and vice versa; in particular, considering molecules characterized by a centre of symmetry, the transitions allowed in Raman are forbidden in IR and vice versa. An advantage of Raman spectroscopy is the ability to record spectra of aqueous solutions, almost impossible by the IR spectroscopic technique,

because of the strong IR absorption of water while its Raman bands are less intense. Also Raman spectroscopy support two types of instruments, as for the IR spectroscopic technique: a dispersive type (consisting of a monochromatic laser source, a cell sample holder, a monochromator and a detector), or a Fourier Transform type, which uses a Nd^{3+}: YAG laser. The use of this laser introduces several advantages: it allows to operate with higher power without causing the photolysis of the sample as well as the phenomenon of fluorescence since it does not provide enough energy for electronic transitions. However, the possible drawbacks reside in the decreased signal intensity (which depends on the laser frequency) and the interference from water.

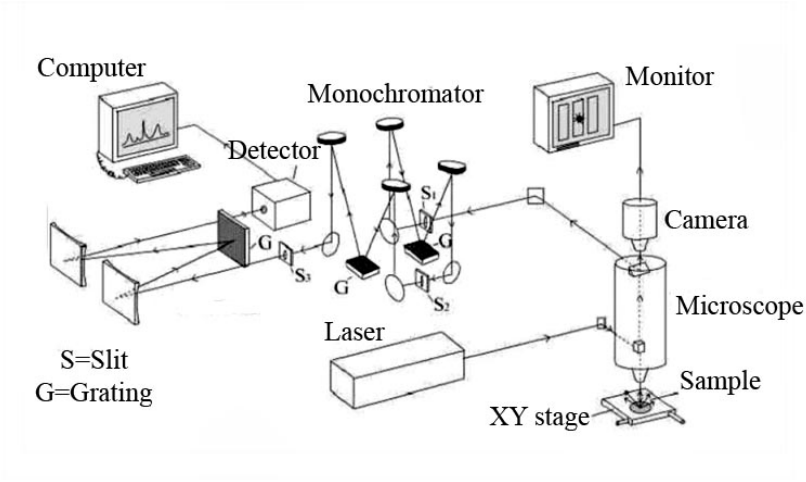

Figure 2.10: Scheme of a dispersive Raman spectrometer coupled to a microscope.

When light strikes the sample, light scattering is observed in all directions. The light is usually collected at 90° or 180° with respect to the incident radiation and focused on the detector. The recording of a spectrum using a dispersive Raman spectrometer can take a long time to scan the entire spectral range: thanks to the introduction of multichannel

detectors (CCD charge coupled device), non-dispersive spectrometers have been developed obtaining much faster registration of the spectrum.

Raman microscopy has been developed by coupling two techniques, i.e. microscopy and Raman spectroscopy; in Raman microscopy the laser is focused on very small regions of the sample (few microns) with a consequent increase in signal intensity and the possibility to analyze punctual regions of inhomogeneous samples.

The possibility of using a confocal setup allows to obtain spectra from a thin section of sample. In this thesis micro-Raman spectra were recorded using a Jasco NRS-2000C instrument (Jasco Inc., Easton, MD, USA) connected to a microscope with 10-20 or 100× magnification depending on specific experiments. All the spectra were recorded in back-scattering conditions with 1 or 5 cm^{-1} spectral resolutions using the 514 nm line (Innova Coherent 70; Coherent Inc., Santa Clara, CA, USA). As detector unit, a 160 K frozen Charge Coupled Device from Roper Scientific Inc (Trenton, NJ, USA) was used. Due to the high fluorescence of some samples upon excitation in the visible range, the Raman spectra were recorded with a less energetic excitation source. A Nd^{3+} : YAG laser emitting in the near-infrared region (1064 nm) was used with a Bruker MultiRam Fourier Transform FT-Raman spectrometer (Bruker Optik GmbH, Ettlingen, Germany) equipped with a cooled Ge-diode detector. With this instrument the laser beam spot diameter was about 100 μm and the spectral resolution was of 4 cm^{-1}.

2.3 Fluorescence Spectroscopy

Using as excitation source a UV-visible frequency radiation, other photo-physical phenomena other than scattering usually occur. These photon energies induce modification

in the electronic distribution of the molecule: absorbing a photon, the system is promoted from the ground state S_0 to an excited electronic state S_1.

Fluorescence is observed when an a molecule or atom from an excited electronic state relaxes to its ground state by emitting a photon of light.

The excitation process $S_0 + h\nu_{ex} \rightarrow S_1$ is followed by vibrational relaxation (internal conversion) and then by emission (fluorescence) $S_1 \rightarrow S_0 + h\nu_{em} + \Delta$, where $h\nu$ is the photon energy, h is Planck's constant and ν is the light frequency (Figure. 2.11).

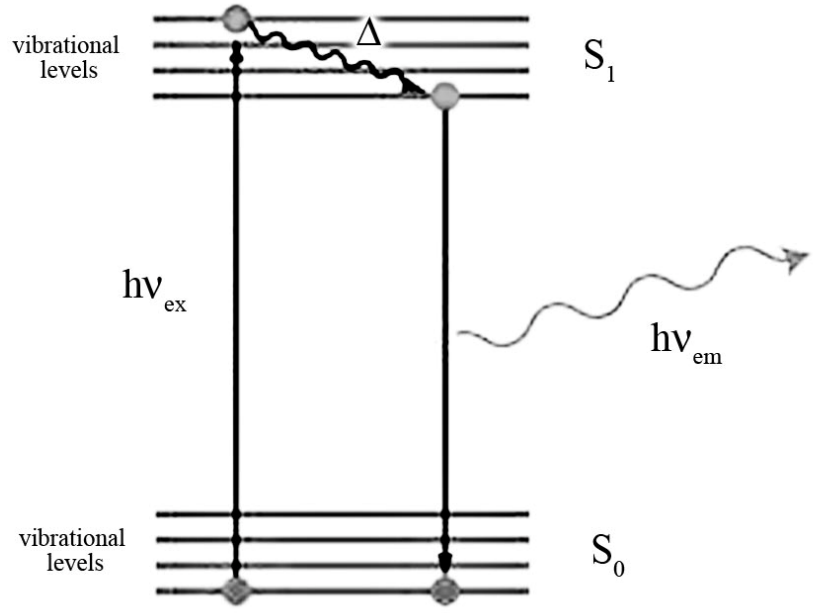

Figure 2.11: Jablonski diagram of the emission (fluorescence) process.

A molecule in its excited state, S_1, can relax by various competing pathways. In addition to fuorescence, one also encounters radiationless processes where molecules in an excited state may return to the ground state without the emission of a photon, converting all the excitation energy into heat. The process is called internal conversion.

Another possible pathway of relaxation is represented by phosphorescence that, as fluorescence, is radiative. The phosphorescence involve a process called *intersystem crossing* that can be considered a modification of the quanto-mechanical properties of the exited state. This modification can induce variation of frequency emitted and a delay of the radiative process.

A lot of compounds show fluorescence under UV-visible light excitation. A well know system that exhibits a characteristic emission if excited with visible photons is ruby.

Ruby is Al_2O_3 (α-alumina) wherein a small fraction of the Al^{3+} ions are replaced by Cr^{3+} ions. Each Cr^{3+} is surrounded octahedrally by six O^{2-} ions. This crystallographic arrangement strongly affects each Cr^{3+}, resulting in light absorption in the yellow-green region of the spectrum (responsible for the red colour of the gem). After yellow-green light absorption by Cr^{3+}, the excited state relaxes to ground state emitting red light around 694 nm generating a characteristic doublet (Figure 2.12).

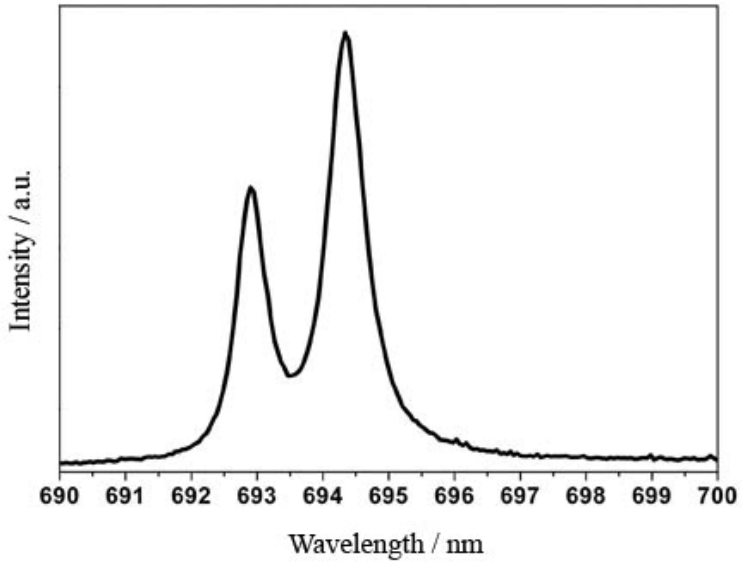

Figure 2.12: Characteristic doublet in the fluorescence spectrum of ruby

The emission process involves the interaction between the Cr^{3+} electronic distribution and the surrounding lattice (Al_2O_3): potential distortions of the lattice geometry significantly influence the fluorescence spectrum. The analysis of the position and the shape of the fluorescence bands gives information about the structural environment of the Cr^{3+} ions and therefore about the mechanical properties of the whole material (e.g. residual stresses).

The so-called photoluminescence piezospectroscopy is a well-established technique for optical measurements of residual stresses. This technique is based on measuring the spectral shift of a fluorescence band as a result of a stress-induced change in the surrounding crystal field and consequently electronic transition energy.

In the present thesis, the fluorescence of Cr^{3+}-containing alumina has been measured as a probe to analyse the residual stress state of the samples.

Also fluorescence spectroscopy can be coupled with microscopy to investigate smaller (i.e. micron-sized) areas of samples.

The instrumental setup of a micro-fluorimeter is displayed in Figure 2.13.

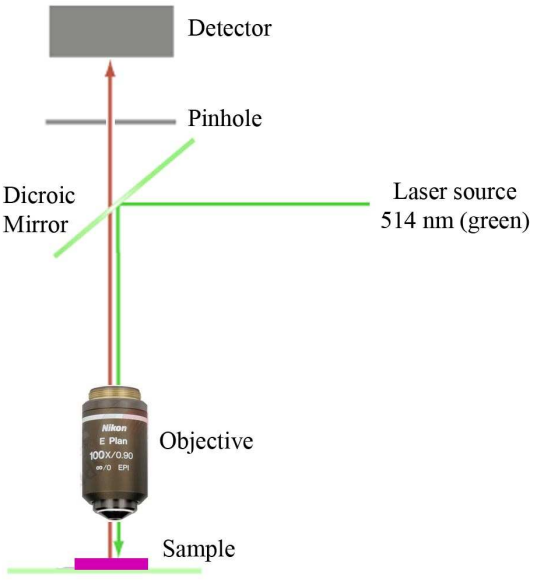

Figure 2.13: Schematic instrumental setup of a micro-fluorimeter

Here the sample is excited by a green laser source operating at 514 nm. The laser beam is focalized on the sample using a microscope; the fluorescence emitted is sampled through the lens and then routed to the detector.

The presence of the pinhole allows for confocal fluorescence microscopy that, eliminating out-of-focus emitted light from the specimen, probes only the material layers closed to the focal plane. This configuration is useful for investigating the strictly superficial region of the specimen.

2.4 References

- AA VV. *Fourier Transform Infrared Spectroscopy*. Theodofanides T, Reidel D ed, PublishingCompany, Dordrecht (1984).
- Colthup N B, Daly L H, Wiberley S E. *Introduction to Infrared and Raman Spectroscopy.*Academic Press, New York (1964).
- McCreery R C. *Raman Spectroscopy for the Chemical Analysis.* Wiley-Interscience, New York(2000).
- Shrader B. *Infrared and Raman Spectroscopy.* Weunheim (1995).
- Silverstein R M, Bassler G C, Morrill T C. *Spectrometric identification of organic compounds.*Wiley and Sons, New York (1991).
- Tu A. *Raman Spectroscopy in biology.* Wiley and Sons, New York (1982).
- Parker S F. *Applications of Infrared Raman and Resonance Raman Spectroscopy in Biochemistry*. Plenum Press, New York (1983).38
- Turro N. J. *Modern Molecular Photochemistry*. Univesity Science Books. Sausalito CA. (1991).

- Semwogerere D., Weeks E.R.. *Confocal Microscopy*. Emory University, Atlanta, Georgia, U.S.A.

Part II

CHAPTER 3 - BIOACTIVITY OF COMMERCIAL ROOT-END FILLING MATERIALS

3.1 Introduction

As introduced in the first chapter, many materials have been proposed and clinically used as root-end fillings, such as amalgam, zinc oxide cements, glass-ionomer cements (GIC), composites and MTA.

Root-end filling materials are placed in close contact with living tissues and must promote a fast bone healing and regeneration. A requirement for this functionality is the formation of an apatite layer that covers the material when introduced in its site (bioactivity).

To predict the *in vivo* apatite deposition, *in vitro* tests in a simulated body fluid (SBF) with ion concentrations nearly equal to those of human blood plasma can be performed.

The study of the bioactivity of commercial root-end filling materials is important to evaluate their biological behaviour and their impact on bone formation as well as to design and develop new experimental materials.

The aim of this chapter is to evaluate the bioactivity of six root-end filling materials after ageing in different soaking media characterized by different ions concentrations. DPBS (Dulbecco's Phosphate Buffered Saline) and HBSS (Hanks' Balanced Salt Solution) were selected as simulated body fluids to assess bioactivity in presence (HBSS) and absence (DPBS) of calcium ions.

3.2 Materials and Methods

Cements preparation

Six root-end materials, commonly used in surgical treatments were studied. Glass ionomer, zinc oxide-eugenol and MTA calcium silicate cements have been considered. The composition and manufacturers are summarized in Table 3.1.

MATERIAL	COMPOSITION	MANUFACTURER
IRM	**Powder:** 75% zinc oxide and 15% polymethylmethacrylate **Liquid:** 99% eugenol and 1% acetic acid	Dentsply DeTrey, Konstanz, Germany
Superseal cement	**Powder:** zinc oxide, aluminium oxide; calcium tungstate or natural resin. **Liquid:** 68% 2-etoxybenzoic acid, 32% bidistilled eugenol	Ogna, Muggio, Milano, Italy
Vitrebond	**Powder:** ion-leachable fluoroaluminosilicate glass SiO_2, AlF_3, ZnO, SrO, cryolite, NH_4F, MgO and P_2O_5.**Liquid:** modified poly-acrylic acid with pendant methacrylate groups, HEMA (2-hydroxyethylmethacrylate), water and photoinitiator.	3M, St.Paul, MN, USA
White ProRoot MTA	**Powder:** 80% white Portland cement and 20% bismuth oxide **Liquid:** distilled water.	Dentsply, Tulsa, OK
Grey MTA Angelus	**Powder:** 80% grey Portland cement and 20% bismuth oxide. **Liquid:** distilled water.	Angelus Soluções Odontológicas, Londrina, PR, Brazil
White MTA Angelus	**Powder:** 80% white Portland cement and 20% bismuth oxide. **Liquid:** distilled water.	Angelus Soluções Odontológicas, Londrina, PR, Brazil

Table 3.1: Composition and manufacturers of the root-end materials under study.

All the cements (provided by Professor Carlo Prati, Laboratory of Biomaterials, Department of Odontostomatological Science, University of Bologna, Italy) were prepared according to manufacturers' directions.

IRM is an intermediate restorative material well-tested as root-end filling material. SuperSeal cement is a zinc oxide-eugenol cement reinforced with 2-ethoxybenzoic acid.

Vitrebond is a resin-modified glass-ionomer cement (GIC) and was prepared following manufacturer directions [1 spoon (0.033 g)/1 drop (0.05 g)]. It was light-cured for 30 seconds with a LED lamp (Mod. Anthos Cefla, Imola, Italy) after the covering of the sample surface with a polyester transparent matrix (Directa Matrix Strips, Directa AB, Upplands Vasby, Sweden).

White ProRoot MTA, White MTA Angelus and Grey MTA Angelus powders were mixed with deionized water (powder:liquid ratio of 3:1) on a glass slab with a stainless steel spatula.

A homogeneous paste for each material was prepared and placed in round PVC mould of 8 mm of diameter and 1.6 mm high. The moulds were filled and the excess material was removed with a stainless steel spatula for obtaining a disk.

After preparation, the disks were immediately immersed in 5 mL of medium at 37 °C, i.e. DPBS (Cambrex Bio Science Verviers s.p.r.l., Belgium, cat. n.BE17-512) or HBSS (Cambrex Bio Science Verviers s.p.r.l., Belgium, cat. n.10-527).

The composition of the DPBS and HBSS solutions has been already reported in Table 1.2.

All the cements were analyzed after 1, 7, 14 and 28 days of soaking.

Angelus MTA cements were soaked only in DPBS. The storage media were renewed every week. The disks were analyzed by micro-Raman and IR spectroscopy both on their upper surface and their interior fractured section.

Spectroscopic measurements

IR spectra were recorded using a Nicolet 5700 FTIR (Thermo Electron Scientific Instruments Corp., Madison, WI, USA), equipped with a Smart Orbit diamond attenuated total reflectance (ATR) accessory and a DTGS detector; the spectral resolution was 4 cm^{-1}. The ATR area had a 2 mm diameter. Under this instrumental setup, the IR radiation penetration into the cement was about 2 μm. The aged samples were analysed after air-drying at room temperature. The unhydrated powders of the MTA cements were analysed as control immediately after the opening of the packages (to avoid the carbon dioxide uptake from environment and the formation of calcium carbonate); the other cements were analysed immediately after their preparation (unaged samples).

Micro-Raman spectra were recorded *in situ* on the samples maintained in their storage media, to prevent any transformation. The spectra were obtained using an argon laser (Innova Coherent 70; Coherent Inc., Santa Clara, CA, USA) operating at 514 nm and a Jasco NRS-2000C micro-Raman spectrometer (Jasco Inc., Easton, MD, USA) equipped with a 160 K frozen digital CCD detector (Spec-10: 100B, Roper Scientific Inc. Trenton, NJ, USA) employing a microscope of 20× magnification. Under these conditions, laser spot size was about 5 μm. All the spectra were recorded in back-scattering conditions with 5 cm^{-1} spectral resolution and a power on the sample of about 50 mW. Five IR and five Raman spectra at least were recorded in each area of each specimen.

Due to the high fluorescence of Vitrebond upon excitation in the visible range (i.e. at 514 nm), the Raman spectra were recorded using a Nd^{3+}- YAG laser emitting in the near-infrared region (1064 nm) with a Bruker MultiRam Fourier Transform FT-Raman spectrometer (Bruker Optik GmbH, Ettlingen, Germany) equipped with a cooled Ge-diode detector. The focused laser beam diameter was about 100 µm, the spectral resolution 4 cm^{-1}, and the laser power at the sample about 300 mW.

The spectra in the figures are representative of the obtained measurements. Intensity ratios were calculated as peak heights.

pH measurements

The pH of the soaking solutions was measured using a Denver Instrument Basic pH meter (Denver Instruments, Bohemia, NY, USA), equipped with a Hamilton liquid-glass electrode and ±0.01 resolution, which had previously been calibrated with acidic, neutral, and alkaline standard solutions. pH was measured at room temperature (24°C) after 1, 7, 14 and 28 days of incubation.

3.3 Results

Spectra of the unaged materials

Figures 3.1 and 3.2 show the IR and Raman spectra of the unaged materials, respectively.

The IR spectrum of unaged SuperSeal (Figure 3.1A) shows the bands typical of the cement formulation. The bands due to EBA, 2-ethoxybenzoic zinc salt (EBA-Zn) and eugenol have been assigned according to the literature [1,2]. The non detection of the marker band

of eugenolate zinc salt at 1319 cm^{-1} [2] suggests the absence of this component and of its corresponding calcium salt. The Raman spectrum of SuperSeal (Figure 3.2A) appeared affected by strong fluorescence interference and was not considered.

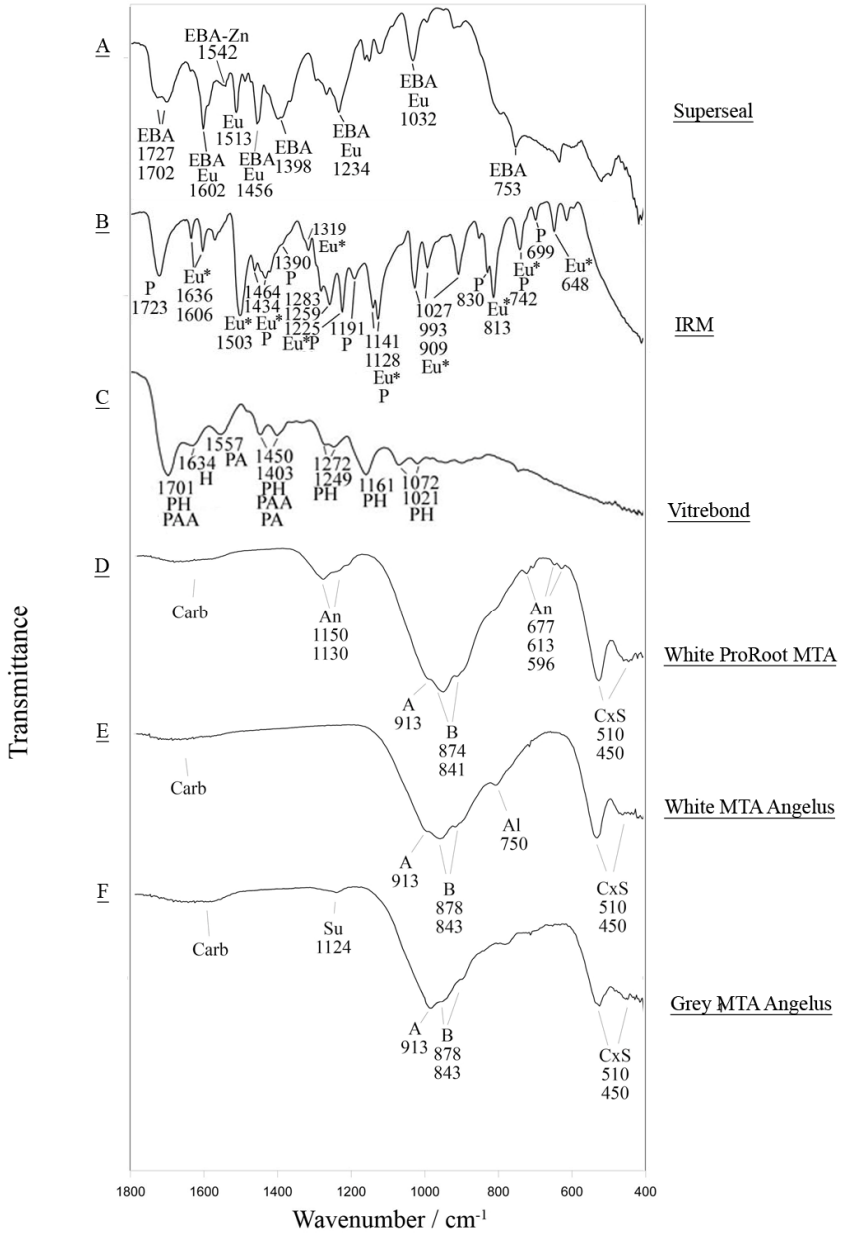

Figure 3.1: IR spectra of the unaged materials. The bands prevalently due to 2-ethoxybenzoic acid (EBA), 2-ethoxybenzoic zinc salt (EBA-Zn), eugenol (Eu) eugenolate zinc salt (Eu*), polymethylmethacrylate (P), HEMA unreacted monomer (H), poly-

HEMA (PH), poly-acrylic acid (PAA), poly-acrylate (PA), calcium carbonate (Carb), sulphates (Su), anhydrite (An), alite (A), belite (B), tricalcium aluminate (Al), fewly polymerised silicate tetrahedra (CxS) are indicated.

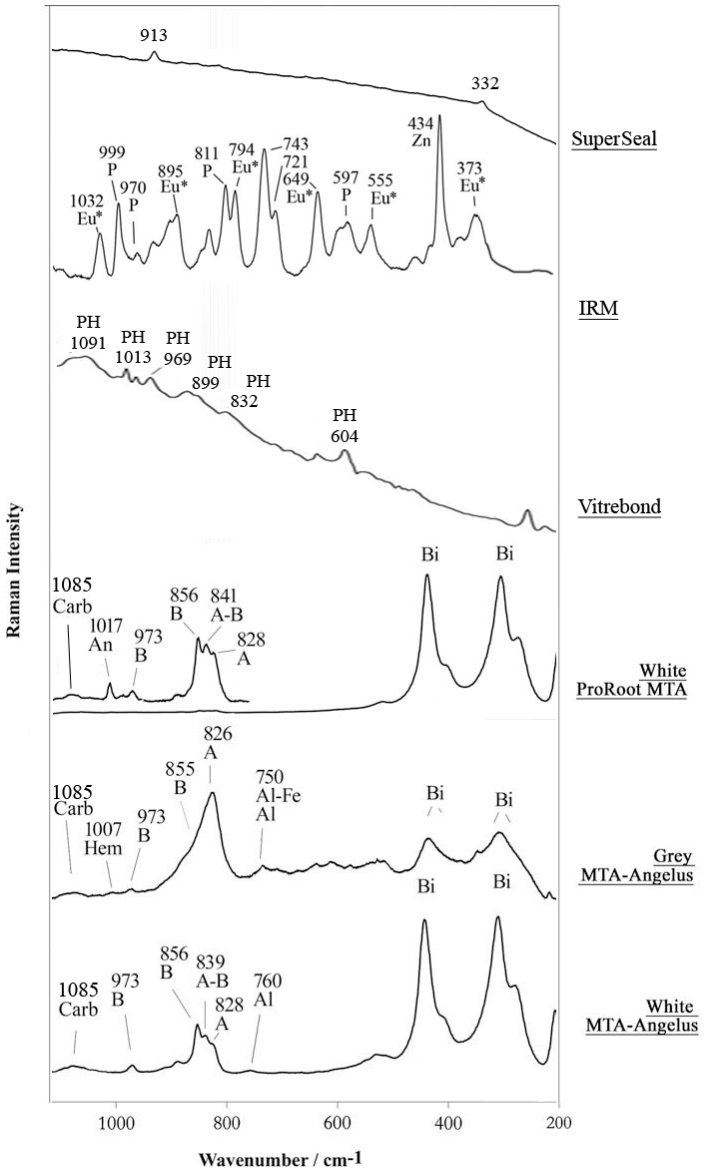

Figure 3.2: Raman spectra of the unaged materials. The bands prevalently due to eugenolate zinc salt (Eu*), polymethylmethacrylate (P), zinc oxide (Z), poly-HEMA (PH), calcium carbonate (Carb), anhydrite (An), calcium sulphate hemihydrate (Hem), alite (A), belite (B), tricalcium aluminate (Al), tetracalcium aluminoferrite (Al–Fe), bismuth oxide (Bi) are indicated.

Figures 3.1B and 3.2B show the IR and Raman bands ascribable to the IRM components (in particular, eugenolate zinc salt, polymethylmethacrylate and zinc oxide) assigned according to the literature [2-4].

The IR and Raman spectra of unaged Vitrebond (Figures 3.1C and 3.2C) were dominated by the bands of the polymeric component (i.e. unreacted HEMA monomer, poly-HEMA, poly-acrylic acid (PAA) and poly-acrylate), assigned according to the literature (5-6).

Figures 3.1D, E, F and 3.2D, E, F show the IR and Raman spectra recorded on the unhydrated powders of the three MTA cements (White ProRoot MTA, White MTA Angelus and Grey MTA Angelus, respectively). Bands assignments have been given according to the literature [7- 8].

The IR spectra of all the unhydrated cements (Figures 3.1 D, E, F) showed the bands due to belite, alite, and calcium carbonate with different relative intensities. Bismuth oxide component was not detectable in the investigated spectral range.

In all the spectra the bands at 510 and 450 cm^{-1} were present: they are assignable respectively to out-of-plane and in-plane bending modes of fewly polymerised silicate tetrahedra (CxS) [9]. The band at about 915–930 cm^{-1} was attributed to alite [10], and the components at about 875 and 845 cm^{-1} were assigned to belite [11]. In Grey Angelus-MTA the belite bands were observed with the highest relative intensity.

In the IR spectrum of the White ProRoot MTA unhydrated powder, the bands at 1150–1130 cm^{-1} (triply degenerate stretching mode), 677, 613 and 596 cm^{-1} (bending modes) indicate the presence of calcium sulphate in the anhydrite form [12]. On the basis of band

relative intensities, it can be deduced that the sulphate content decreased along the series White ProRoot MTA > Grey MTA Angelus > White MTA Angelus.

According to its Material Safety Data Sheet (MSDS) no calcium sulphates were observed in the White MTA-Angelus unhydrated powder. The spectrum of White MTA-Angelus showed a prominent component at about 750 cm^{-1}, attributable to stretching vibrations of AlO_4^{4-} tetrahedra of tricalcium aluminate [13-14], which has a unit cell containing eight cyclic $Al_6O_{18}^{18-}$ anions, consisting of six corner-sharing AlO_4 tetrahedra [15]. Also in Grey MTA-Angelus a broader band at a similar wavenumber position was observed.
Actually the IR spectra of all the unhydrated MTA cements revealed, in a spectral range not shown, the presence of a band at 3640 cm^{-1} (OH stretching mode) due to portlandite.

The Raman spectra of all the unhydrated cements (Figures 3.2D, E and F) showed with different relative intensities the bands due to bismuth oxide (below 600 cm^{-1}), monoclinic belite and monoclinic alite.

A weak band at about 1085 cm^{-1} due to calcium carbonate was also observed [7] In agreement with other studies [16], the bands due to bismuth oxide were less intense in the MTA Angelus powders than in the other cements.

With regards to the silicate component, both White ProRoot MTA and White MTA-Angelus showed bands at 856 and 973 cm^{-1} (assignable to monoclinic belite), a band at about 840 cm^{-1} (due to both monoclinic alite and belite) and a component at 828 cm^{-1} (due to alite) [1-9]. In Grey MTA-Angelus the main band of silicates appeared at 826 cm^{-1}, suggesting that the alite phase was predominant on the belite phase (shoulder at 855 cm^{-1}). Actually, grey Portland cements are characterized by higher alite to belite ratios than white Portland cements [20].

In White ProRoot MTA the band at 1017 cm^{-1} due to anhydrite ($CaSO_4$) was detected. In Grey MTA-Angelus a weak band at 1007 cm^{-1} was observed suggesting the presence of calcium sulphate hemihydrate ($CaSO_4 \cdot 1/2H_2O$) [21]. In agreement with its MSDS, no calcium sulphate was detected in White MTA-Angelus.

The Raman spectra of MTA-Angelus cements show a weak component near 750–760 cm^{-1}. In White MTA-Angelus, the 760 cm^{-1} component is due to the tricalcium aluminate $3CaO \cdot Al_2O_3$ (ν_3 AlO_4^{4-} mode) [22]; white MTA-Angelus contains a higher amount of tricalcium aluminate than the other cements for which no evidence of this band was observed. In Grey MTA-Angelus the band at about 750 cm^{-1} is assignable to tricalcium aluminate as well as to aluminoferrite [17,19,23], a component typically present in grey Portland cements.

Spectra of the aged samples: upper surface

Figure 3.3 shows the IR spectra recorded on the surface of SuperSeal after ageing in HBSS (A) and DPBS (B) for 1, 7 and 28 days.

Upon ageing for 1 day in HBSS and DPBS, a broad band at about 1025 cm^{-1}, assignable to the PO_4^{3-} asymmetric stretching mode of an amorphous calcium phosphate (ν_3 PO_4) [24] was observed; the bands due to the underlying cement were still detectable in both media and appeared stronger upon ageing in HBSS, suggesting that in this medium the thickness of the calcium phosphate layer was lower. At increasing ageing times in both media, the bands due to the cement became progressively weaker, due to the thickening of the

deposit; after 28 days of ageing in both media, an unresolved band at about 545 cm^{-1} (ν_4 PO_4 bending) appeared, confirming the amorphous nature of the deposit [24-25].

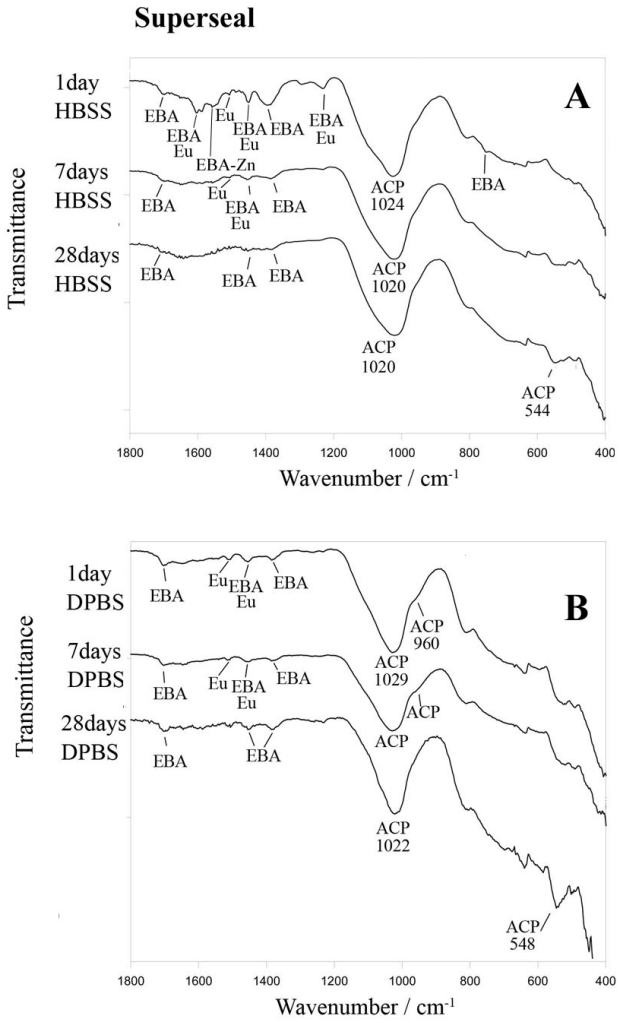

Figure 3.3: IR spectra recorded on the surface of SuperSeal after ageing in HBSS (A) and DPBS (B) for 1, 7 and 28 days. The bands assignable to eugenolate zinc salt (Eu), 2-ethoxybenzoic acid (EBA), 2-ethoxybenzoic zinc salt (EBA-Zn) and amorphous calcium phosphate (ACP) are indicated.

Figure 3.4A shows the IR spectra recorded on the surface of IRM after ageing in HBSS for 1, 7 and 28 days. Figure 3.4B shows the Raman spectra recorded on the same cement after ageing in HBSS for 28 days. The trend of the IR spectra recorded after ageing in both media was similar to that observed for SuperSeal; after 1 day of ageing in HBSS (Figure 3.4A) an amorphous calcium phosphate was present on the surface of the cement. The low crystallinity of the phosphate deposit is revealed by the low resolution of the phosphate bending mode that did not show distinct components at about 600 and 560 cm^{-1} (ν_4 PO_4). At increasing ageing times, the bands due to the material components progressively decreased in intensity, but remained still well detectable after 28 days of ageing. Analogous trends were observed after ageing in DPBS (spectra not shown). The Raman spectra confirmed these findings: after 28 days of ageing the band at about 970 cm^{-1} appeared strengthened due to the presence of an amorphous calcium phosphate.

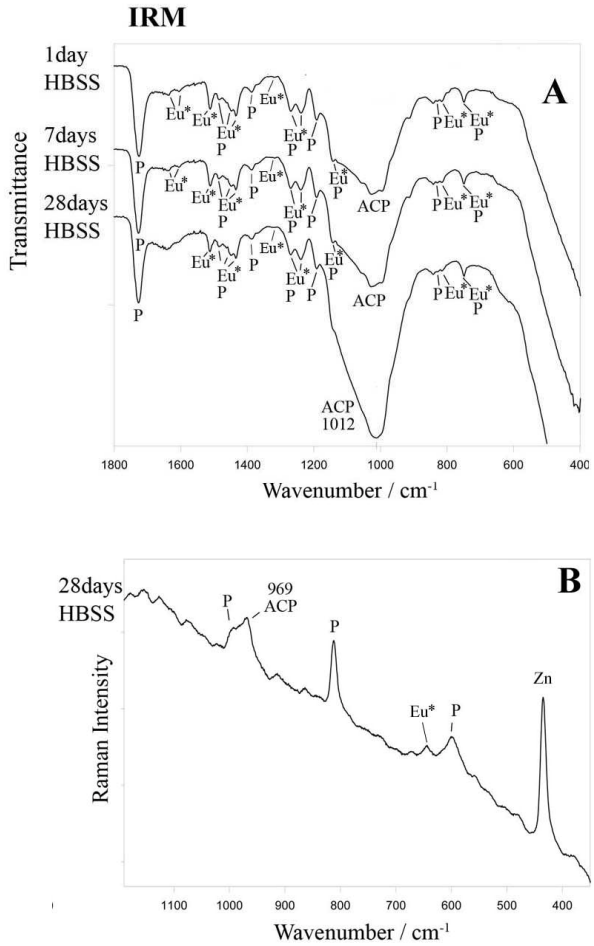

Figure 3.4: (A) IR spectra recorded on the surface of IRM after ageing in HBSS for 1, 7 and 28 days. (B) Raman spectra recorded on the surface of the same cement after ageing in HBSS for 28 days. The bands assignable to eugenolate zinc salt (Eu*), polymethylmethacrylate (P), zinc oxide (Zn) and amorphous calcium phosphate (ACP) are indicated.

Figure 3.5 shows the IR spectra recorded on the surface of Vitrebond after ageing in HBSS (A) and DPBS (B) for 1,7 and 28 days; Figure 3.5C shows the Raman spectra recorded on the surface of Vitrebond before (t = 0) and after ageing in HBSS and DPBS for 28 days. Upon ageing in HBSS, IR bands at about 1009-991 and 540 cm^{-1} appeared both on the

surface (Figure 3.5A) and in the interior of the cement (see below); an analogous result was obtained upon ageing in DPBS (Figure 3.5B), with the only difference that the former band was observed at 1017 cm^{-1}, i.e. at the same wavenumber position as after storage in water (see below). The Raman spectra did not show any significant band strengthening in the spectral range where phosphate modes fall, i.e. near 960 cm^{-1} (Figure 3.5C).

Upon ageing in both media, the IR bands at about 1555 and 1405 cm^{-1} assignable to poly-acrylate salt appeared particularly prominent (Figures 3.5A and 3.5B). Upon ageing in HBSS, the bands due to the poly-HEMA component were detectable only until 7 days (Figure 3.5A) while upon ageing in DPBS, they were clearly observable also after 28 days of ageing (Figure 3.5B).

Raman spectra (Figure 3.6) show the apatite formation on the surface of all the MTA cements after 1 day of incubation in DPBS.

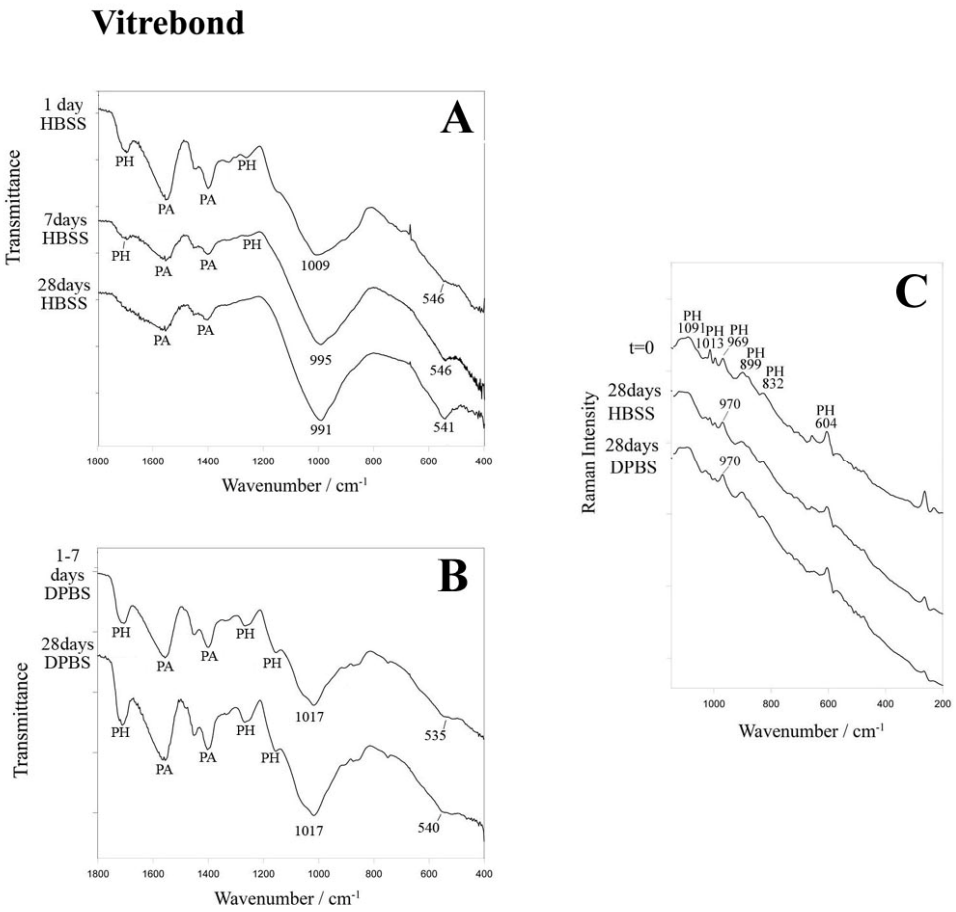

Figure 3.5: IR spectra recorded on the surface of Vitrebond after ageing in HBSS (A) and DPBS (B) for 1, 7 and 28 days; (C) Raman spectra recorded on the surface of Vitrebond after ageing in HBSS and DPBS for 28 days (the spectrum of the unaged material is reported as reference). The bands assignable to poly-HEMA (PH) and poly-acrylate (PA) are indicated.

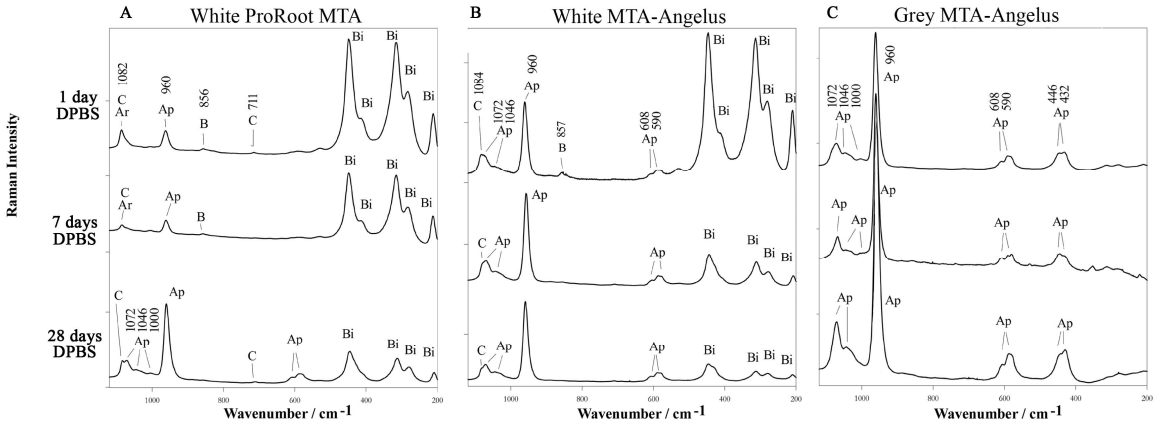

Figure. 3.6: Micro-Raman spectra recorded on the surface of the MTA cements soaked in DPBS for 1, 7 and 28 days: (A) White ProRoot MTA, (B), White MTA-Angelus and (C) Grey MTA-Angelus. The bands prevalently due to calcite (C), aragonite (Ar), apatite (Ap), alite (A), belite (B) and bismuth oxide (Bi) are indicated.

On the basis of the differences in the relative intensities, the thickest and most homogeneous deposit appeared on the Grey MTA-Angelus cement; after 1 day of storage in DPBS, the Raman spectrum of this sample (Figure. 3.6C) showed the bands typical of a B-type carbonated apatite at 1072 cm^{-1} (ν_3 PO_4 and ν_1 CO_3 in B-site), 1046 cm^{-1} (ν_3 PO_4), 960 cm^{-1} (ν_1 PO_4), 608–590 cm^{-1} (ν_4 PO_4) and 446–432 cm^{-1} (ν_2 PO_4) [26]. A weak band at 1000 cm^{-1}, assigned to the HPO_4^{2-} ion in HPO_4^{2-}containing apatites [27]**,** indicated the presence of HPO_4^{2-} ions in the apatite lattice. According to Labarthe et al. [28] the general formula of the deposited phase can be $Ca_{10-x}(PO_4)_{6-x}(CO_3^{2-}$ or $HPO_4^{2-})_x(OH)_{2-x}$ (with $0 \leq x \leq 2$). The bands due to cement components were undetectable, confirming that the deposit was thick enough to mask the underlying matrix. Differently, in the spectra of White ProRoot MTA (Figure. 3.6A) and White MTA Angelus (Figure 3.6B) the cement

components (belite and bismuth oxide) were observed, suggesting a thinner deposit on the materials other than Grey MTA-Angelus.

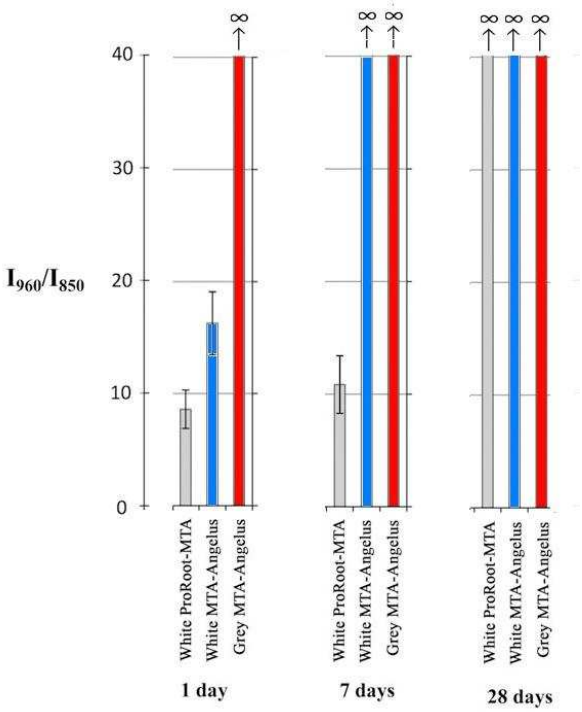

Figure 3.7: Trend of the I_{960}/I_{850} Raman intensity ratio (average ± standard deviation) calculated from the spectra recorded on the surface of the MTA cements at different times of incubation in DPBS.

In order to evaluate the deposit thickness, the I_{960}/I_{850} Raman intensity ratio was calculated from the spectra recorded on the upper surface of the samples. The trend of this parameter is shown in Figure 3.7: the thickness of the apatite deposit appeared to decrease along the series Grey MTA-Angelus > White MTA-Angelus > White ProRoot MTA. According to the increasing thickness of the deposit, after 28 days of ageing in DPBS, the bands of bismuth oxide were detected with decreasing relative intensity along the inverse series, i.e. White ProRoot MTA > White MTA-Angelus > Grey MTA-Angelus. With regards to Grey MTA-Angelus, the Raman spectra indicated the progressive maturation of the apatite

phase, since the band at about 1000 cm^{-1} decreased in intensity at 7 days and became undetectable at 28 days (Figure. 3.6C).

The IR spectra of the soaked samples confirmed the major bioactivity of the Grey MTA-Angelus cement (Figure 3.8).

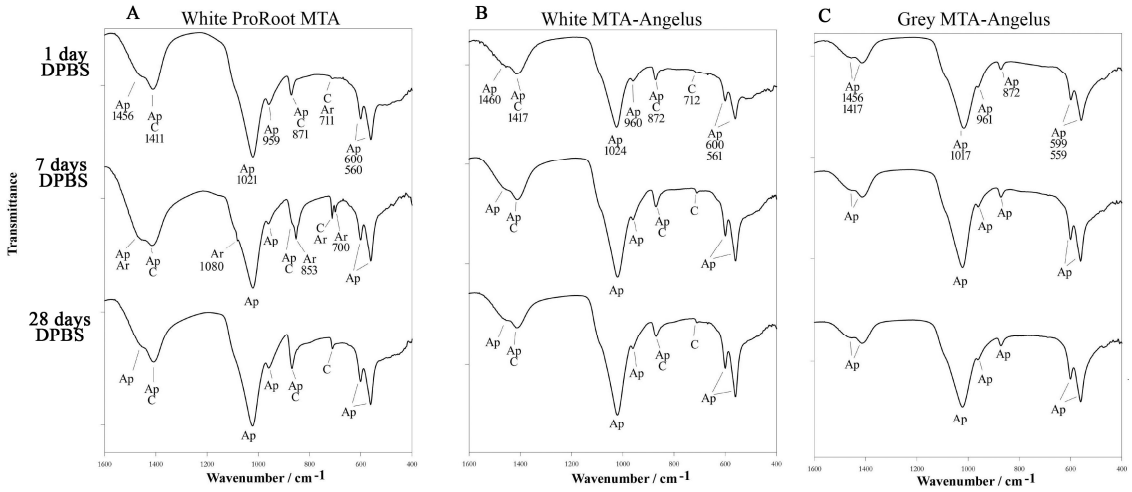

Figure 3.8: IR spectra recorded on the surface of the MTA cements soaked in DPBS for 1, 7 and 28 days: (A) White ProRoot MTA, (B), White MTA-Angelus and (C) Grey MTA-Angelus. The bands prevalently due to calcite (C), aragonite (Ar), and apatite (Ap) are indicated.

According to the Raman results, after one day of incubation in DPBS, in the IR spectrum recorded on its surface only the bands due to a B-type carbonated apatite at 1456 cm^{-1} (ν_3 CO_3), 1417 cm^{-1} (ν_3 CO_3), 1017 cm^{-1} (ν_3 PO_4), 961 cm^{-1} (ν_1 PO_4), 872 cm^{-1} (ν_2 CO_3), 599 cm^{-1} (ν_4 PO_4) and 559 cm^{-1} (ν_4 PO_4) were observed [26] (Figure 3.8C). Since no bands of the calcium silicates were detected, the deposit should be thicker than 2 μm which is the average IR penetration depth using a diamond crystal in the ATR technique. The deposit on Grey MTA Angelus appeared homogenous since all the recorded spectra were coincident.

The other MTA cements also formed a deposit constituted by B-type carbonated apatite and calcite (bands at about 1415, 870 and 711 cm^{-1} assigned to ν_3, ν_2 and ν_1 CO_3 vibrations) [29] (Fig. 3.8). In some single spectra recorded on the surface of White MTA-Angelus and White ProRoot MTA after one day of soaking, the presence of a shoulder at about 1110 cm^{-1} confirmed the formation of ettringite upon hydration [30] and then suggested a not homogeneous deposit, thinner than 2 μm. These features are not visible in Figure 3.8 where average spectra are shown.

After 7 days of soaking, no cement bands were detected in the IR spectra recorded on the surface of any of the cements, indicating a deposit thicker than 2 μm. On White ProRoot MTA a significant amount of aragonite was detected by the presence of the bands at 1455 cm^{-1}(ν_3 CO_3), 1080 cm^{-1}(ν_1 CO_3), 853 cm^{-1}(ν_2 CO_3), 711 cm^{-1} (ν_4 CO_3) and 700 cm^{-1}(ν_4 CO_3) [31-32]. At all incubation times, no calcium carbonate phase was detected on the surface of Grey MTA-Angelus.

Figure 3.9A shows the IR spectra recorded on the surface of White ProRoot MTA after ageing in HBSS for 1, 7 and 28 days. Figure 3.10B shows the Raman spectrum of the same cement after ageing in HBSS for 28 days.

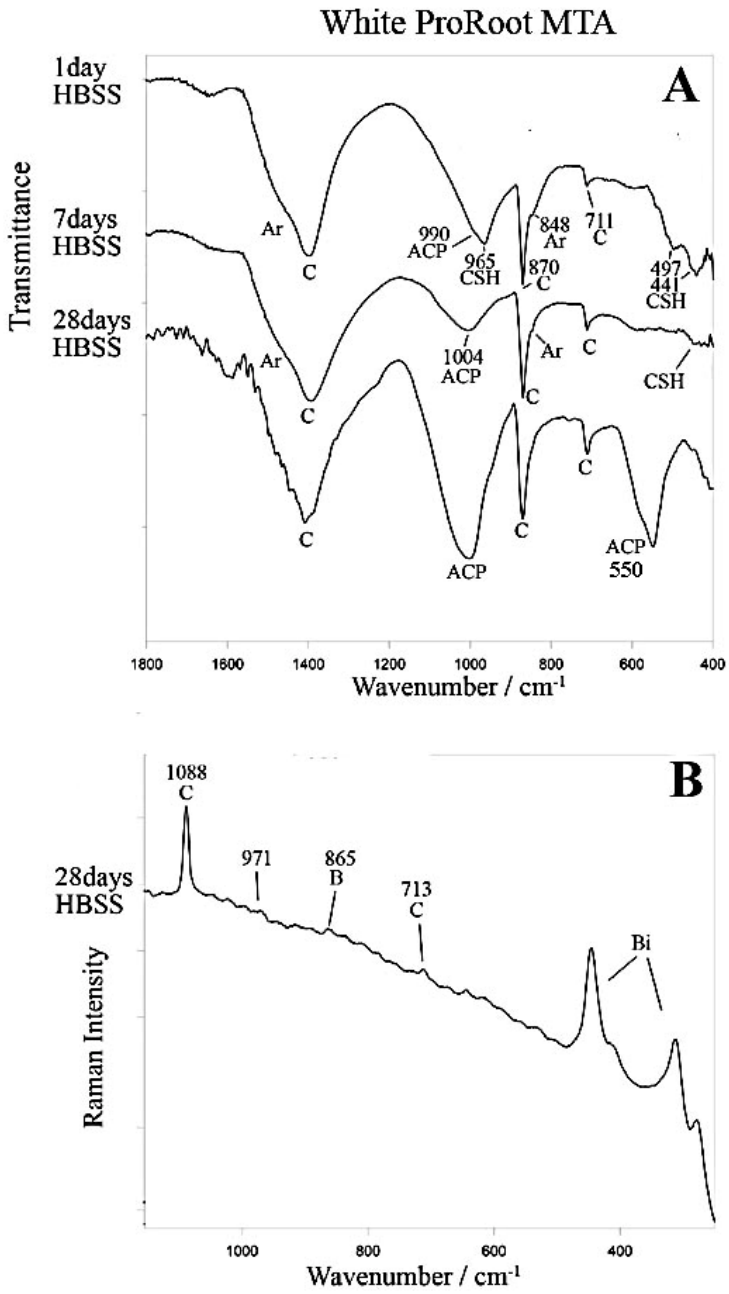

Figure 3.9: (A) IR spectra recorded on the surface of White ProRoot MTA after ageing in HBSS for 1, 7 and 28 days; (B) Raman spectrum of the same cement after ageing in HBSS for 28 days. The bands prevalently due to aragonite (Ar), calcite (C), belite (B), hydrated silicate gel (CSH), bismuth oxide (Bi) and amorphous calcium phosphate (ACP) are indicated.

Upon ageing in HBSS, White ProRoot MTA formed a coating of amorphous calcium phosphate (bands at about 1004 and 550 cm^{-1}) and calcium carbonate (as both calcite and aragonite) which progressively thickened at increasing ageing time, as revealed by the progressive disappearance of the bands due to the cement components (i.e. mainly CSH in the IR spectra, Figures 3.9A, and mainly belite and bismuth oxide in the Raman spectra, Figure 3.9B).

Spectra of the aged samples: inner fractured section

Figure 3.10 shows the IR spectra recorded in the inner fractured section of the SuperSeal cement after ageing in DPBS for 1 and 28 days.

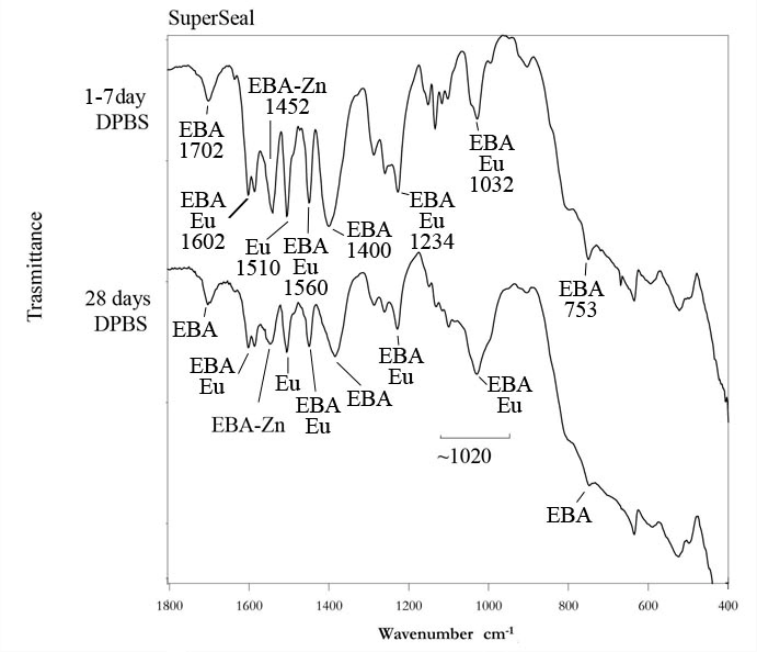

Figure 3.10: IR spectra recorded in the inner fractured side of the SuperSeal after ageing in DPBS for 1 and 28 days. The bands prevalently due to 2-ethoxybenzoic acid (EBA), 2-ethoxybenzoic zinc salt (EBA-Zn) and eugenol (Eu) are indicated.

The spectra recorded in the inner fractured section until 7 days of soaking in both media showed the same bands as the unaged material (see Figure 3.1); however, the band at 1452 cm^{-1}, assigned to the 2-ethoxybenzoic zinc salt, underwent a significant increase in intensity in both the media. With regards to DPBS, at longer ageing time (28 days), a weak broad feature at about 1020 cm^{-1} appeared, suggesting the formation of an amorphous calcium phosphate deposit also in the interior of the disk. This behaviour was not observed upon ageing in HBSS. The band of portlandite at about 3640 cm^{-1} (range not shown) was never detected at any ageing time and in any medium.

The Raman spectra of the fractured inner section were not considered because strongly affected by fluorescence interference.

The Raman and IR spectra recorded in the inner fractured section of the IRM samples aged in HBSS and DPBS, did not reveal any significant change with respect to those of the unaged material (Figures 3.1 and 3.2) and thus are not reported. The band of portlandite at about 3640 cm^{-1} (range not shown) was never detected at any ageing time and in any medium.

Figure 3.11A shows the IR spectra recorded in the inner fractured section of Vitrebond after ageing in DPBS for 1, 7 and 28 days. Upon ageing in DPBS, the IR spectra recorded in the interior and on the surface (Figure 3.5B) were coincident, as above reported. The IR bands at about 1017 and 550 cm^{-1} appeared also in the spectrum recorded on the surface of a reference sample aged for 1 day in water. (Figure 3.11B).

With regards to the HBSS ageing, the spectra recorded in the interior fractured section at any time of soaking were coincident with those recorded on the surface (Figure 3.5A).

The band of portlandite at about 3640 cm^{-1} (range not shown) was never detected at any ageing time and in any medium.

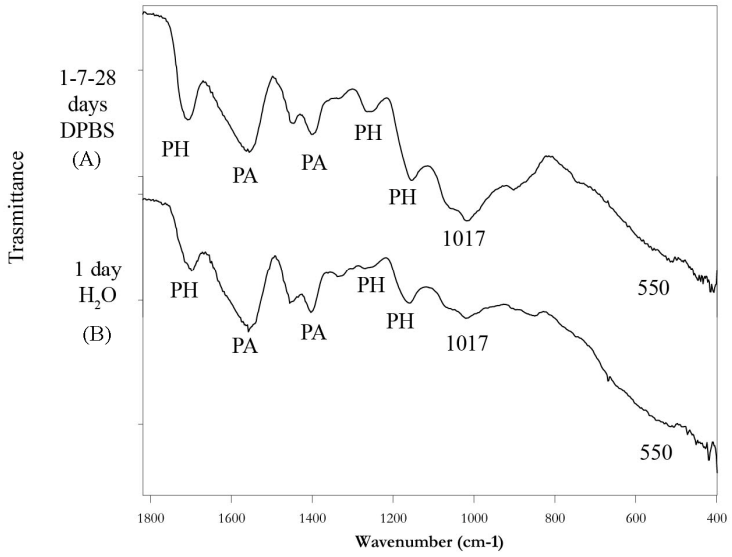

Figure 3.11: IR spectra recorded (A) in the inner fractured section of Vitrebond after ageing in DPBS for 1, 7 and 28 days and (B) on the surface of Vitrebond after ageing in H_2O for 1 day. The bands assignable to poly-HEMA (PH) and poly-acrylate (PA) are indicated.

Figure 3.12 shows the IR spectra recorded in the inner fractured section of the three MTA cements after ageing in DPBS for 1, 7 and 28 days. After 1 day of soaking in DPBS, the spectra of all the cements showed the bands of calcite (1418 cm^{-1}) and CSH component at about 940, 495 and 450 cm^{-1}.

White ProRoot MTA, and Grey MTA-Angelus showed a band at about 1110 cm^{-1} due to ettringite: according to the low sulphate content in the unhydrated powder of Grey MTA-Angelus, in this cement the component appeared with lower intensity. The band of ettringite was not observed in White MTA-Angelus, due to the absence of any sulphate

component in the unhydrated powder of this cement. On the other hand, the presence of a prominent band at about 800 cm^{-1} was assignable to cement hydration products and attributed to Si replacement by Al in tetrahedral sites of CSH [14]. The significant content of tricalcium aluminate in White MTA-Angelus powder supported this hypothesis. The sharp peak observed at about 420 cm^{-1} can be assigned to the lattice vibration (Ca-O) of hydrated tricalcium aluminate [32].

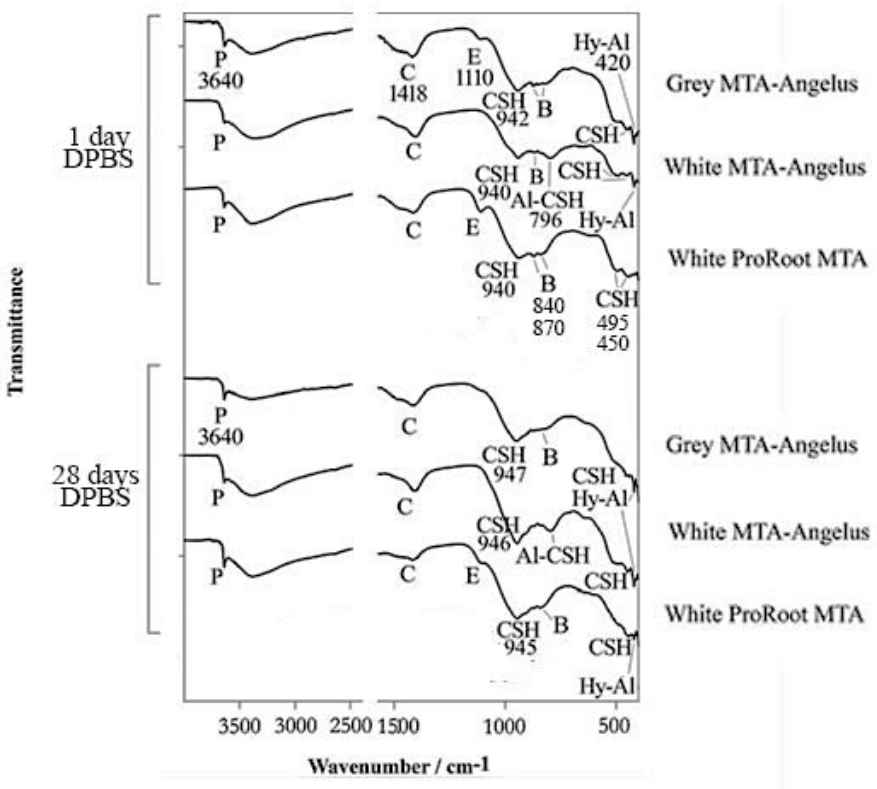

Figure 3.12: IR spectra recorded in the inner fractured section of the three MTA cements after ageing in DPBS for 1 and 28 days. The bands prevalently due to portlandite (P), calcite (C), ettringite (E), belite (B), hydrated silicate gel (CSH), hydrated tricalcium aluminate (Hy-Al), Al-substituted hydrated silicate gel (Al-CSH) are indicated.

After 28 day of soaking in DPBS, the position of the main CSH band showed an upshift to about 950 cm^{-1} due to the proceeding of the hydration process. Moreover, this band increased in intensity with respect to the belite band at about 840 cm^{-1}. Where present, the band of ettringite after 28 days was detected significantly decreased. The band at about 800 cm^{-1}, assigned to Al-substituted hydrated silicate gel, was observed as prominent component only in White MTA-Angelus.

The marker band of portlandite at about 3640 cm^{-1} (OH stretching mode) was observed in the interior of all incubated samples. The $Ca(OH)_2$ produced by the hydration process was detected only in the interior of the samples, but never on their surface, due to its release into the surrounding medium which underwent an increase in pH (see below). Upon ageing in DPBS (i.e. a calcium-free medium), this component was detected in all the cements until 28 days. Upon ageing in HBSS (i.e. a calcium-rich medium), portlandite was detected only until 7 days (see below, White ProRoot MTA).

Figure 3.13 shows the Raman spectra recorded in the inner fractured section of the MTA cements after ageing in DPBS for 1, 14 and 28 days.

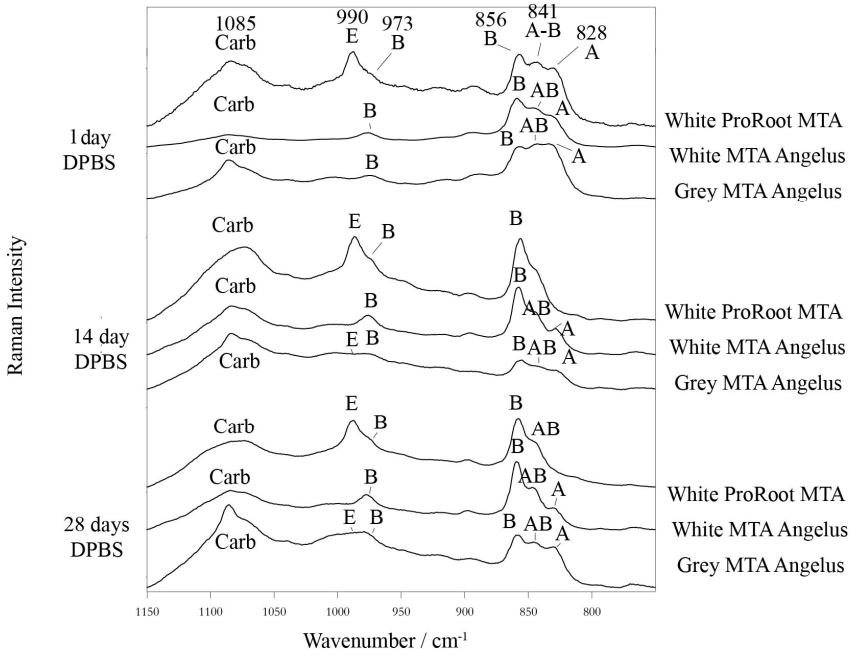

Figure 3.13: Micro-Raman spectra recorded in the inner fractured section of MTA cements after ageing in DPBS for 1, 14 and 28 days. The bands due to calcium carbonate (Carb), belite (B), alite (A) and ettringite (E) are indicated.

All the spectra showed the bands due to silicates at 973, 856, 841 and 828 cm^{-1} and the 1085 cm^{-1} component due to calcium carbonate. The ettringite band at 990 cm^{-1} was clearly observed in the interior of White ProRoot MTA at all ageing times. White MTA-Angelus did not show the presence of ettringite at any soaking time since its formulation did not contain any sulphate. Grey MTA-Angelus showed the appearance of ettringite as weak feature at 990 cm^{-1} only since 14 days of soaking, according to its low sulphate content. Moreover, upon ageing of all the cements, the alite band at 828 cm^{-1} progressively decreased in intensity with respect to the belite component, confirming the higher hydration rate of the former silicate [23,33-35].

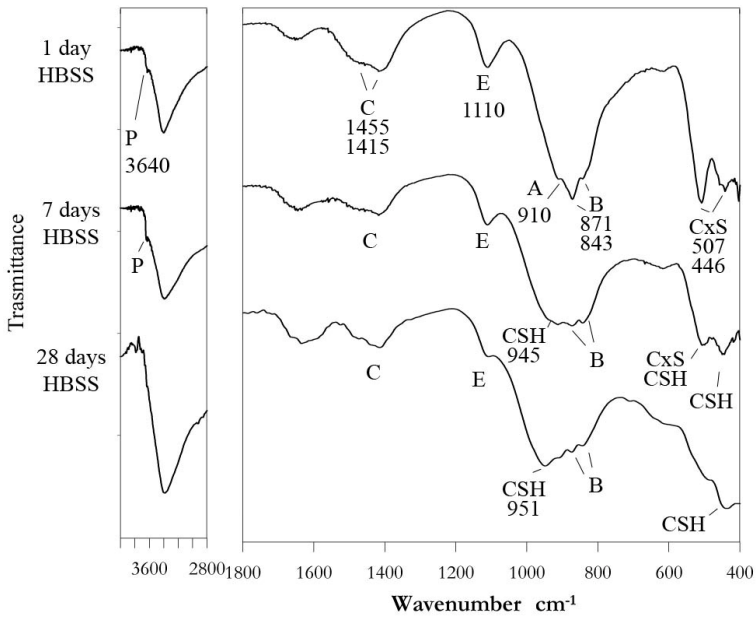

Figure 3.14: IR spectra recorded in the inner fractured section of White ProRoot MTA after ageing in HBSS for 1, 7 and 28 days. The bands prevalently due to portlandite (P), calcite (C), ettringite (E), belite (B), hydrated silicate gel (CSH) and fewly polymerized silicate tetrahedra (CxS) are indicated.

Figure 3.14 shows the IR spectra recorded in the inner fractured section of White ProRoot MTA after ageing in HBSS for 1, 7 and 28 days. The evolution of the IR spectra upon HBSS aging reflected the behavior observed for the aging in DPBS. However, the portlandite band at 3640 cm^{-1} was detected only until 7 days.

pH measurements of the ageing media

Figure 3.15 shows the trend of pH in the soaking media during ageing experiments.

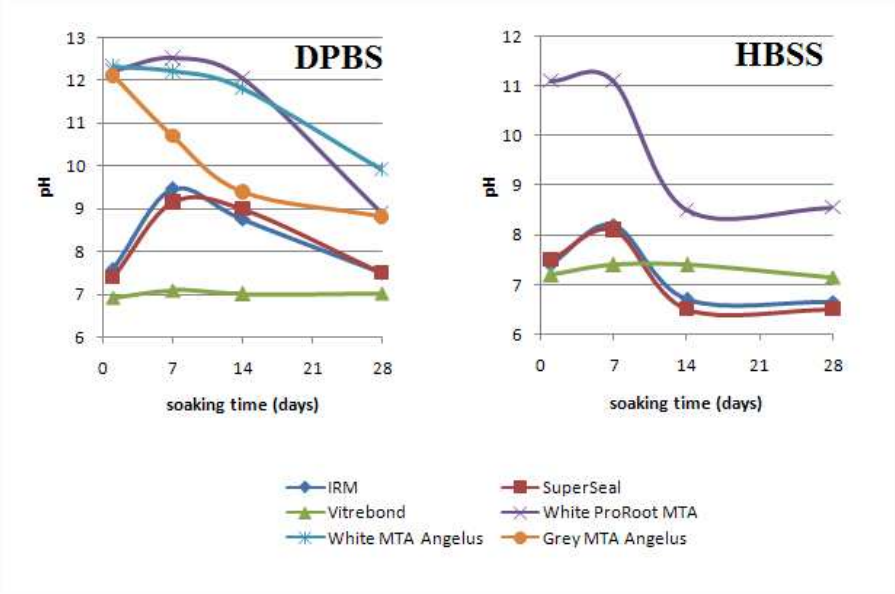

Figure 3.15: pH of the DPBS and HBSS soaking media after ageing of the studied materials for 1, 7, 14, and 28 days.

After 1 day of ageing in both media, the soaking solution of SuperSeal, IRM and Vitrebond maintained nearly the same pH as the buffered media (about 7.4), while for all the MTA cements a significant pH increase was detected (12 in DPBS and 11 in HBSS). At longer ageing times (28 days) all the materials, in all the media, presented a decrease of the pH values: SuperSeal, IRM and Vitrebond showed nearly neutral pH, while MTA cements still high values (about 9). Even if portlandite was not detected in IRM and SuperSeal samples, a significant pH increase was observed for both materials up to 14 days in DPBS and 7 days in HBSS.

3.4 Discussion

Since root-end filling materials are placed in close contact with living tissues and bone, they should be biocompatible and bioactive to allow osteoblasts proliferation and promote a fast bone regeneration.

Numerous materials have been used as root-end fillings. The ideal requirements for a root-end filler range from ease of handling to physical-chemical properties and biocompatibility. An important aspect that allows to obtain satisfactory results in endodontic treatments is the root-end filler capability to form apatite-like deposits when inserted in human body (bioactivity). The evaluation of the bioactivity of several materials commercially available can be useful to rate the product efficiency. Six root-end fillers were compared, belonging to three different classes: GIC, zinc oxide-eugenol cements and MTAs.

As described before (section 1.2.2), the formation of apatite deposits on MTAs is related to their release of calcium as product of the cement hydration process. The interaction between calcium ions and phosphate groups from the surrounding medium leads to the formation of calcium phosphate precipitates.

The calcium silicate MTA cements showed a marked higher bioactivity if compared with the other types of root-end fillers. In the MTA group differences in bioactivity kinetics have been highlighted.

The higher bioactivity of Grey MTA-Angelus can be explained in relation to its higher alite to belite ratio; a higher release of calcium hydroxide by alite with respect than by belite has been demonstrated [20]. Moreover, tricalcium aluminate has been reported to accelerate the hydration process [22]: the higher tricalcium aluminate content of White

MTA-Angelus cement with respect to White ProRoot MTA can explain the higher bioactivity of the former.

On the basis of the Raman results, for the MTA cements soaked in DPBS, the bioactivity decreased along the series: Grey MTA-Angelus > White MTA-Angelus > White ProRoot MTA.

Due to the lower bioactivity shown by White ProRoot MTA in DPBS, the influence of the soaking medium was analysed only for this cement and ageing studies in both HBSS and DPBS were carried out.

The vibrational data showed that the calcium phosphate deposit formed on White ProRoot MTA had a different nature in the two soaking media considered: in DPBS, a more crystalline B-type carbonated apatite formed since 1 day of ageing (Figures 3.8A), while in HBSS an amorphous calcium phosphate was detected (Figures 3.9A). This deposit matured into a more crystalline deposit at soaking times longer than 28 days as reported in a recent study [36]. Moreover, upon ageing in HBSS, the IR bands due to the material components were still visible after 7 days, while at the same time of ageing in DPBS were already undetectable. These trends demonstrated than in HBSS the bio-coating formation process was slower than in DPBS, producing thinner and less mature (i.e. amorphous) deposits, according to its lower phosphate content (0.776 mM *versus* 9.5 mM, see Table 1.2). Moreover, in HBSS the deposit appeared richer in the calcium carbonate component (as calcite and/or aragonite) than in the latter, due to the bicarbonate ion present in the medium composition.

IR spectra of the inner fractured sections revealed the formation of the classic products of calcium silicates hydration, i.e. CSH and $Ca(OH)_2$. Dissociation of calcium hydroxide into calcium and hydroxyl ions increases the pH.

CSH is a porous, fine-grained and highly disorganized hydrated silicate gel layer containing silanol groups (Si–OH) [37]. At the alkaline pH induced by $Ca(OH)_2$, the deprotonation of silanol groups should predominate [38] with the consequent formation of SiO^- negative groups: therefore the CSH particles show a very high negative charge density that attracts Ca^{2+} ions [39].

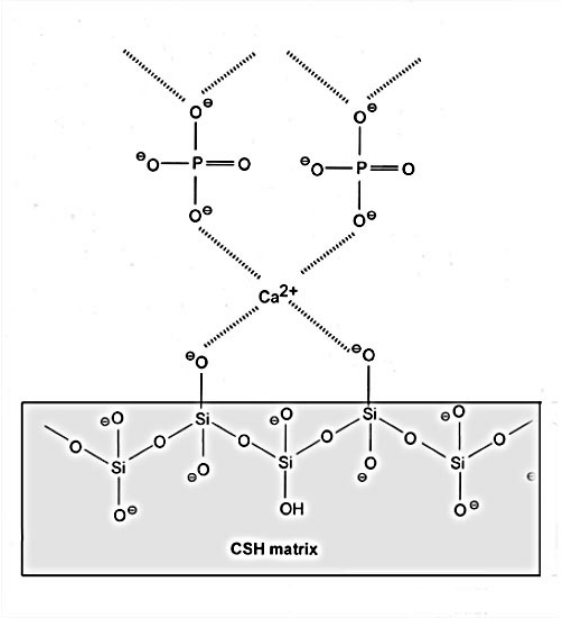

Figure 3.16: Schematic representation of heterogeneous nucleation of an apatite phase by interaction between the SiO^- groups of the CSH phase, Ca^{2+} and phosphate anions.

As shown in Figure 3.16, the SiO^- negative groups induce heterogeneous nucleation of apatite by bonding calcium ions on the silica-rich CSH surface: afterwards, calcium ions, interacting with phosphate anions present in the medium, form the apatitic phase [40].

Since apatite solubility decreases at higher pH (see Figure 1.1), the alkaline environment represents an ideal conditions for apatite deposition.

The formation of an osteoconductive apatite layer supports the osteoblast activity and spreading [41], while calcium release may induce osteoclast inhibition [42].

With regards to the sulphate component, its absence in the formulation of White MTA-Angelus and the low content in Grey MTA-Angelus is responsible for the null/lower amount of ettringite produced by these cements with respect to White ProRoot MTA (Figures 3.12 and 3.13). Sulphates decrease the hydration rate of calcium aluminates retarding the setting of the paste: the low amounts of sulphates detected in Angelus-MTA cements may explain the shorter setting times stated in the packaging brochure with respect to calcium sulphate-containing ProRoot MTA [43].

Another fundamental aspect involved in the use of root-end fillers is represented by the sealing ability: it has been demonstrated that apatite formation may contribute to improve the sealing ability of the cement aiding to fill the marginal porosity around restoration [44]. The ability to fill the marginal porosity may in part explain the better sealing ability that calcium silicate cements showed if compared with other root-end materials [45-47].

IRM and SuperSeal displayed the formation of significantly lower amounts of calcium phosphate deposits than MTA cements; the formation of a calcium phosphate deposit also in the calcium-free DPBS medium, suggests a certain ability of IRM and SuperSeal to release calcium. Differently from the analysed calcium silicate cements, the deposit was amorphous also after ageing in DPBS, suggesting a significantly slower bio-coating formation.

Based on the lower relative intensity of the IR bands due to the material components, it can be deduced that the deposit formed on SuperSeal was thicker than on IRM. No calcium

hydroxide was detected in the spectra recorded either on the surface or in the interior of these materials. Nevertheless a significantly basic pH was observed (Figure 3.15) for both SuperSeal and IRM up to 14 days in DPBS and 7 days in HBSS, due to the formation of a base other than portlandite during the setting process.

The low bioactivity of IRM and SuperSeal can be explained considering the potential chelation ability of the components present in the cements. ZnO hydration can form many Zn-OH groups that can induce apatite nucleation and thus trigger the formation of bone-like apatite on the surface of the cements, as proposed for similar systems [48].

Since eugenol can form a chelate with zinc ions [49], also a potential chelation of calcium ions can be supposed, due to the similarity in coordination number and ionic radius of the two ions. According to the literature [50], spectral features observed in the IR spectra of IRM (Figure 3.4A) are consistent with the formation of eugenolate calcium salt.

Since 2-ethoxybenzoic zinc salt was detected in SuperSeal (Figures 3.3 and 3.10), based on the previous considerations, an analogous calcium chelate formed by 2-ethoxy benzoic acid can be supposed [51] for SuperSeal cement.

The chelation of calcium ions by eugenol and 2-ethoxy benzoic acid can induce a heterogeneous nucleation of a mineral phase through the attraction of the phosphate anions present in the medium. This mechanism could explain the formation of the amorphous calcium phosphate deposits revealed by Raman and IR spectra recorded on the aged samples in both soaking media.

With regards to Vitrebond, the bands at about 1017 and 540 cm^{-1} (Figure 3.5 B) should not be ascribable to the formation of a calcium phosphate deposit because they were also observed in the interior of the samples and on the surface of a sample soaked in water (Figure 3.11). They could be rather assignable to the product of the reaction occurred in

water between the components already present in the cement formulation. Actually, as stated by its MSDS, Vitrebond does not contain calcium, so that it is not possible to observe bioactivity in a calcium-free medium such as DPBS.

The presence of calcium ions in the HBSS medium suggests that an amorphous calcium phosphate deposit could be formed (Fig. 3.5A). The formation of a deposit would be confirmed by the different relative intensity of the poly-HEMA bands in the different sample areas; the latter were observed with a significantly higher intensity in the interior than on the surface (Figures 3.5A and 3.11). The absence of bioactivity for experimental GIC with a different composition from Vitrebond has been demonstrated [52]. The limited bioactivity demonstrated by Vitrebond may be partially explained by the chemical behaviour of poly-HEMA and PAA, which showed a limited but not negligible bioactivity [53**].**

The tests performed suggest that zinc oxide-based cements and GIC, commonly used as root-end filling materials, have a very limited ability to induce apatite formation if compared to MTA cements. This low bioactivity represents a limitation in the use of these materials as root-end fillings since the large bone defect induced by apical infection and surgical procedures suggest the application of a biocompatible and bioactive material to promote a fast bone cellular response and to improve the healing and clinical success.

3.5 Conclusions

The Raman and IR spectroscopic analysis allowed to identify significant differences in the *in vitro* bioactivity of six commonly used root-end filling materials.

The results here reported demonstrated that calcium silicate MTA-based cements had the ability to induce a fast formation of a thick calcium phosphate/apatite bio-coating. In a phosphate-rich medium, such as DPBS, apatite deposition was faster than in a phosphate-poor medium such as HBSS.

Raman results indicated that after one day of soaking in DPBS the bioactivity of the three considered MTA cements decreased along the series: Grey MTA-Angelus > White MTA-Angelus > White ProRoot MTA. At longer incubation times the differences among the cements appeared less pronounced.

Thanks to the formation of apatite deposits, calcium silicate cements may promote bone regeneration: this characteristic makes MTA cements suitable in clinical situations where fast bone tissue formation is required.

The conventional root-end filling materials considered (i.e. IRM, SuperSeal and Vitrebond) showed only a modest and delayed formation of calcium phosphate deposits.

3.6 References

1. M. Bagby, E.H. Greener. *Dent. Mater.* 1985, **1,** 86.
2. A.D. Wilson, R.J. Mesley. *J. Dent. Res.* 1972, **51,** 1581.
3. B. Schrader, B. Dippel, I. Erb, S. Keller, T. Löchte, H. Schulz, E. Tatsch, S. *J. Mol. Struct.* 1999, **480,** 21.
4. M. Suzuki, H. Kato, S. Wakumoto. *J. Dent. Res.* 1991, **70,** 1092.
5. D. Belton, S.I. Stupp. *Macromolecules* 1983, **16,** 1143.
6. P. Taddei, F. Balducci, R. Simoni, P. Monti. J. *Mol. Struct.* 2005, **744,** 507.

7. S. Martinez-Ramirez, S. Sanchez-Cortes, J.V. Garcia Ramos, C. Domingo, C. Fortes, M.T. Blanco-Varela, *Cem. Concr. Res.* 2003, **33,** 2063

8. P. Taddei, A. Tinti, M.G. Gandolfi, P.L. Rossi, C. Prati. *J. Mol. Struct*. 2009, **924,** 548.

9. I. Lecompte, C. Henrist, M. Liegeois, A. Rulmont, R. Cloots, *J. Eur. Ceram. Soc*. 2006, **26,** 3789.

10. T.L. Hughes, C.M. Methven, T.G.J. Jones, S.E. Pelham, P. Fletcher, C. Hall, Adv. Cem. Based Mater. 1995, **2,** 91

11. M.I. Dominguez, J. Carpena, D. Borschnek, M.A. Centeno, J.A. Odriozola, J. Rose, *J. Hazard Mater.* 2008, **150,** 99.

12. H.W. Van der Marel, H. Beutelspacher, Atlas of Infrared Spectroscopy of Clay Minerals and their Admixtures, Elsevier, Amsterdam, 1976.

13. P. Tarte, *Spectrochim. Acta* 1967, **23A,** 2127.

14. A. Hidalgo, S. Petit, C. Domingo, C. Andrade, *Cem. Concr. Res.* 2007, **37,** 63.

15. P. Mondal, J.W. Jeffery, *Acta Cryst.* 1975, **B31,** 689

16. J.S. Song, F.K. Mante, W.J. Romanow, S. Kim, *Oral Surg. Oral Med. Oral Pathol. Oral Radiol. Endodontics* 2006, **102,** 809.

17. M. Conjeaud, H. Boyer, *Cem. Concr. Res.* 1980, **10,** 61.

18. J. Bensted, *J. Am. Ceram. Soc.* 1976, **59,** 140.

19. M. Tarrida, M. Madon, B. Le Rolland, P. Colombet, *Adv. Cem. Based Mater*. 1995, **2,** 15.

20. B.S. Hamad, *Adv. Cem. Based Mater.* 1995, **2,** 161.

21. H. Chang, P.J. Huang, S.C. Hou, Mater. *Chem. Phys.* 1999, **58,** 12.

22. L. Black, C. Breen, J. Yarwood, C.S. Deng, J. Phipps, G. Maitland, *J. Mater. Chem.* 2006, **16,** 1263.

23. D. Gastaldi, E. Boccaleri, F. Canonico, M. Bianchi, *J. Mater. Sci.* 2007, **42,** 8426.

24. J.D. Termine, A.S. Posner. *Science* 1966, **153,** 1523-1525.

25. N.J. Coleman, K. Awosanya, J.W. Nicholson. *J. Biomed. Mater. Res*. 2009, **90,** 166.

26. D.G.A. Nelson, J.D.B. Featherstone, *Calcif. Tissue Int.* 1982, **34,** S69.

27. R.M. Wilson, J.C. Elliott, S.E.P. Dowker, L.M. Rodriguez-Lorenzo, *Biomaterials* 2004, **25,** 2205.

28. J.C. Labarthe, G. Bonel, G. Montel, *Ann. Chim*. 1973, **8,** 289.

29. F.A. Andersen, L. Brecevic, *Acta Chem. Scand.* 1991, **45,** 1018.

30. M.Y.A. Mollah, W. Yu, R. Schennach, D.L. *Cocke, Cem. Concr. Res*. 2000, **30,** 267.

31. E.T. Stepkowska, J.M. Blanes, C. Real, J.L. Perez-Rodriguez. *J. Therm. Anal. Cal.* 2005, **82,** 731.

32. Z. Zakaria, J. Mihaly, I. Sajò, R. Katona, L. Haiba, F.A. Aziz, J. Mink, J. Coral. *J. Raman Spectrosc.* 2008, **39,** 1204

33. J. Plank, H. Keller, P.R. Andres, Z. Dai. *Inorg. Chim. Acta* 2006, **359,** 4901

34. S. Martinez-Ramirez,M. Frıas,C. Domingo, *J.RamanSpectrosc.* 2006, **37,** 555.

35. H. F. W. Taylor, *Cement Chemistry*, Academic Press: London, 1990

36. M.G. Gandolfi, P. Taddei, A. Tinti, E. Dorigo De Stefano, C. Prati. *Materials for Biological Applications*, 2011, **31,** 1412.

37. M.G. Gandolfi, P. Taddei, F. Siboni, E. Modena, G. Ciapetti, C. Prati. *Dent Mater.* 2011, **27,** 134.

38. F. Sanchez, L. Zhang. *J. Colloid Interf. Sci.* 2008, **323,** 349.

39. C. Plassard, E. Lesniewska, I. Pochard, A. Nonat. *Langmuir* 2005, **21,** 7263.

40. P. Zhu, Y. Masuda, T. Yonezawa, K. Koumoto. *J. Am. Ceram. Soc.* 2003, **86,** 782.

41. M.G. Gandolfi, G. Ciapetti, P. Taddei, F. Perut, A. Tinti, M.V. Cardoso, B. Van Meerbeek, C. Prati. *Dent Mater.* 2010, **26,** 974

42. D. Hashiguchi, H. Fukushima, H. Yasuda, W. Masuda, M. Tamikawa, K. Marikawa, K. Maki, E. Jimi. *J. Dent. Res.* 2011, **90,** 912.

43. Angelus. MTA Angelus: cimento reparador. Londrina: Angelus.

44. M.G. Gandolfi, C. Prati. *Int. Endod. J.* 2010, **43,** 889.

45. J.F. Reyes-Carmona, A.S. Santos, C.P. Figueiredo, C.H. Baggio, M.C. Felippe, W.T. Felippe, M.M. Cordeiro. *J. Endod.* 2010, **36,** 1347.

46. A. Fernández-Yáñez Sánchez, M.I. Leco-Berrocal,, J.M. Martínez-González. *Med. Oral. Patol. Oral. Cir. Bucal.* 2008, **13,** E180.

47. M. Torabinejad, M. Parirokh. *J. Endod.* 2010, **36,** 190.

48. Z. Li, L. Yubao, Z. Yi, W. Lan, J.A. Jansen J. Biomed. Mater. Res. 2010, **93A,** 269.

49. H.I.Copeland, G.M. Brauer, W.T .Sweeney, A.F. Forziati. *Bur. Stand. J. Res.* 1955, **55,** 133.

50. J. Margelos, G. Eliades, C. Verdelis, G. Palaghias. *J. Endod.* 1997 , **23,** 43.

51. N.J. Ray, B.J. Hathaway. *Acta Cryst.* 1981, **B37,** 1652.

52. J. Lööf, F. Svahn, T. Jarmar, H. Engqvist, C.H. Pameijer. *Dent. Mater.* 2008, **24,** 653.

53. C. Ohtsuki, Y. Aoki, T. Kokubo, Y. Bando, M. Neo, T. Nakamura. *J. Ceram. Soc. Jpn.* 1995, **103,** 449.

CHAPTER 4 - EXPERIMENTAL CALCIUM SILICATE CEMENTS

4.1 Introduction

The results reported in the previous chapter show that MTA cements are bioactive, to a higher extent than the non-MTA materials commonly used as root-end fillings. The formation of a bone-like apatite layer appears a significant advantage for new tissue formation and the integration in bone tissue.

On the other hand, one of the main disadvantages of calcium silicate MTA cements for endodontics is represented by their too extended setting time: one of the most used commercial materials, White ProRoot MTA, is characterized by an initial setting time of about 41 min and a final setting time of about 170 min [1]. In this light, the development of accelerated calcium silicate MTA cements as root-end filling materials is an attractive field: a reduced setting time will also overcome the problem of wash-out from the surgical site with increased potential clinical success.

This chapter deals with the characterization of two experimental cements named wTC and wTC-Bi, developed by Prof. C. Prati and Dr. M.G. Gandolfi (Laboratory of Biomaterials, Department of Odontostomatological Science, University of Bologna, Bologna, Italy), with the aim to conjugate the bioactivity properties of calcium silicates and the role of specific additives (such as $CaCl_2$) as setting accelerators. As for the MTA cements, the cement hydration and bioactivity upon ageing in DPBS was investigated *in situ* and in real time by micro-Raman spectroscopy, without sample manipulation and minimal interference from environmental water [2-3]. Micro-Raman configuration allows the detection of the changes in chemical composition on a microscale, because the laser spot size is of the order of few microns. The setup used to record micro-Raman spectra allows to analyse a thick depth of

sample, providing information on the evolution of the thickness of the apatitic deposit present on the cements surface. On the contrary, the ATR technique used to record the IR spectra allows to analyse a thinner layer of sample (2 µm) and thus proved more sensitive to detect the appearance of an apatitic phase at short ageing times.

The data obtained on the wTC and wTC-Bi cements were compared each other to obtain information on the possible influence of bismuth oxide on bioactivity and correlate this finding with the cell cultures experiments carried out at the Laboratory for Physiopathology of Orthopedic Implants, Istituto Ortopedico Rizzoli of Bologna (group of Prof. N. Baldini) aimed at investigating the effect of ageing of experimental calcium silicate cements on osteoblast viability and proliferation [4]. In the second part of this chapter, the data obtained for wTC-Bi were compared with those obtained for the radiopaque MTA cements analysed in the previous chapter.

4.2 Materials and Methods

Cements preparation and ageing experiments

The two experimental wTC and wTC-Bi calcium silicate cements were prepared at the Laboratory of Biomaterials, Department of Odontostomatological Science, University of Bologna, Bologna, Italy; they have been recently introduced to the market as Tech Biosealer Apex and Tech Biosealer RooEnd (Isasan, Italy), respectively.

The Portland-based calcium silicate powder (CEM I white Aalborg, Aalborg, Denmark) was thermally and mechanically treated, and added with 5% wt calcium chloride only for wTC and 5% wt calcium chloride and 17% wt of bismuth oxide for wTC-Bi. Calcium chloride is a well known setting accelerator [5] [6].

The cement powder was mixed with the already mentioned DPBS solution for 15 sec (powder/liquid ratio 3:1 by weight), then layered on a plastic coverslip (Thermanox, diameter 1.2 cm) to obtain standard disks. Mechanical vibrations were used to make the disk surfaces flat and regular, with a 1.1 ± 0.1 cm^2 exposed surface area. After preparation, the disks were immediately immersed in 5 mL of DPBS (15 mL of medium for 1 g of cement paste) and maintained at 37 °C. The samples were soaked in DPBS for different times (i.e. 5 hours, 1 day, 7, 14 and 28 days).

The storage media were renewed every week. At the endpoints, the medium was removed and its pH was measured using a glass electrode.

Spectroscopic measurements

The aged disks were analyzed by micro-Raman and ATR/FT-IR spectroscopy on their upper and inner fractured surfaces. The measurement conditions were the same described in Chapter 1. The spectra of the unhydrated cement powders and of the freshly prepared cements (i.e. 10' after preparation) were used for comparison. The spectra in the figures are representative of the obtained measurements. Intensity ratios were calculated as peak heights.

pH measurements

The pH of the soaking solutions was measured using a Denver Instrument Basic pH meter (Denver Instruments, Bohemia, NY, USA), equipped with a Hamilton liquid-glass electrode and ±0.01 resolution, which had previously been calibrated with acidic, neutral, and alkaline standard solutions. pH were tested at room temperature (24°C) after 1, 7, 14 and 28 days of incubation

4.3 Results

Characterization of the wTC and wTC-Bi unhydrated powders

Figure 4.1 shows the micro-Raman spectra recorded on the powders of the wTC and wTC-Bi unhydrated cements. The spectra of both the unhydrated powders revealed the presence of calcium carbonate (Carb), anhydrite (An), gypsum (G), belite (B) and alite (A), as shown by the respective marker bands indicated in the spectra [7-8**]**. The spectrum of unhydrated wTC-Bi showed at lower wavenumbers the strong bands assignable to bismuth oxide (Bi).

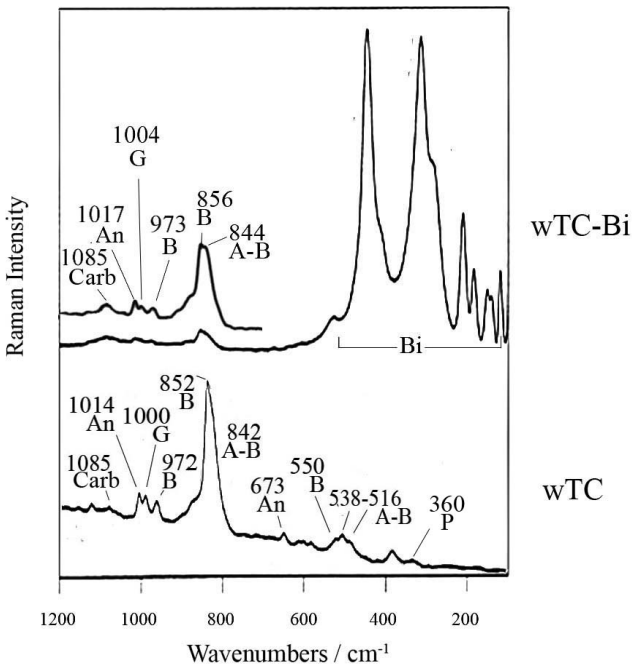

Figure 4.1: Micro-Raman spectra recorded on the unhydrated powders of the wTC and wTC-Bi cements. The bands due to belite (B), alite (A), anhydrite (An), gypsum (G), calcium carbonate (Carb), portlandite (P) and bismuth oxide (Bi) are indicated.

A weak feature at 360 cm^{-1} assignable to portlandite (P) was observed in the wTC Raman spectrum while it was undetectable in the wTC-Bi spectrum due to the presence of strong

bands due to Bi_2O_3. The lack of any band in the 700-750 cm^{-1} range indicates that neither tricalcium aluminate ($3CaO \cdot Al_2O_3$) nor aluminoferrite ($4CaO \cdot Al_2O_3 \cdot Fe_2O_3$) were detected.

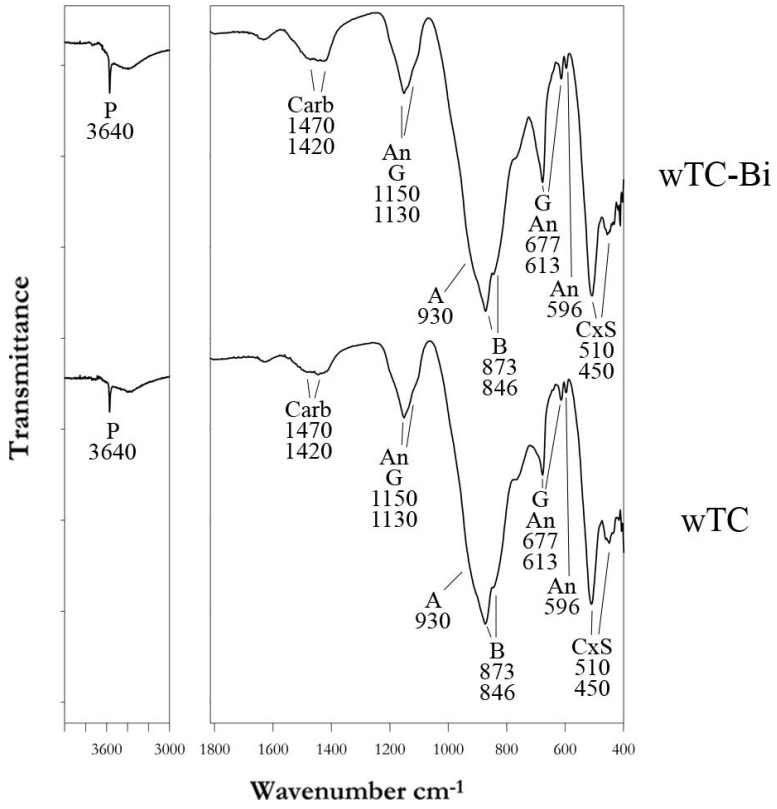

Figure 4.2: IR spectra recorded on the unhydrated powders of the wTC and wTC-Bi. The bands due to belite (B), alite (A), anhydrite (An), gypsum (G), calcium carbonate (Carb), portlandite (P) and fewly polymerised silicate tetrahedra (CxS) are indicated.

Figure. 4.2 shows the IR spectra recorded on the powders of the wTC and wTC-Bi unhydrated cements. The Raman findings on the composition of the cements were confirmed by IR spectroscopy. Bismuth oxide component was not detectable in the investigated spectral range. The IR spectra of both the unhydrated cements revealed the presence of portlandite (νOH band at 3640 cm^{-1}).

In both the spectra the bands at 510 and 450 cm^{-1} were present: they are assignable respectively to out-of-plane and in-plane bending modes of fewly polymerised silicate tetrahedra (CxS) [9**].** The band at 930 cm^{-1} was attributed to alite [10], and the components at about 873 and 846 cm^{-1} were assigned to belite [11].

The unhydrated powders of wTC and wTC-Bi cements contained calcium sulphate as both gypsum and anhydrite; the bands at 1150–1130 cm^{-1} (triply degenerate stretching mode), 677 and 613 cm^{-1} (bending modes) indicate calcium sulphate in the gypsum and anhydrite forms, while the component peak at 596 cm^{-1} is distinctive of anhydrite [12]**.**

Study of bioactivity: spectra recorded on the surface of the wTC and wTC-Bi aged cements

To evaluate the possible influence of bismuth oxide on bioactivity, micro-Raman and IR spectra of the two aged cements were compared. As revealed by the data reported in the previous chapter, micro-Raman spectroscopy proved more suitable to discriminate between differently bioactive cements, since it allows to analyse thicker depths of sample than IR spectroscopy. On the other hand, IR spectroscopy allows to detect earlier the formation of an apatite deposit.

Figures 4.3 and 4.4 show respectively the Raman spectra recorded on the surface of wTC and wTC-Bi cements freshly prepared (10') and after 5 hours, 1 day, 7, 14 and 28 days of soaking in DPBS.

Both the freshly prepared cements revealed the presence of ettringite (about 990 cm^{-1}), anhydrite (about 1015 cm^{-1}), gypsum (about 1000 cm^{-1}), alite and belite (852-842 cm^{-1} range), and calcium carbonate (about 1085 cm^{-1}). After 5 hrs of soaking in DPBS, an increment in the ettringite content occurred, as revealed by the increased relative intensity

of its marker band at 990 cm^{-1}. Since anhydrite hydrates more quickly than gypsum, its marker band at about 1015 cm^{-1} became nearly undetectable after 5 hrs of soaking. The band of alite appeared weakened with respect to that of belite, confirming its higher hydration rate. No apatite band was detected.

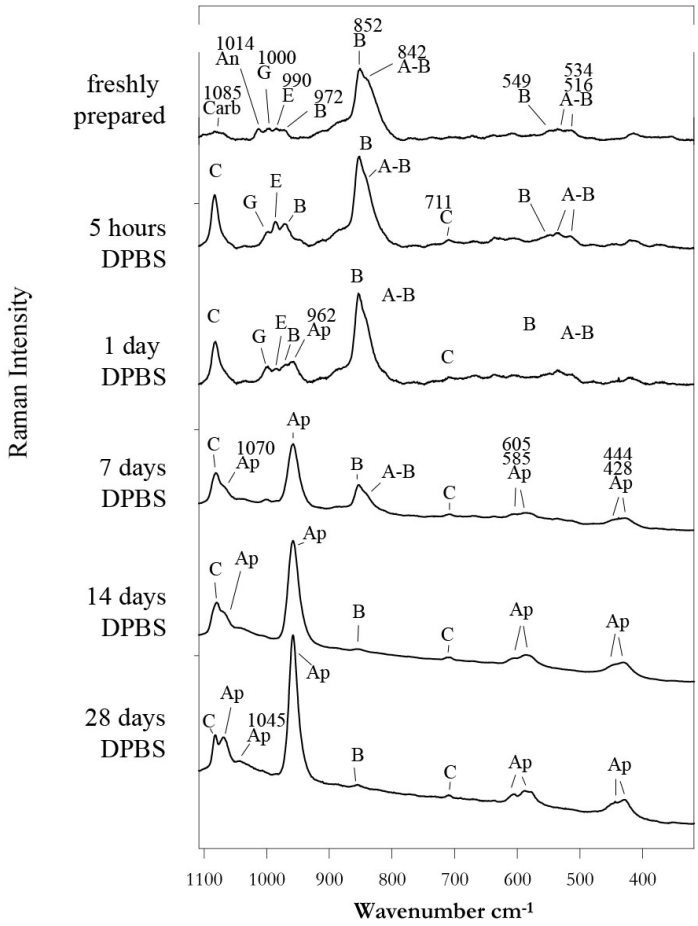

Figure 4.3: Micro-Raman spectra recorded on the surface of the wTC cement: freshly prepared (10') and after 5 hours, 1 day, 7, 14 and 28 days of soaking in DPBS. The bands due to belite (B), alite (A), anhydrite (An), gypsum (G), ettringite (E), calcium carbonate (Carb), calcite (C) and apatite (Ap) are indicated .

The spectra recorded on the surface of the cements soaked for 1 day in DPBS showed the presence of the marker band of ettringite (990 cm^{-1}), alite and belite (855-840 cm^{-1} range) and calcite and/or aragonite (about 1085 cm^{-1}). Both the cements showed the presence of a band at about 960 cm^{-1} due to calcium phosphate, indicating the presence of an apatite deposit [13]. The marker band of portlandite at 360 cm^{-1} [14] was never observed on the surface of wTC, due to its dissolution into the surrounding medium. The CSH component was not detected, because it is characterized by a weak spectrum as a result of its amorphous nature; it was revealed by IR spectroscopy (see below).

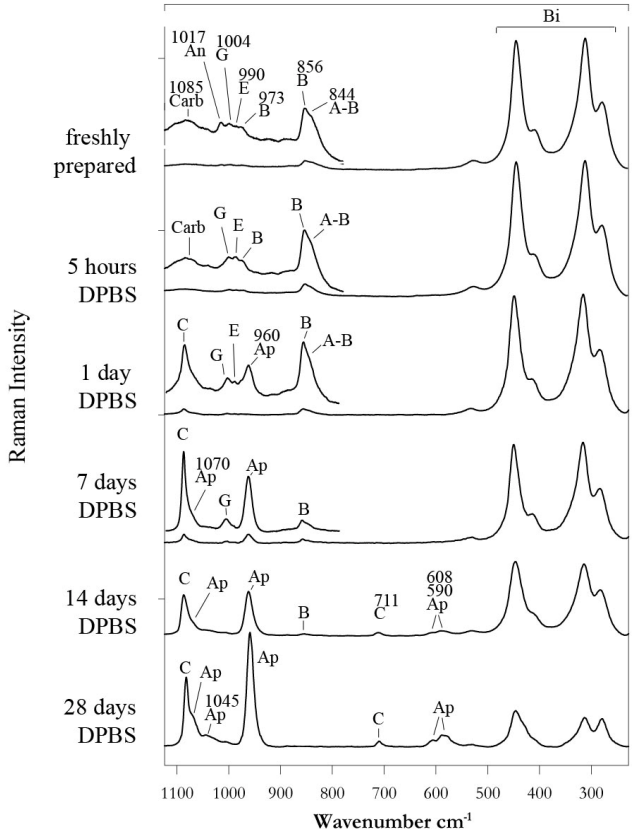

Figure 4.4: Micro-Raman spectra recorded on the surface of wTC-Bi cement: freshly prepared (10') and after 5 hours, 1 day, 7, 14 and 28 days of soaking in DPBS. The bands due to belite (B), alite (A), anhydrite (An), gypsum (G), ettringite (E), calcium carbonate (Carb), calcite (C), apatite (Ap) and bismuth oxide (Bi) are indicated .

At longer soaking times, the 960 cm^{-1} apatite band increased in intensity and after 7 days the 1075 cm^{-1} component typical of B-type carbonated apatite [13] appeared for both cements. Another spectral feature of this phase is the band at 1045 cm^{-1} [13], which was detected after 14 days for both cements. The sharp band at about 1085 cm^{-1} occasionally accompanied by the weak 711 cm^{-1} component revealed the presence of calcite. With regards to wTC-Bi, at increasing storage times, the marker bands of the bismuth oxide progressively decreased in intensity confirming an increase of the deposit thickness. After 7 days, the weaker components at about 605-585 and 445-430 cm^{-1}, assignable to the bending modes of phosphate, appeared in the spectra of wTC (Figure 4.3); the former bands appeared on wTC-Bi only after 14 days (Figure 4.4), while the latter were undetectable due to the interference of bismuth oxide.

Figures 4.5 and 4.6 show the IR spectra recorded on the surface of wTC and wTC-Bi cements, respectively, after 5 hours, 1 day, 7, 14 and 28 days of soaking in DPBS.

The IR analysis of the freshly prepared cements was not performed due to the high content of water that heavily affects the IR spectra.

After 5 hours of soaking in DPBS both the cements showed the presence of a band at 1110 cm^{-1} that confirms the presence of ettringite as hydration product [15]. Moreover, the spectral features around 950 and 500-450 cm^{-1} can be assigned to the CSH (hydrated silicate gel) phase formed upon hydration of the silicate component [15] and were detected in both cements.

The bands of belite at about 870 and 845 cm^{-1} were still observed. The components at about 1455, 1415, 870 and 711 cm^{-1} can be assigned to calcite. The presence of the band at 1470 cm^{-1} suggested also the presence of a low amount of aragonite. On the surface of

wTC, a deposit of B-type carbonated apatite formed as revealed by the characteristic components at 1455, 1415, 1027, 601, 562 cm^{-1} [13].

After 1 day of ageing the marker bands of B-type carbonated apatite were present in the spectra of both cements. Even if formed earlier, the deposit on wTC appeared thinner than on wTC-Bi, as revealed by the relative intensity of its bands with respect to those of CSH.

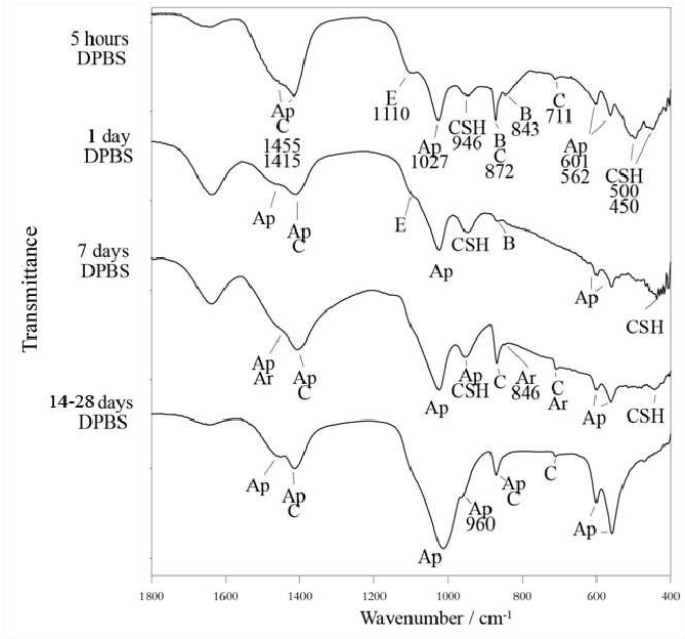

Figure 4.5: IR spectra recorded on the surface of wTC after 5 hours, 1 day, 7, 14 and 28 days of soaking in DPBS. The bands due to belite (B), ettringite (E), calcite (C), calcite (C), apatite (Ap) and hydrated silicate gel (CSH) are indicated

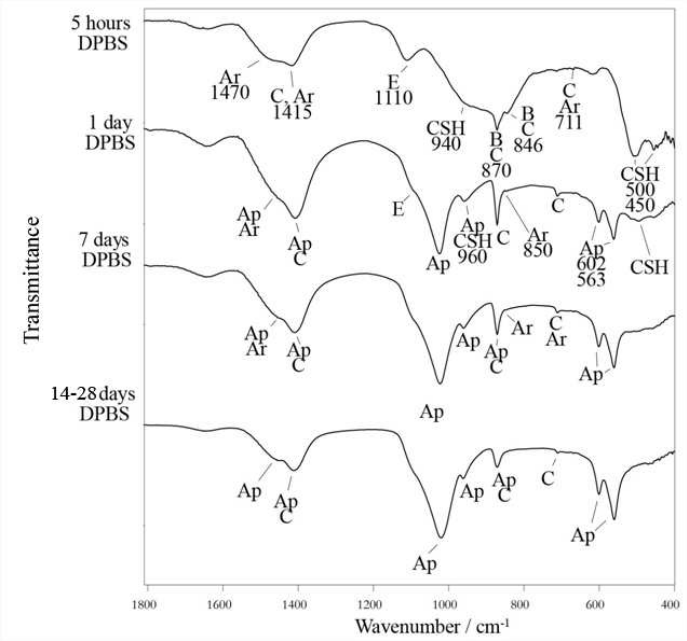

Figure 4.6: IR spectra recorded on the surface of wTC-Bi after 5 hours, 1 day, 7, 14 and 28 days of soaking in DPBS. The bands due to belite (B), ettringite (E), calcite (C), aragonite (Ar), apatite (Ap) and hydrated silicate gel (CSH) are indicated.

After 7 days of soaking in DPBS, a deposit thicker than 2 µm formed on wTC-Bi, since no bands of the underneath cement were observed; on the contrary, for wTC the IR components of CSH were still visible, suggesting a deposit thickness lower than 2 µm.

The spectra recorded on the surface of both wTC and wTC-Bi after 28 days displayed the bands of B-type carbonated apatite. No portlandite was detected at any ageing time, due to its release into the soaking medium.

Spectra of the aged samples: inner fractured section

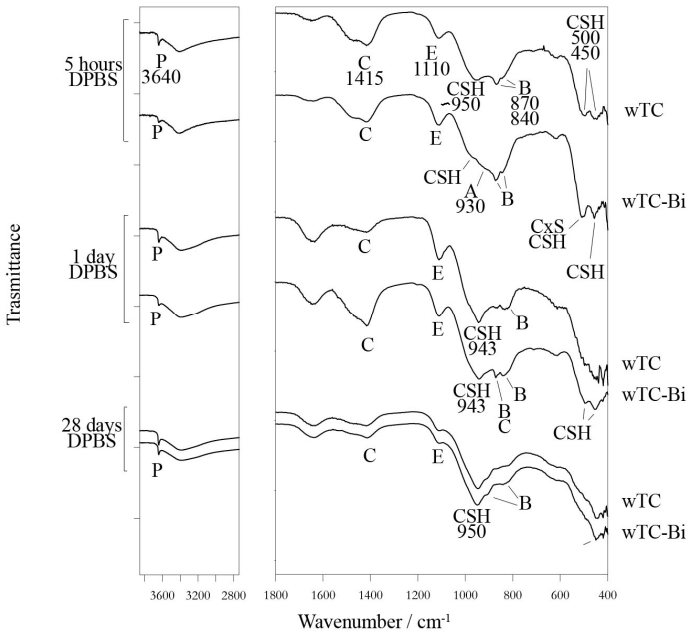

Figure 4.7: IR spectra recorded in the inner fractured section of wTC and wTC-Bi after ageing in DPBS for 5 hours, 1 day and 28 days. The bands prevalently due to portlandite (P), calcite (C), ettringite (E), alite (A), belite (B) and hydrated silicate gel (CSH) are indicated.

Figure 4.7 shows the IR spectra recorded in the inner fractured section of wTC and wTC-Bi after ageing in DPBS for 5 hours, 1 day and 28 days. The marker bands of portlandite at 3640 cm^{-1} and belite at 870 and 840 cm^{-1} were detected in the spectra of both cements at every ageing time as well as the bands of calcite (1415 cm^{-1} and occasionally 870 cm^{-1}). The spectral feature of ettringite (1110 cm^{-1}) was present already after 5 hours showing an increase in intensity after 1 day and a progressive decrease up to 28 days of soaking. The CSH component appeared in both cements since the early stages of ageing (i.e. 5 hours)

and was found to mature at longer ageing times, as revealed by the progressive up-shift of its marker band at about 945 cm^{-1}. At short ageing times (i.e. at 5 hours and 1 day), the reported spectra showed a less advanced stage of hydration in the wTC-Bi cement, as revealed by the lower intensity ratio between the bands of CSH and belite.

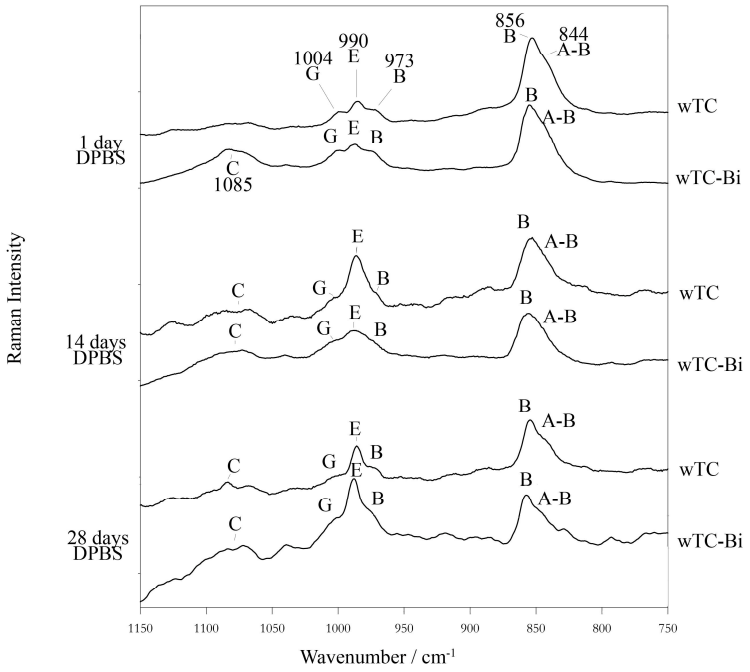

Figure 4.8: Micro-Raman spectra recorded in the inner fractured section of wTC and wTC-Bi after ageing in DPBS for 1 day, 14 and 28 days. The bands prevalently due to calcium carbonate (Carb), gypsum (G), ettringite (E), belite (B) and alite (A) are indicated.

Figure 4.8 shows the Raman spectra recorded in the inner fractured section of wTC and wTC-Bi after ageing in DPBS for 1 day, 14 and 28 days.

After 1 day the spectra were very similar for the two cements and showed some differences if compared with those recorded on the upper surface (Figure 4.3 and 4.4). In the wTC spectrum a prominent band at 360 cm^{-1}, attributable to portlandite was observable (spectral range not shown) confirming the IR data. This band was not detectable in the wTC-Bi

spectrum due to the overlapping of bismuth oxide bands. For both cements the band of ettringite at 990 cm^{-1} was clearly observed.

pH measurements of the ageing media

The pH values of the DPBS solutions where wTC and wTC-Bi aged for different times are reported in Table 4.1. Both the cements showed alkaline pH (i.e. ≥ 11) since early soaking times up to 14 days. After 28 days of soaking, the DPBS solution of wTC-Bi maintained higher pH values (11.8) than upon ageig of wTC (9.4).

	5 hours	**1 day**	**14 days**	**28 days**
wTC	11.7	12.2	11.0	9.4
wTC-Bi	11.7	12.3	11.7	11.8

Table 4.1: pH of the DPBS medium after immersion of wTC and wTC-Bi for 5 hours, 1 day, 14 and 28 days.

4.4 Discussion

As reported in chapters 1 and 3, MTA cements are used in a wide range of clinical applications including root-end filling and root perforation repair.

A root-end filling material should set immediately when placed in contact with oral hard tissues to allow dimensional stability of the restoration and to confer adequate strength to avoid displacement during restorative procedures.

One of the main defects of calcium silicate MTA cements for endodontic treatments is represented by their extended setting time that provide a poor handling [16]. To improve the physical and chemical properties of calcium silicate cements in regard to their relatively slow setting, $CaCl_2$ has been proposed as accelerating agent [17]

White ProRoot MTA, a widely used root-end material, exhibits initial and final setting times of about 41 and 170 min, respectively [1]. The wTC cement here described has significantly faster setting times (31 and 55 min, respectively) if compared with White ProRoot MTA. [1]**.**

The evaluation of the *in vitro* bioactivity of the experimental wTC cement, as well as its modified formulation added with bismuth oxide for radiopacity, was performed by micro-Raman and IR analysis with the aim to assess the influence of the latter component.

The first finding of this study is that both the experimental cements showed *in vitro* bioactivity when immersed in DPBS.

IR spectra revealed the formation of a B-type carbonated apatite layer (thinner than 2 µm) on the surface of the wTC cement already after 5 hours. On the wTC-Bi cement, the formation of an apatite deposit occurred later (1 day), but its thickness appeared higher. After 5 hours probably the deposit was not perfectly homogeneous, so that the IR spectra recorded on the latter cement may be considered not perfectly representative of the surface.

In the micro-Raman spectra the marker band of calcium phosphates at 960 cm^{-1} became detectable only after 1 day of ageing in DPBS because of the higher depth of penetration of the technique.

The addition of bismuth oxide did not significantly affect the apatite forming ability of the experimental cement; the IR spectra recorded in the inner fractured section at short ageing times revealed that in wTC-Bi the silicate hydration process was delayed if compared with wTC.

The presence of an extensive apatite layer has been reported to support osteoblast differentiation and adhesion, which favours bone bonding [18,19].

A cell culture study was carried out at the Laboratory for Physiopathology of Orthopedic Implants of Istituto Ortopedico Rizzoli in Bologna, with the aim of investigating the effect of ageing of wTC and wTC-Bi cements on osteoblast viability and proliferation [4]. Human marrow stromal cells (HMSC) were seeded on the cements freshly prepared and maintained in DPBS for different time periods (until 28 days) and cell viability was assessed. Surprisingly, these tests demonstrated that the proliferation of HMSC was higher on freshly prepared samples (i.e. with no content of apatite) than on aged samples (i.e. with a high content of apatite). Moreover, cell viability was decreased on the wTC-Bi cement, confirming the moderate cytotoxicity of bismuth oxide. Among the wTC.-Bi tested samples, those cultured after 28 days of ageing in DPBS showed the highest cell growth. This result can be explained in relation to the micro-Raman measurements, which showed a progressive decrease of the bismuth oxide bands at increasing ageing times as a result of the apatite deposit formation. Evidently, the adverse effect of bismuth oxide on cell growth was reduced by the formation of the apatite bio-coating.

Comparison with the MTA commercial cements

It appears interesting to compare wTC-Bi to the Bi_2O_3-containing commercial MTA cements described in Chapter 3.

The unhydrated powders of the cements showed several differences in composition. The main findings are summarized in Table 4.2; as can be easily seen, the major differences concern the calcium silicate, sulphate and aluminate components.

The cements appeared significantly different also with regards to the apatite-forming ability in DPBS, at short ageing times, at least. After 1 day of soaking, the I_{960}/I_{850} Raman intensity ratio (Figure 4.9), considered as an index of the deposit thickness, was lower for wTC-Bi than for the other cements, although the differences tended to decrease at longer ageing times. Table 4.2 reports that after 28 days of ageing, B-type carbonated apatite was present on the surface of all the cements.

The evolution of the hydration process observed by the IR analysis of the interior fractured section of the samples (Figure 3.13 and 4.7) showed a similar behaviour for wTC-Bi and the commercial materials. The data at 28 days of ageing are summarised in Table 4.2.

Portlandite formation was observed in all the cements at every ageing time; wTC-Bi showed the most alkaline medium after 28 days of ageing (Figure 4.10).

Cements.	Unhydrated powders	28 days DPBS soaking
Grey MTA-Angelus	Alite (predominant silicate component) Belite Calcium sulphate hemihydrate Tricalcium aluminate Tetracalcium aluminoferrite Portlandite Calcium carbonate Bismuth oxide	**Surface:** B-type carbonated apatite **Interior:** CSH phase Belite Ettringite Hydrated tricalcium aluminate Portlandite Calcite Bismuth oxide
White MTA-Angelus	Alite Belite (predominant silicate component) Tricalcium aluminate Portlandite Calcium carbonate Bismuth oxide	**Surface:** B-type carbonated apatite and calcite **Interior:** CSH phase Belite Hydrated tricalcium aluminate Al-substituted hydrated silicate gel Portlandite Calcite Bismuth oxide
White ProRoot MTA	Alite Belite (predominant silicate component) Anhydrite Portlandite Calcium carbonate Bismuth oxide	**Surface:** B-type carbonated apatite and calcite **Interior:** CSH phase Belite Ettringite Hydrated tricalcium aluminate Portlandite Calcite Bismuth oxide
wTC-Bi	Alite Belite (predominant silicate component) Anhydrite Gypsum Portlandite Calcium carbonate Bismuth oxide	**Surface:** B-type carbonated apatite and calcite **Interior:** CSH phase Belite Ettringite Hydrated tricalcium aluminate Portlandite Calcite Bismuth oxide

Table 4.2: Phases detected by Raman and IR spectroscopy in the unhydrated cements and after soaking in DPBS for 28 days.

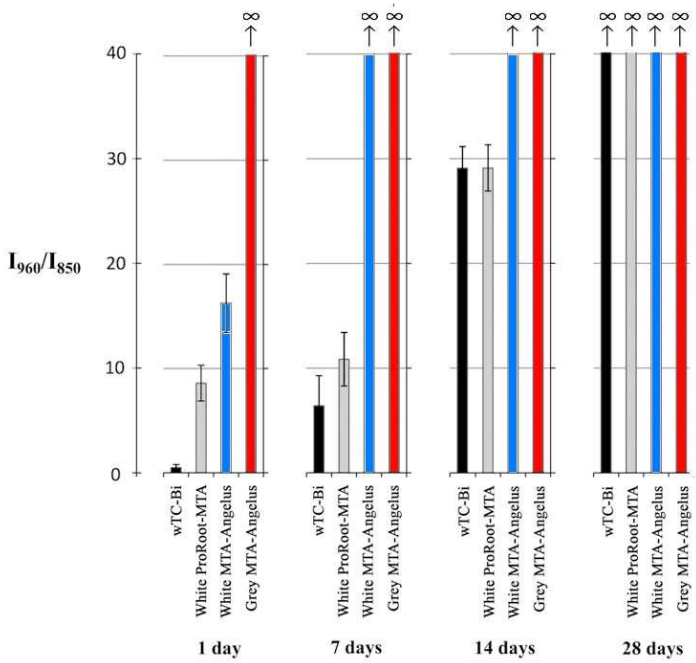

Figure 4.9: Trend of the I_{960}/I_{850} Raman intensity ratio calculated from the spectra recorded on the surface of the cements at different times of incubation in DPBS

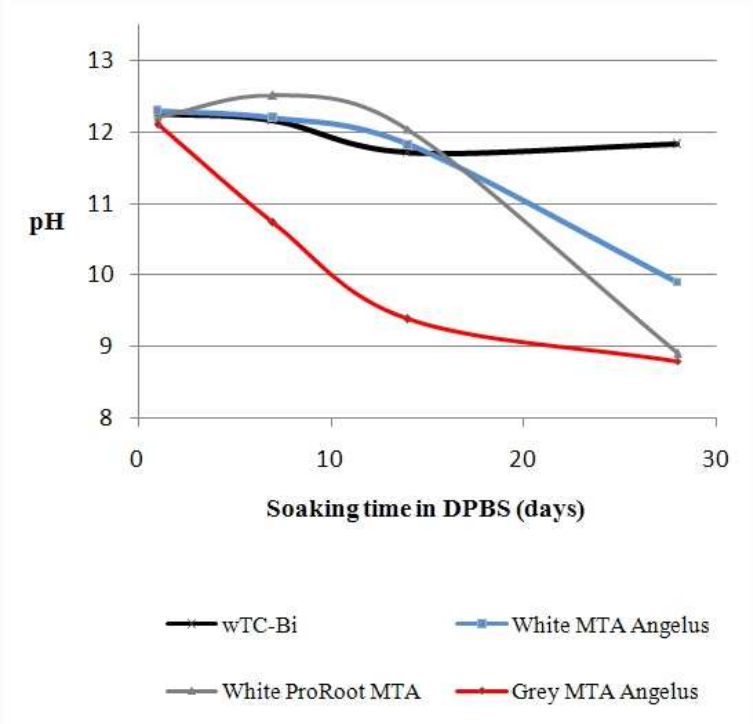

Figure 4.10: pH variations during DPBS soaking.

4.5 Conclusions

Two accelerated experimental MTA cements named wTC and wTC-Bi were characterized by micro-Raman and ATR/FT-IR spectroscopy.

The study demonstrated that these cements may promote the precipitation of a 'bone-like' apatite layer on the external surface when exposed to a simulated body fluid solution. The bioactivity of the wTC cement was not negatively affected by the presence of bismuth oxide.

If compared with the commercial MTA cements presented in chapter 3, wTC-Bi indicated a lower bioactivity in the first days of soaking. At longer incubation times the differences among the cements were less pronounced and the experimental accelerated wTC-Bi cement maintained a high bioactivity only slightly lower than the other commercial white calcium -silicate cements [20].

On the other hand, on the basis of the above mentioned cell culture studies [4], it can be affirmed that a too fast apatite formation may negatively affect cell adhesion and proliferation. In the light of this consideration, the experimental wTC-Bi cement appears a good alternative to commercial MTA cements.

3.5 References

1. M.G. Gandolfi, F. Iacono, K. Agee, F. Siboni, F. Tay, D.H. Pashley, C. Prati. *Oral. Surg. Oral. Med. Oral. Pathol. Oral. Radiol. Endod.* 2009, **108,** e39.
2. P. Taddei, A. Tinti, M.G. Gandolfi, P.L. Rossi, C. Prati. *J Mol. Struct*. 2009, **924-926,** 548.
3. S. Martinez-Ramirez, M. Frıas, C. Domingo. *J. Raman Spectrosc*. 2006, **37,** 555.

---

4. M.G. Gandolfi, F. Perut, G. Ciapetti, P. Taddei, E. Modena, P.L. Rossi, C. Prati, *J. Appl. Biomater. Biomech.* 2009, **7,** 160.

5. P. Kogan, J. He, G.N. Glickman et al. J. Endod, 2006, **32,** 569.

6. R. Abdullah, T.R. Pitt Ford, S. Papaioannou et al. *Biomaterials* 2002, **23,** 4001.

7. S. Martinez-Ramirez, M. Frıas, C. Domingo. *J. Raman Spectrosc*. 2006, **37,** 555.

8. S.S. Potgieter-Vermaak, J.H. Potgieter, R.Van Grieken. *Cem. Concr. Res.* 2006, **36,** 656.

9. I. Lecompte, C. Henrist, M. Liegeois, A. Rulmont, R. Cloots. *J. Eur. Ceram. Soc.* 2006, **26,** 3789.

10. T.L. Hughes, C.M. Methven, T.G.J. Jones, S.E. Pelham, P. Fletcher, C. Hall. *Adv. Cem. Based Mater.* 1995, **2,** 91.

11. M.I. Dominguez, J. Carpena, D. Borschnek, M.A. Centeno, J.A. Odriozola, J. Rose, *J. Hazard Mater.* 2008, **150,** 99.

12. H.W. Van der Marel, H. Beutelspacher, Atlas of Infrared Spectroscopy of Clay Minerals and their Admixtures, Elsevier, Amsterdam, 1976.

13. D.G.A. Nelson, J.D.B. Featherstone, *Calcif. Tissue Int.* 1982, **34,** S69.

14. C.S. Deng, C. Breen, J. Yarwood, S. Habesch, J. Phipps, B. Craster, G. Maitland, *J.Mat. Chem.* 2002, **12,** 3105.

15. M.Y.A. Mollah, W. Yu, R. Schennach, D.L. Cocke. *Cem. Concr. Res.* 2000, **30,** 267.

16. M. Torabinejad, N. Chivian. *J. Endod.* 1999, **25,** 197.

17. P. Kogan, J. He, G.N. Glickman, I. Watanabe .*J. Endod,* 2006, **32,** 569.

18. S.J. Ding, M.Y. Shie, C.Y. Wang, J. Mater. Chem. 2009, **19,** 1183.

19. A.E. Porter, C.M. Botelho, M.A. Lopes, J.D. Santos, S.M. Best, W. Bonfield. *J. Biomed. Mater. Res. A* 2004, **15–16,** 670.

20. P. Taddei, E. Modena, A. Tinti, F. Siboni, C. Prati, M.G Gandolfi. *J. Mol. Struct.* 2011, **993,** 367

CHAPTER 5 - EXPERIMENTAL FLUORIDE CONTAINING CALCIUM SILICATE CEMENTS

5.1 Introduction

In this chapter, a modified formulation of the wTC-Bi cement previously discussed is considered: different amounts of sodium fluoride were added to the wTC-Bi cement powder in order to evaluate its effect on bioactivity. It is well known that fluoride exhibits good biological activity on osteoblast and dental pulp cells [1-3].

On the basis of the good bioactivity of calcium silicate MTA cements, fluoride-doped MTA cements have been recently designed and studied.

It has been demonstrated that the addition of sodium fluoride 1% wt to calcium silicate powder causes a delay in the setting time and increases cement expansion [4] and long-term apical sealing ability in the root canal [5**]**.

The aim of this chapter was to evaluate the effect of the sodium fluoride amount added to wTC-Bi on the kinetics of apatite formation. The bioactivity of the experimental fluoride-doped calcium silicate cements was investigated after ageing in DPBS by micro-Raman and IR spectroscopy.

5.2 Materials and Methods

The composition of the wTC-Bi cement was reported in the material and methods section of chapter 4. Sodium fluoride 1% wt or 10% wt was added to wTC-Bi to produce two experimental fluoride-doped cements, identified as FTC-Bi and F10TC-Bi, respectively The two experimental cements were developed by Professor C. Prati and Dr. M.G.

Gandolfi at the Laboratory of Biomaterials, Department of Odontostomatological Science, University of Bologna

Cements disks were prepared and aged according to the previous procedures described in section 4.2. The disks were soaked in DPBS for 5 hours, 1 day, 7, 14, and 28 days.

The storage media were renewed every week. At the endpoints, the medium was removed and its pH was measured using a glass electrode. The deposit dispersed in the medium was filtered, dried and analyzed by IR spectroscopy.

Micro-Raman, FT-IR and pH measurements were carried out as described in chapter 4.

5.3 Results

To evaluate the effect of the sodium fluoride content on bioactivity, micro-Raman and ATR/FT-IR spectra were compared.

Figures 5.1 and 5.2 report the Raman and IR spectra recorded on the unhydrated powders of the F-doped cements. Bands were assigned, as reported in chapters 3 and 4, according to the literature.

The Raman spectra of FTC-Bi and F10TC-Bi were practically coincident each other and with the spectrum of undoped wTC-Bi reported in Figure 4.1, since the marker band of NaF fell around 200 cm^{-1} and was covered by bismuth oxide strong features.

The spectra showed the presence of calcium carbonate (band at 1088 cm^{-1}), calcium sulphate as both anhydrite (band at 1017 cm^{-1}) and gypsum (band at 1003 cm^{-1}), alite (band at 845 cm^{-1}), belite (bands at 855 and 845 cm^{-1}) and bismuth oxide (bands below 600 cm^{-1}).

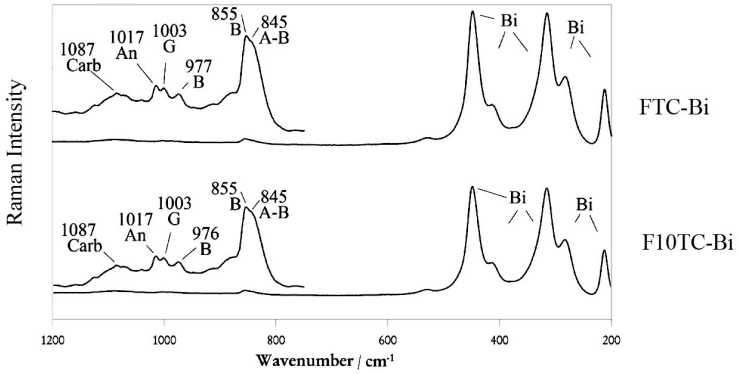

Figure 5.1: Micro-Raman spectra recorded on the unhydrated powders of the F-doped cements. The bands due to calcium carbonate (Carb), anhydrite (An), gypsum (G), belite (B), alite (A) and bismuth oxide (Bi) are indicated.

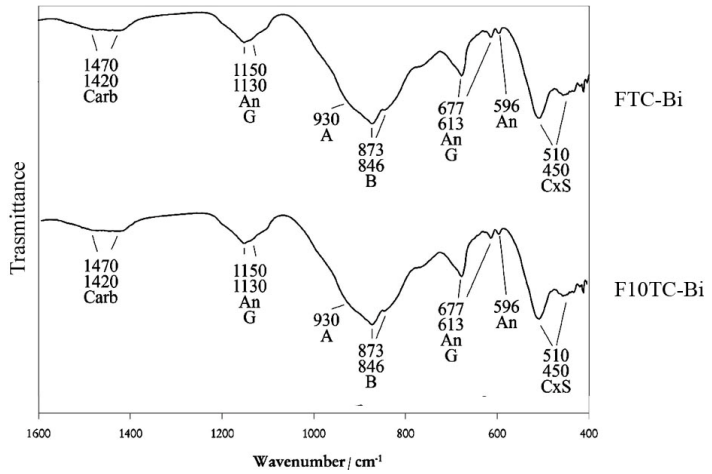

Figure 5.2: IR spectra recorded on the unhydrated powders of the F-doped cements. The bands due to calcium carbonate (Carb), gypsum (G), anhydrite (An), alite (A), belite (B) and fewly polymerized silicates (CxS) are indicated.

As observed for Raman analysis, the IR spectra of FTC-Bi and F10TC-Bi coincided with that recorded on the unhydrated powder of wTC-Bi reported in Figure 4.2, since NaF does not absorb in the considered spectral range. The spectra showed the presence of calcium

carbonate (bands at 1470 and 1420 cm^{-1}), calcium sulphate as both anhydrite (bands at 1150, 1130, 677, 613 and 596 cm^{-1}) and gypsum (bands at 1150, 1130, 677 and 613 cm^{-1}), alite (band at 930 cm^{-1}), belite (bands at 873 and 846 cm^{-1}) and fewly polymerized calcium silicate (bands at 510 and 450 cm^{-1}).

Study of bioactivity: spectra recorded on the surface of the aged samples and on the powders isolated from the ageing media

Figures 5.3 and 5.4 show the Raman spectra recorded on the freshly prepared cements and after ageing in DPBS up to 28 days.

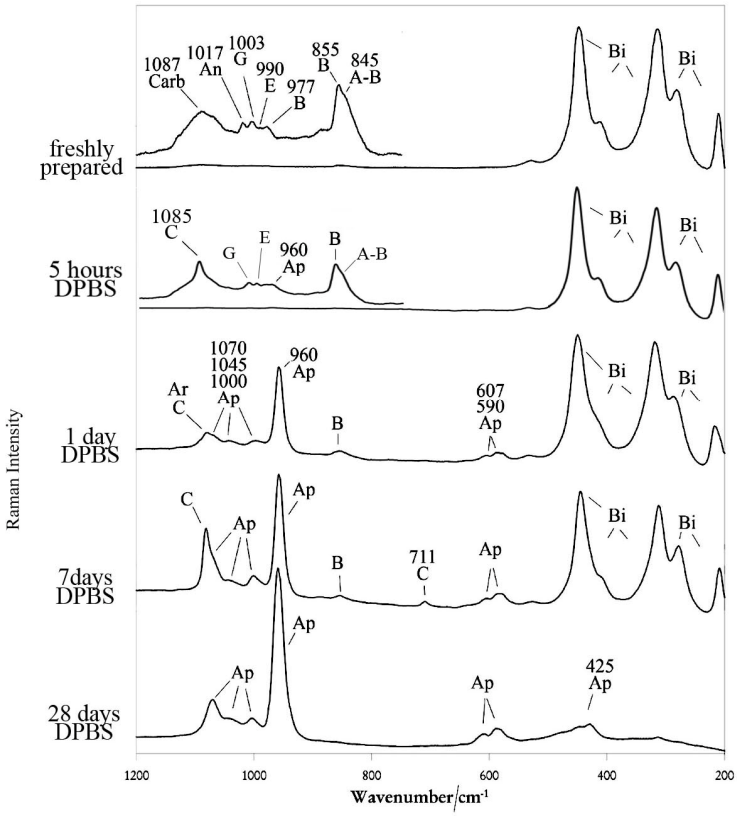

Figure 5.3: Micro-Raman spectra recorded on the surface of the FTC-Bi cement freshly prepared and after ageing in DPBS for 5 hours, 1 day, 7 and 28 days. The bands due to

calcium carbonate (Carb), calcite (C), apatite (Ap), belite (B) ettringite (E), gypsum (G), anhydrite (An) and bismuth oxide (Bi) are indicated.

The freshly prepared samples revealed the appearance of the marker band of ettringite at about 990 cm^{-1}, particularly strong on the F10TC-Bi cement. After 5 hours of ageing in DPBS, the band at 960 cm^{-1}, due to the presence of an apatite deposit, was observed on both cements: its relative intensity with respect to the main belite component at 855 cm^{-1} was higher in the spectrum of F10TC-Bi where the band at 1070 cm^{-1} (typical of B-type carbonated apatite) was also observed. The band at 1000 cm^{-1} can be assigned to the presence of HPO_4^{2-} ions in the apatite lattice.

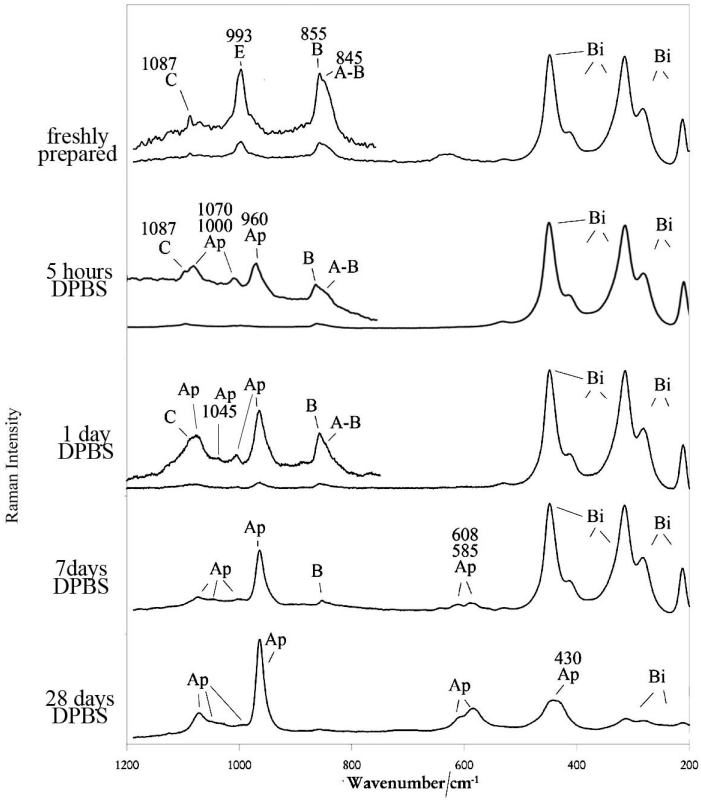

Figure 5.4: Micro-Raman spectra recorded on the surface of the F10TC-Bi cement freshly prepared and after ageing in DPBS for 5 hours, 1 day, 7 and 28 days. The bands due to

calcite (C), apatite (Ap), alite (A), belite (B) ettringite (E) and bismuth oxide (Bi) are indicated.

After 1 day of ageing in DPBS, the Raman spectrum recorded on FTC-Bi clearly showed the bands typical of a HPO_4^{2-}containing B-type carbonated apatite at 1070, 1045, 1000, 960, and 607–590 cm^{-1}. The intensity ratio between the bands of apatite and belite (at about 960 and 855 cm^{-1}, respectively) was considered as a marker of the thickness of the apatite deposit. This ratio was higher on the FTC-Bi cements than on F10TC-Bi. Moreover, the 960 cm^{-1} apatite band was broader on F10TC-Bi than on FTC-Bi, up to 7 days of ageing.

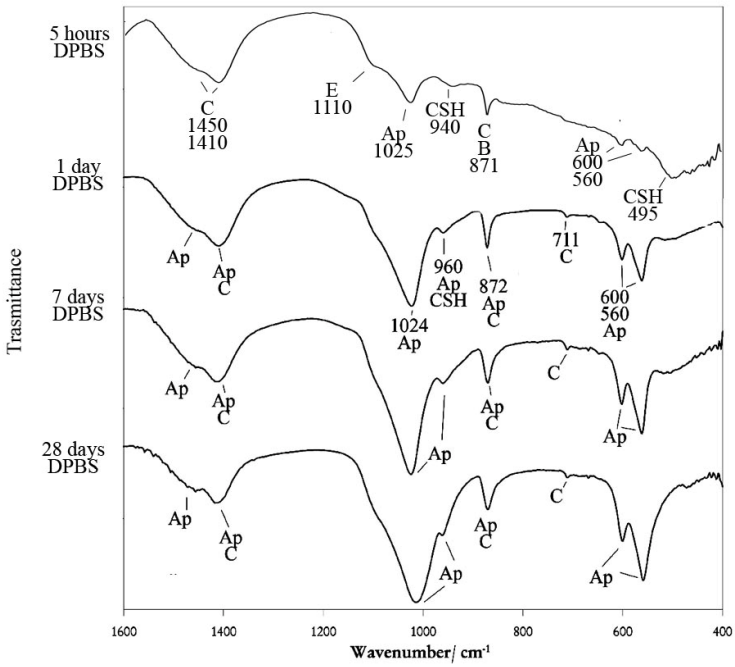

Figure 5.5: IR spectra recorded on the surface of the FTC-Bi cement after ageing in DPBS for 5 hours, 1 day, 7 and 28 days. The bands due to calcite (C), apatite (Ap), belite (B), ettringite (E) and hydrated silicate gel (CSH) are indicated.

As observed for the wTC-Bi cement in chapter 4, at increasing storage times, the bands of the cement progressively weakened, while the bands typical of a B-type carbonated apatite progressively strengthened.

After 28 days of ageing, the bands of bismuth oxide were observed with lower intensity in FTC-Bi than F10TC-Bi.

Figures 5.5 and 5.6 show the IR spectra recorded on the surface of the cements after ageing in DPBS for 5 hours, 1 day, 7 and 28 days.

According to Raman results, the presence of the apatitic deposit was observed on both cements since 5 hours of soaking in DPBS (bands at about 1020, 600 and 560 cm^{-1}). At this time a shoulder at about 1110 cm^{-1} appeared, confirming the formation of ettringite.

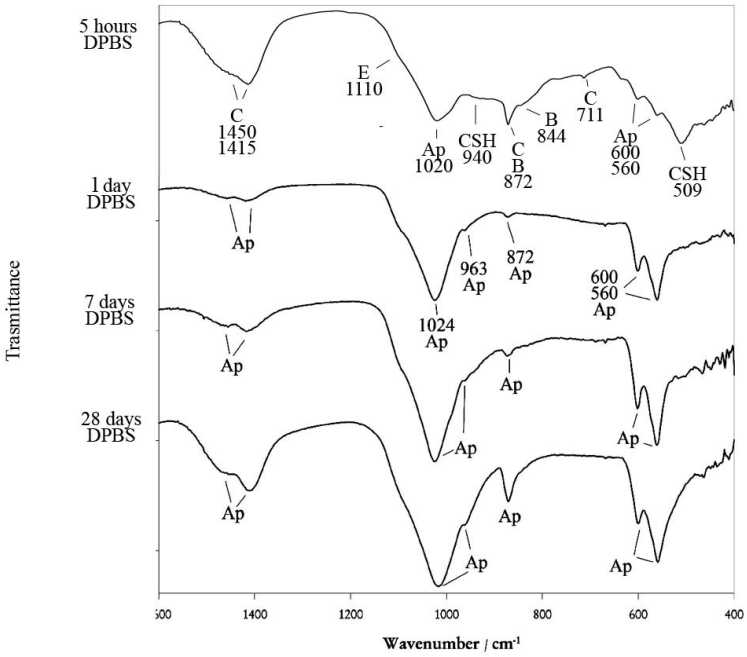

Figure 5.6: IR spectra recorded on the surface of the F10TC-Bi cement after ageing in DPBS for 5 hours, 1 day, 7 and 28 days. The bands due to calcite (C), apatite (Ap), belite (B), ettringite (E) and hydrated silicate gel (CSH) are indicated.

After 1 day of ageing in DPBS, the spectra recorded on the surface of FTC-Bi and F10TC-Bi surfaces did not show any band of the underlying cement, indicating that the deposit was thicker than 2 µm; it was mainly constituted by B-type carbonated apatite (bands at about 1450, 1410, 1024, 960, 872, 600 and 560 cm^{-1}) and calcite.

The apatite bands on F10TC-Bi were broader than on FTC-Bi (in particular those at 1024 and 963 cm^{-1}), according to the Raman findings. The same behaviour was observed after 7 and 28 days of ageing.

To gain more insights into the formed apatitic deposit, IR spectra of the powders isolated from the ageing media were measured. Figure 5.7 shows the IR spectra recorded on the powders isolated from the soaking media where wTC-Bi, FTC-Bi and F10TC-Bi aged for 1 day, 7 and 28 days.

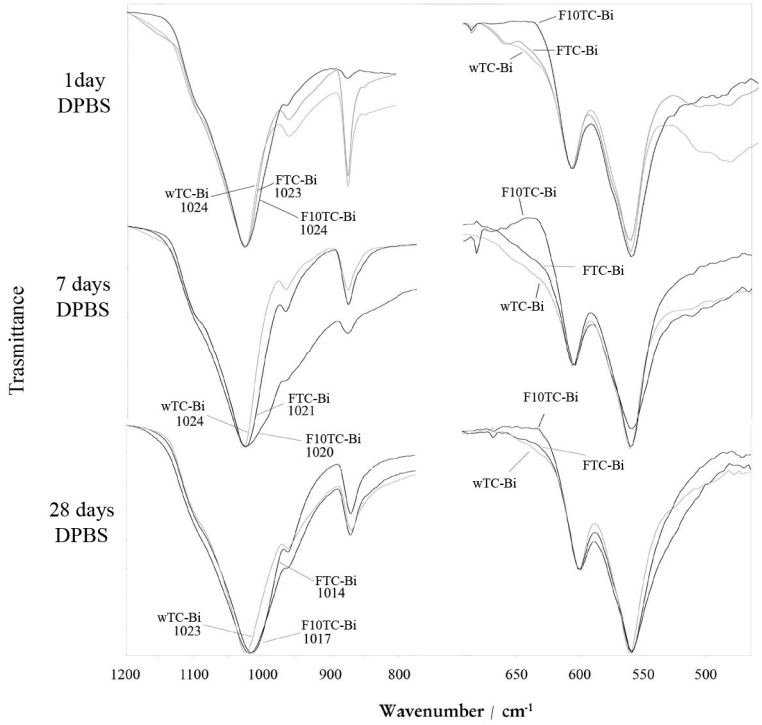

Figure 5.7: IR spectra recorded on the powders isolated from the soaking media where wTC-Bi, FTC-Bi and F10TC-Bi aged for 1 day, 7 and 28 days.

The apatite marker bands at about 1020 and 600-560 cm^{-1} appeared broader for F10TC-Bi than for FTC-Bi, in agreement with the previous results. Moreover, the spectra displayed in Figure 5.7 also showed a different trend for the different cements in the range near 630 cm^{-1}, where the OH bending mode falls. At all the ageing times, the prominent feature observed for the undoped cement (wTC-Bi) progressively weakened going to FTC-Bi and F10TC-Bi.

Spectra of the aged samples: inner fractured section

Figure 5.8 shows the IR spectra recorded in the inner fractured section of FTC-Bi and F10TC-Bi after ageing in DPBS for 5 hours, 1 day and 28 days.

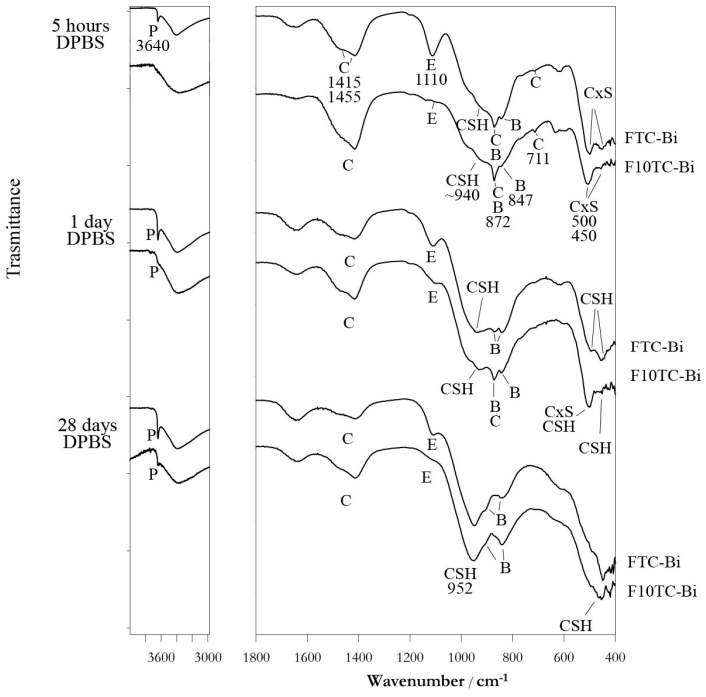

Figure 5.8: IR spectra recorded in the inner fractured section of FTC-Bi and F10TC-Bi after ageing in DPBS for 5 hours, 1 day and 28 days. The bands prevalently due to

portlandite (P), calcite (C), ettringite (E), belite (B), hydrated silicate gel (CSH) and fewly polymerized silicate tetrahedra (CxS) are indicated.

After 5 hours the marker bands of belite at (872 and 847 cm^{-1}) and calcite (1455, 1415 cm^{-1} and 870 cm^{-1}) were detected in the spectra of both cements. The shoulder at about 940 cm^{-1} indicated the formation of the CSH phase, while fewly polymerized silicates (CxS) were still present (band at 500 cm^{-1}).

The marker band of ettringite (1110 cm^{-1}) observed after 5 hours, showed a progressive decrease at longer ageing times (1 and 28 days) both in FTC-Bi and F10TC-Bi: at every ageing time, this band was more prominent in the former cement.

As observed for commercial MTAs (Figure 3.12) and for the undoped wTC-Bi cement (Figure 4.7), upon ageing (1 and 28 days), the increase in intensity of the band at 500 cm^{-1} with respect to the band at 450 cm^{-1} as well as the shift to higher frequencies of the main CSH band (from 943 to 950 cm^{-1}) and its strengthening with respect to the belite components, indicated the progress of the hydration process and the formation of the CSH phase.

The marker band of portlandite (3640 cm^{-1}) was always observed with a significantly lower intensity in the F10TC-Bi cement.

The Raman spectra recorded recorded in the inner fractured section of FTC-Bi and F10TC-Bi after ageing in DPBS (spectra not shown) confirmed the formation of ettringite as hydration product. The portlandite was not observed since its marker band at 360 cm^{-1} was undetectable due to the overlapping of the strong bismuth oxide bands.

pH measurements of the ageing media

The pH values of the DPBS solutions at different ageing time for FTC-Bi and F10TC-Bi are reported in Table 5.1. The ageing of both cements determined a marked increase of pH (over 12) since early soaking time up to 14 days. After 28 days of soaking the DPBS the solutions of both cements exhibited a decrease of the pH that still remained alkaline (about 9).

	5 hours	**1 day**	**7 days**	**14 days**	**28 days**
FTC-Bi	11.8	12.9	12.1	12.2	8.7
F10TC-Bi	12.1	13.0	12.1	12.0	9.0

Table 5.1: pH of DPBS after immersion of FTC-Bi and F10TC-Bi for 1, 7, 14, and 28 days

5.4 Discussion

In the previous chapter the bioactivity of the experimental wTC-Bi cement was demonstrated: When exposed to a simulated body fluid solution it may promote the precipitation of a 'bone-like' apatite layer on the external surface and this capability was not negatively affected by the presence of bismuth oxide.

Calcium silicate MTA cements for endodontic surgery are used directly in contact with bone, therefore, osteoconductive activity is an essential property to support an adequate biological response and new bone tissue formation.

It is well known that sodium fluoride exhibits good biological activity on osteoblast cells and dental pulp cells [1-3]. The introduction of NaF in the formulation of MTA cements improves their biological behaviour [6]. Fluorapatite is more active on osteoblast activity and bone formation than hydroxyapatite [7]: several materials such as fluoride-containing tricalcium silicates [8-9] or bioactive glasses [10-11] doped with fluorine have been studied for their ability to form fluorapatite.

Raman and IR spectroscopies have been used to investigate the effect of the doping agent on the *in vitro* bioactivity of two experimental MTA cements (FTC-Bi and F10TC-Bi) obtained by adding respectively 1% and 10% w/w of NaF to the wTC-Bi cement introduced in chapter 4.

As shown by the Raman spectra recorded on the surface of the samples aged in DPBS (Figures 4.4, 5.3 and 5.4), FTC and F10TC had a more pronounced apatite forming ability than wTC-Bi. All the cements showed the formation of an apatite deposit since 5 hours of immersion in DPBS; at longer ageing times (i.e. since 1 day) the thickness of the layer decreased along the series. FTC-Bi > F10TC-Bi > wTC-Bi.

The lower bioactivity of wTC-Bi after 1 day of soaking was confirmed by IR spectroscopy: as shown in Figures 4.6, 5.5 and 5.6, the bands of the underlying cement were appreciably observed only for wTC-Bi.

A different mechanism of the hydration process can be supposed for the FTC-Bi cement, if compared to F10TC-Bi. At every ageing time, the former produced a higher portlandite amount than the latter, as revealed by the IR spectra recorded in the inner fractured section (Figure 5.8), even if the pH of the medium did not differ significantly between the two cements (Table 5.1). Moreover, a higher and faster production of ettringite was observed

since the early phases of the hydration process (see Figure 5.8). On the basis of these data, an effect of the doping agent on the setting process cannot be excluded.

With regards to the chemical composition of the deposits, both techniques showed that for all the cements, the apatite lattice contained B-type carbonate as revealed by the marker bands of B-type carbonated apatites at about 1070 cm^{-1} (Raman), 1450–1410 and 870 cm^{-1} (IR). The presence of HPO_4^{2-} ions in the apatite lattice, as revealed by the Raman marker bands at 1000 cm^{-1}, was detected for both cements at short ageing. The broadening of the phosphate bands observed for F10TC-Bi in both the Raman and IR spectra suggested that on this cement, the apatite deposit was less crystalline than on the FTC-Bi.

Several differences in the fluoridation degree of the apatite formed on F-doped cements can be deduced by the comparison of the IR spectra recorded on the powders isolated from the DPBS medium after ageing (Figure 5.7).

The fluoridation mechanism involves a hydroxyl substitution and a subsequent adjacent hydroxyl rearrangement. As a consequence, the intensity of the OH bending mode at about 630 cm^{-1} has been reported to decrease as the extent of fluoridation increases [12]. At all ageing times, the spectral feature at about 630 cm^{-1} appeared with decreasing intensity along the series wTC-Bi > FTC-Bi > F10TC-Bi.

On the basis of this finding it can be affirmed that the cements under study formed different apatite phases upon ageing in DPBS: a hydroxy-carbonated apatite formed on the surface of wTC-Bi, while since 1 day of ageing, the apatite phase on FTC-Bi and F10TC-Bi contained increasing amounts of fluoride ions in the lattice.

The higher bioactivity of the F-doped cements in DPBS can be explained by the lower solubility of the F-substituted apatites: the incorporation of fluoride ions into the lattice

leads to a decrease of the apatite solubility: K_{sp} for fluorapatite and hydroxyapatite are $6.5 \cdot 10^{-65}$ and $7.36 \cdot 10^{-60}$, respectively.

The tests performed allow to conclude that the increase in the fluoride content up to 10%wt did not lead to an improvement in the apatite forming ability. An analogous resultwas obtained in a previous study [9]; Lin et al. have reported that among the tricalcium silicate samples doped with 1, 2 and 3 wt% of CaF_2, the specimen with the intermediate fluoride content (i.e. 2% wt) had the highest bioactivity.

On the other hand, one the disadvantages of using CaF_2 as calcium silicate cement F-doping agent was found to be the decrease of the alkalinizing activity [9].

The pH values of the DPBS medium (Table 5.1) demonstrated that NaF did not significantly reduce the alkalinity of FTC-Bi and F10TC-Bi with respect to the undoped wTC-Bi, up to 14 days at least.

Cell culture studies carried out at the Laboratory for Physiopathology of Orthopaedic Implants (Istituto Ortopedico Rizzoli, Bologna) showed that these cements had an adequate biocompatibility (comparable to commercial cements) and were able to support cell attachment, growth, and cell-surface interactions [31]

5.5 Conclusions

Experimental fluoride-doped calcium silicate cements are able to form fluorapatite in phosphate-containing solutions. The doped-cements FTC-Bi and F10TC-Bi appeared more bioactive than the undoped wTC-Bi cement. The improved bioactivity can be attributed to the formation of F-substituted apatites, characterized by a lower K_{sp} than hydroxy-carbonate apatite.

5.6 References

1. K.H.W. Lau, D.J. Baylink. *J. Bone. Min. Res* . 1998, **13,** 1660.
2. O. Nakade, H. Koyama, J. Arai, H. Ariji, J. Takada, T. Kaku. *Arch. Oral Biol.* 1999, **44,** 89.
3. D. Abdullah, T.R. Ford, S. Papaioannou, J. Nicholson, F. McDonald. *Biomaterials* 2002, **23,** 4001.
4. M.G. Gandolfi, F. Iacono, K. Agee et al. *Oral Surg. Oral Med. Oral Path. Oral Rad. Endod.* 2009, **108,** e39.
5. M.G. Gandolfi, C. Prati. *Int. Endod. J.* 2010, **43,** 889.
6. M.G. Gandolfi, F. Perut, G. Ciapetti, R. Mongiorgi, C. Prati. *J. Endod*. 2008, **34,** 39.
7. H. Qu, M. Wei. *Acta Biom.* 2006, **2,** 113.
8. Z. Xu, Q. Lin, Y. Li, X. lan, C. Lu. *Adv. Mat. Res*. 2008, **47-50,** 1339.
9. Q. Lin, Y. Li, X. Lan, C. Lu, Y. Chen, Z. Xu *J. Biom. Mat. Res.* 2009, **4,** 1.
10. D.S.Brauer, N. Karpukhina, D. Seah, R.V. Law, R.G. Hill. *Adv. Mat. Res.* 2008, **39-40,** 299.
11. D.S. Brauer, M. Mneimne, E. Lynch, D.G. Gillam, R.G. Hill. *J. Dent. Res.* 2010, **89A,** 3758.
12. C.H. Amberg, H.C. Luk, K.P. Wagstaff. *Can. J. Chem.* 1974, **52,** 4001.
13. M.G. Gandolfi, E. Modena, P. Taddei, A. Tinti, F. Perut, G. Ciapetti, P.L. Rossi, C. Prati. Proceedings of 12 Meeting- Seminar on " Ceramics, Cells and Tissues", Faenza , May 19-22. 2009, 321.

CHAPTER 6 - COMPOSITE LIGHT CURABLE POLYMER/CALCIUM SILICATE CEMENTS

6.1 - Introduction

As stated in the previous chapters, one of the main clinical limitations of MTA is the long setting time and the consequent risk for a fast dissolution and removal of the cement [1] from the surgical site of root-end obturation due to the blood and fluid contamination at the apical region of root canal.

In chapter 4, the strategy of adding calcium chloride to overcome this problem has been described. The incorporation of light-curable resins as setting accelerators has been proposed for many materials, such as the resin-modified glass-ionomer cements, also to improve their mechanical properties. As previously stressed, the reduction of setting time may extend the clinical use of MTA-based materials and make their application advisable in extremely wet and blood-contaminated surgical sites.

Figure 6.1 shows the chemical structure of two monomers widely used in biomedical applications, i.e. HEMA (2-hydroxyethyl methacrylate) and TEGDMA (triethyleneglycol dimethacrylate).

HEMA is a hydrophilic mono-vinyl monomer; its polymer, poly-HEMA, is a hydrogel that can imbibe large amounts of water (from 10 to 600%) by swelling without dissolving, due to the hydrophilic pendant groups of the molecule (Figure 6.1); it has been extensively tested for bioactivity [2-5] and biocompatibility [6].

TEGDMA is a hydrophobic monomer and its introduction into the resin formulation allows the formation of covalent cross-links upon curing, forming tight networks and solid structures [7].

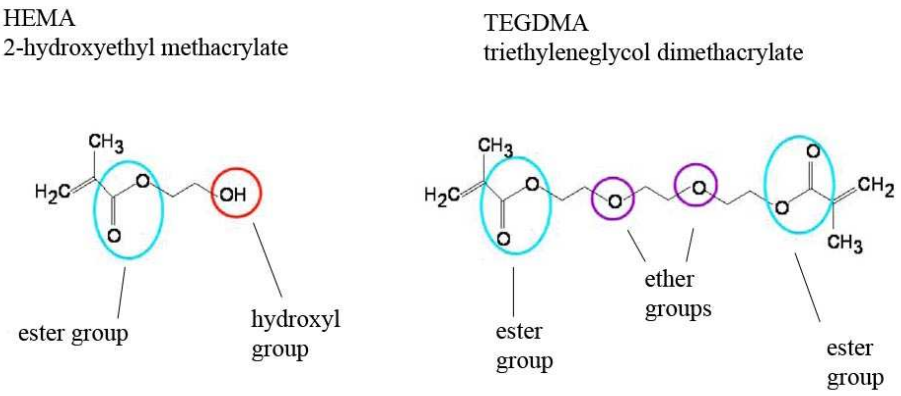

Figure 6.1: Chemical structure of HEMA and TEGDMA monomers: hydrophilic groups are labelled.

The integration of an MTA cement with a polymeric matrix allows to obtain a material with more adequate characteristics and properties for applications in wet apical cavities contaminated by blood during the preparation of a bone window, as it occurs during root-end surgery procedures and root repair procedures.

In this chapter, an experimental light-curable calcium silicate MTA cement is characterized. The experimental wTC formulation (chapter 4) was added with barium sulphate for radiopacity and an anphiphilic light-curable resin composed of a mixture of HEMA and TEGDMA. The effect of the resin as well as barium sulphate on the bioactivity of wTC was investigated.

6.2 - Materials and Methods

Cement preparation

As for the other experimental dental materials studied in this thesis, the cements were prepared at the Laboratory of Biomaterials, Department of Odontostomatological Science, University of Bologna.

The light-curable resin-modified calcium silicate cement (lc-MTA) was prepared by mixing a calcium silicate cement powder (wTC-Ba) and an anphiphilic light-curable resin liquid phase (Gandolfi MG & Prati C, patent of the University of Bologna).

The wTC-Ba powder was constituted by the wTC formulation described in chapter 4 added with $BaSO_4$ for radiopacity. The liquid phase contained 2-hydroxyethyl methacrylate (HEMA), triethyleneglycol dimethacrylate (TEGDMA), camphorquinone (CQ) and ethyl-4-(dimethylamino)-benzoate (EDMAB).

To obtain the wTC-Ba cement, the wTC-Ba powder was mixed with DPBS for 30 s in a powder/liquid ratio of 3:1.

To obtain the lc-MTA cement, the wTC-Ba powder was mixed with the liquid phase for 30 s in a powder/liquid ratio of 4:1 and light-cured for 120 s with a halogen lamp (T-LED elca, Anthos Cefla, Imola, Italy).

Once mixed, all cements were compacted to the excess into PVC moulds (8 mm in diameter and 1.6 mm thick). The obtained cylindrical specimens (0.3 g of weight) exposed an exchange surface of 90.4 mm^2 (upper surface 50.2 mm^2 and lateral surface 40.2 mm^2).

The cylindrical specimens were soaked in 5 mL of DPBS (DPBS/cement ratio 17 mL/g) at 37 °C for 1 day, 7, 14, and 28 days.

Another set of samples were soaked in Dulbecco's Modified Eagle's Medium (DMEM, Sigma-Aldrich Corp., St. Louis, MO, USA) supplemented with 10% of foetal bovine serum (FBS, Sigma-Aldrich Corp., St. Louis, MO, USA) for the same prefixed times.

The storage media were renewed every week. At the endpoints, the medium was removed and its pH was measured using a glass electrode.

Micro-Raman, ATR/FT-IR and pH measurements were carried out under the same experimental conditions described in chapter 4.

To evaluate the possible bioactivity of poly-HEMA, poly-TEGDMA and poly(HEMA-co-TEGDMA) polymers [8], additional resin samples composed of pure poly-HEMA or pure poly-TEGDMA or pure poly(HEMA-co-TEGDMA) were prepared by light-curing under the same experimental conditions used for lc-MTA. The specimens were soaked for 4 weeks in a metastable calcifying medium at pH 7.3 containing Ca^{2+} and PO_4^{3-} ions in a Ca/P ratio of 1.67, according to Chirila et al. [9] and analyzed by ATR/FT-IR.

6.3 Results

Unaged wTC-Ba and lc-MTA cements

The composition of the unhydrated cements was analyzed by micro-Raman and IR spectroscopy.

Figures 6.2 and 6.3 show the micro-Raman and IR spectra, respectively, recorded on the light cured poly(HEMA-co-TEGDMA) resin, the unhydrated wTC-Ba cement and the light cured lc-MTA composite.

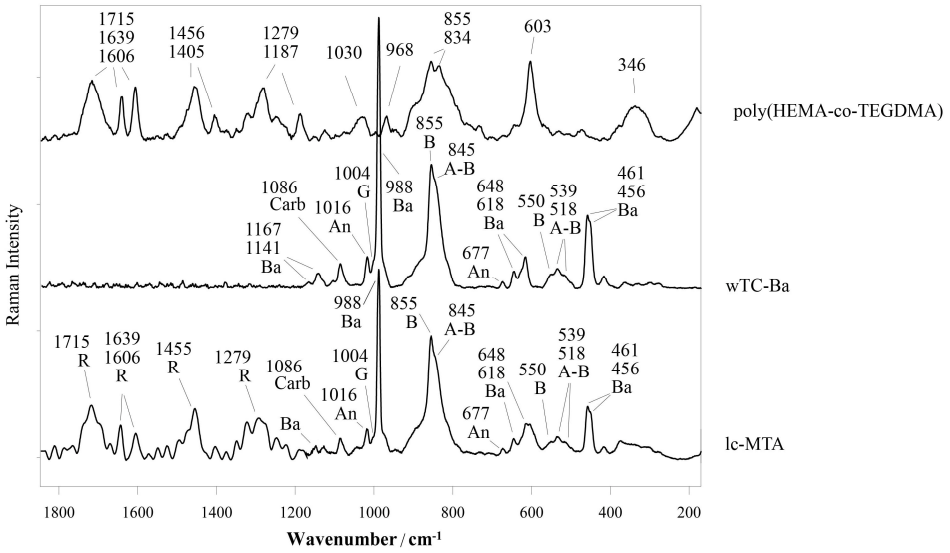

Figure 6.2: Micro-Raman spectra of the light cured poly(HEMA-co-TEGDMA) resin, the unhydrated wTC-Ba cement and the light cured composite (lc-MTA). The bands prevalently due to barium sulphate (Ba), calcium carbonate (Carb), anhydrite (An), gypsum (G), belite (B), alite (A), poly(HEMA-co-TEGDMA) resin (R) are indicated.

The Raman spectrum of unhydrated wTC-Ba (Figure 6.2) as that of wTC (Figure 4.1) showed the presence of alite (bands at 845, 539 and 518 cm^{-1}), belite (bands at 855, 845, 550, 539 and 518 cm^{-1}), gypsum (shoulder at 1004 cm^{-1}), anhydrite (bands 1016 and 677 cm^{-1}) and calcium carbonate (band at 1085 cm^{-1}).

The strongest band observed at 988 cm^{-1} (ν_1 SO_4) was due to the barium sulphate component, added for radiopacity. Other bands attributable to this phase were detected at 1167-1141 cm^{-1} (ν_3 SO_4), 648-618 cm^{-1} (ν_4 SO_4) and 461-456 cm^{-1} (ν_2 SO_4) [10**]**.

The composition of the wTC-Ba cement was confirmed by the IR spectrum (Figure 6.3). According to the Raman results, the bands due to barium sulphate at 1183, 1126, 1082 cm^{-1} (ν_3 SO_4^{2-}), 980 cm^{-1} (ν_1 SO_4^{2-}), 635 and 610 cm^{-1} (ν_4 SO_4^{2-}) [11] were observed, while the component at 677 cm^{-1} was characteristic of gypsum and anhydrite.

The bands at 1420 and 1465 cm^{-1} confirmed the presence of calcium carbonate [12-13].

As for wTC (Figure 4.2), the band at 930 cm^{-1} was attributed to alite and the components at 874 and 847 cm^{-1} were assigned to belite.

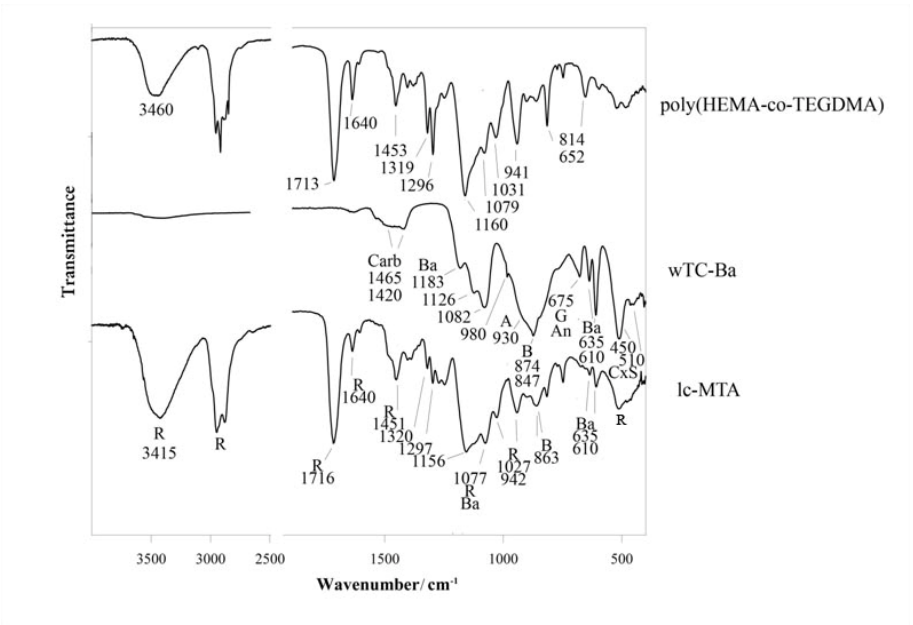

Figure 6.3: IR spectra of the light cured poly(HEMA-co-TEGDMA) resin, the unhydrated wTC-Ba cement and the light cured composite (lc-MTA). The bands prevalently due to barium sulphate (Ba), calcium carbonate (Carb), anhydrite (An), gypsum (G), belite (B), alite (A), fewly polymerized silicates (CxS), poly(HEMA-co-TEGDMA) resin (R) are indicated.

The Raman spectrum of the composite material was highly dominated by the bands of the unhydrated wTC-Ba powder in the region below 1200 cm^{-1} where no spectral features of the resin were detected. The presence of the poly(HEMA-co-TEGDMA) resin was

observed only at higher wavenumbers (components at 1715, 1639, 1606, 1455, and 1279 cm^{-1}): no bands of the inorganic component were observed in this spectral range.

On the other hand, the IR spectrum was highly dominated by the resin components. Some bands of the mineral component due to barium sulphate (at about 1080, 635 and 610 cm^{-1}) and belite (at 863 cm^{-1}) were detected.

IR spectroscopy allows to investigate the possible interactions between the calcium silicate cement component and the poly(HEMA-co-TEGDMA) resin (Figure 6.3).

The band assigned to belite showed a downshift from 874 to 863 cm^{-1} going from wTC-Ba to the composite; moreover, the maximum of the broad band due to the OH stretching vibration of HEMA appeared shifted from 3460 to 3415 cm^{-1} going from poly(HEMA-co-TEGDMA) to the composite. These trends suggested the occurrence of hydrogen bonding interactions between silicate ions and OH groups of HEMA.

In the composite, the C=O stretching band was detected shifted and broadened with respect to the copolymer (at 1716 cm^{-1} in the former, 1713 cm^{-1} in the latter) suggesting a change in the hydrogen bonding arrangement and distribution.

Moreover, in the composite, the band at 1640cm^{-1}, due to the vibration of the C=C group of the HEMA and TEGDMA monomers, was significantly weaker than in the resin suggesting that lc-MTA was characterized by a higher polymerization degree of the resin than pure poly(HEMA-co-TEGDMA).

Study of bioactivity: spectra recorded on the surface of the aged samples

Figures 6.4 and 6.5 show the micro-Raman spectra recorded on the surface of the wTC-Ba cement and the composite after ageing in DPBS for 1 day, 7, 14 and 28 days.

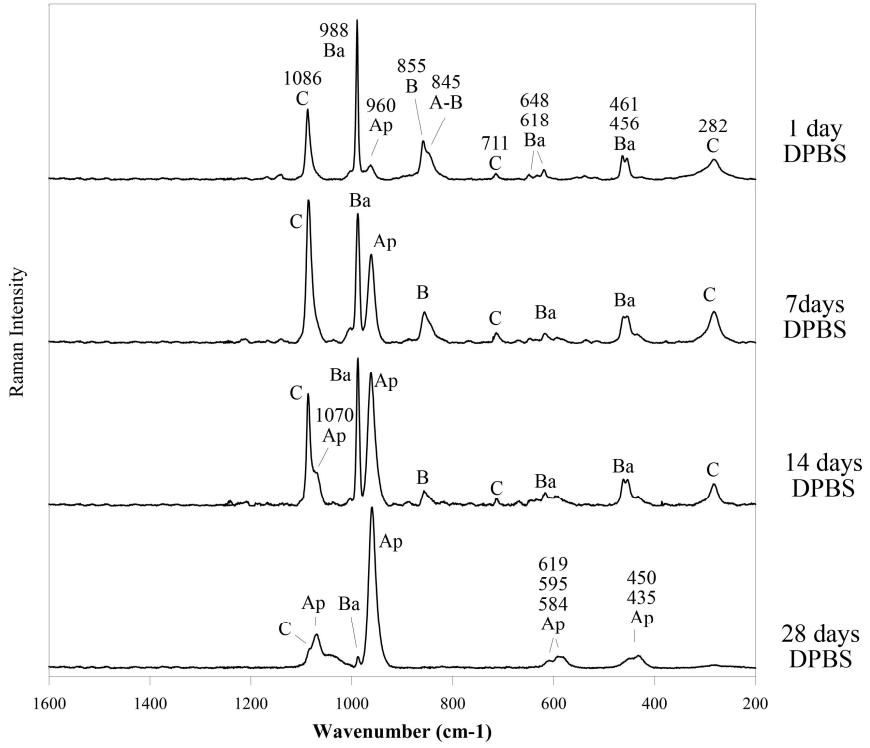

Figure 6.4: Micro-Raman spectra recorded on the surface of wTC-Ba after 1 day, 7, 14 and 28 days of soaking in DPBS. The bands due to belite (B), alite (A), anhydrite (An), gypsum (G), barium sulphate (Ba), calcite (C), apatite (Ap) are indicated .

The marker band of apatite at about 960 cm^{-1} was observed in the spectra of lc-MTA and wTC-Ba cements already after one day of aging in DPBS, with different relative intensities. The presence of the component at 1070 cm^{-1} in the spectrum recorded on the surface of lc-MTA suggested the formation of a B-type carbonated apatite: the weaker bands due to the cement components and calcite were also detected; the lc-MTA cement appeared to form the thickest deposit, as revealed by the highest intensity ratio between the bands of apatite and belite (at about 960 and 855 cm^{-1}, respectively).

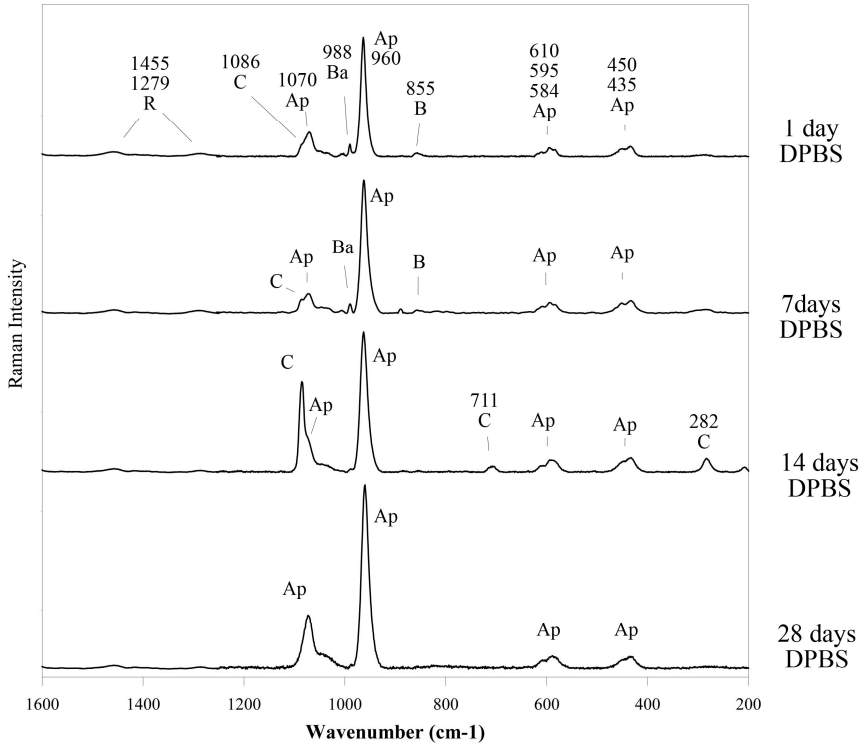

Figure 6.5: Micro-Raman spectra recorded on the surface of lc-MTA after 1 day, 7, 14 and 28 days of soaking in DPBS. The bands due to belite (B), barium sulphate (Ba), calcite (C), apatite (Ap) and poly(HEMA-co-TEGDMA) resin (R) are indicated .

At increasing ageing times, the deposit became progressively thicker on both the cements: the bands of the underneath cement progressively weakened, while the component at 1070 cm^{-1} (B-type carbonated apatite) progressively appeared also on the wTC-Ba cement (14 days): the phosphate bending modes at 610, 590, 584, 450 and 435 cm^{-1} were detected already after 1 day of ageing for lc-MTA and only after 28 days for wTC-Ba, confirming a thicker deposit on the composite. The bands of poly(HEMA-co-TEGDMA) resin were only slightly detectable over 1200 cm^{-1} after 1 day of ageing.

The $Ca(OH)_2$ band at 360 cm^{-1} was never detected on the surface of the cements, due to its release into the storage medium, which leads to a pH increase (see below), in agreement with the results reported in the previous chapters.

Figures 6.6 and 6.7 show the IR spectra recorded on the surface of wTC-Ba and lc-MTA cements, respectively, after 1 day, 7, 14 and 28 days of soaking in DPBS.

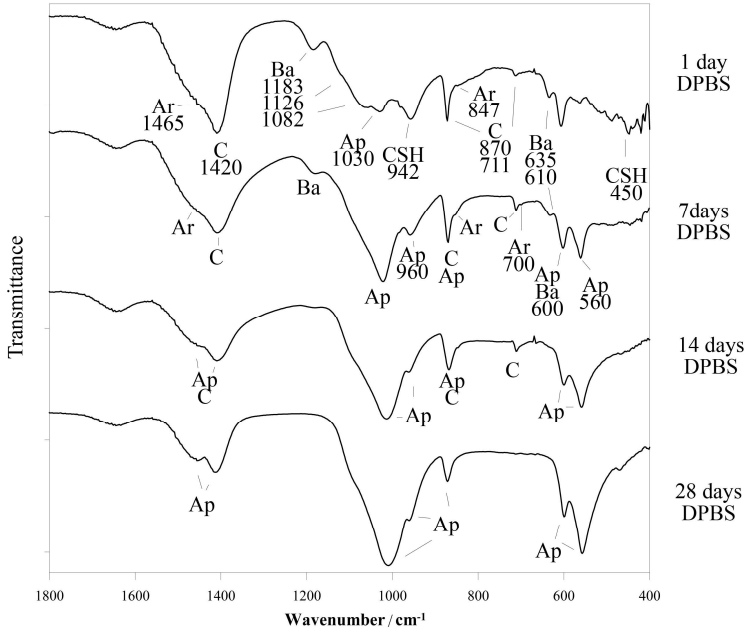

Figure 6.6: IR spectra recorded on the surface of wTC-Ba after 1 day, 7, 14 and 28 days of soaking in DPBS. The bands due to hydrated silicate gel (CSH), barium sulphate (Ba), calcite (C), aragonite (Ar) and apatite (Ap) are indicated .

After 1 day of ageing in DPBS, the IR spectra of lc-MTA showed the presence of B-type carbonated apatite deposit, as revealed by the marker bands at 1465, 1420, 1025, 960, 870, 600 and 560 cm^{-1}. The evidence of an apatitic layer on wT-Ba was given by the marker band at 1030 cm^{-1}. The band at 711 cm^{-1} indicated the formation of a few amount of calcite; on wTC-Ba calcium carbonate was present also as aragonite (marker band at 847 cm^{-1}). No bands of the underlying cement were detected on lc-MTA, suggesting a deposit

thicker than 2 μm: on wTC-Ba, the apatite deposit appeared thinner than on lc-MTA, as revealed by the lower intensity of the apatite bands, and the detection of prominent features due to the CSH silicate phase (942 cm^{-1}) and barium sulphate (1183, 635 and 610 cm^{-1}). The bands of the underlying cement were still observed after 7 days of ageing and became undetectable only at 14 days.

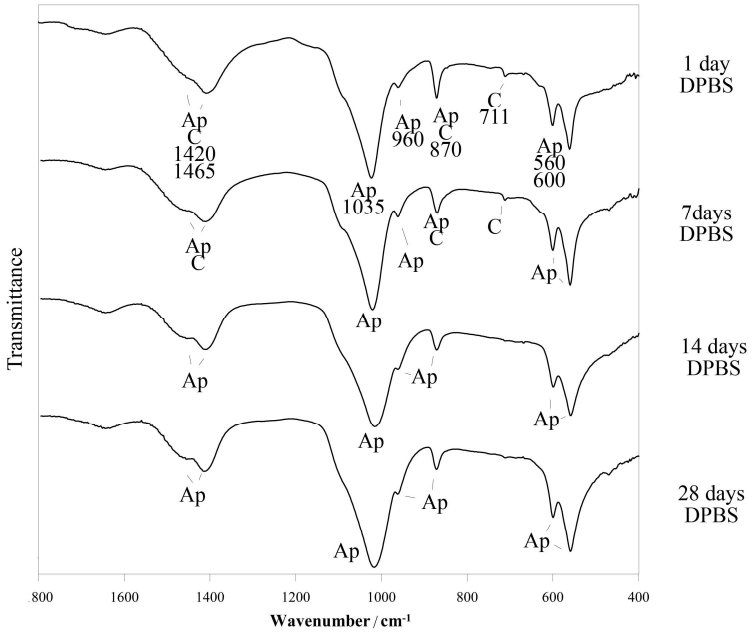

Figure 6.7: IR spectra recorded on the surface of lc-MTA after 1 day, 7, 14 and 28 days of soaking in DPBS. The bands due to calcite (C) and apatite (Ap) are indicated .

Figures 6.8 and 6.9 show the IR spectra recorded on the surface of wTC-Ba and lc-MTA cements, respectively, after 1 day, 7, 14 and 28 days of soaking in DMEM. The Raman spectra were not recorded because of the high fluorescence of the medium.

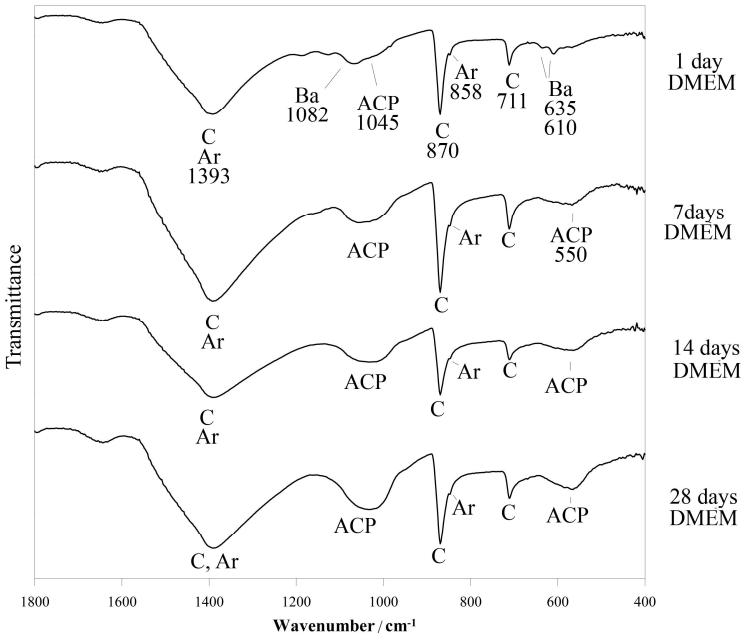

Figure 6.8: IR spectra recorded on the surface of wTC-Ba after 1 day, 7, 14 and 28 days of soaking in DMEM. The bands due to barium sulphate (Ba), calcite (C), aragonite (Ar), amorphous calcium phosphate (ACP) are indicated .

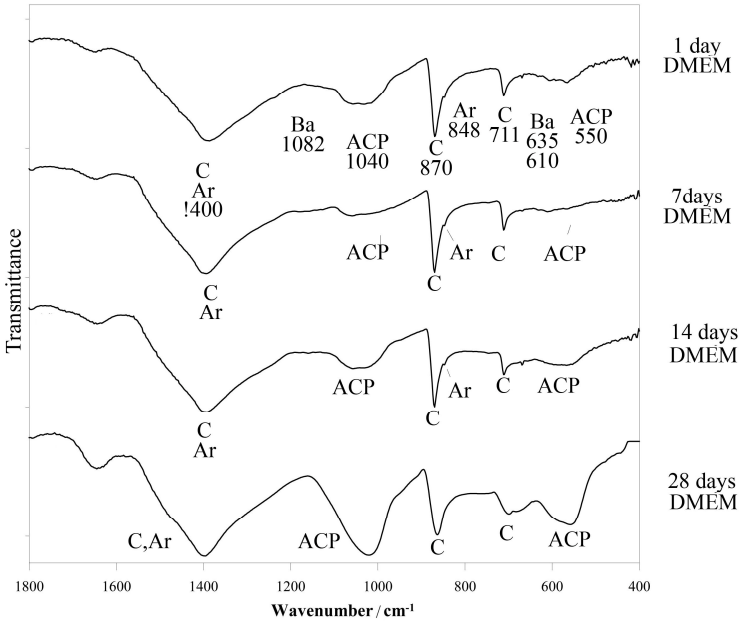

Figure 6.9: IR spectra recorded on the surface of lc-MTA after 1 day, 7, 14 and 28 days of soaking in DMEM. The bands due to barium sulphate (Ba), calcite (C), aragonite (Ar), amorphous calcium phosphate (ACP) are indicated.

Upon ageing in DMEM, wTC-Ba and lc-MTA formed a coating of amorphous calcium phosphate (broad bands at about 1050 and 550 cm^{-1}) and calcium carbonate (as both calcite and aragonite), which progressively thickened at increasing ageing time, as revealed by the progressive disappearance of the underlying cement bands due to barium sulphate (at 635 and 610 cm^{-1}) that became undetectable since 7 days.

Spectra of the aged samples: inner fractured section.

Figures 6.10 and 6.11 show the micro-Raman spectra recorded in the inner fractured section of wTC-Ba and lc-MTA, respectively, after 1 day, 14 and 28 days of ageing in DPBS.

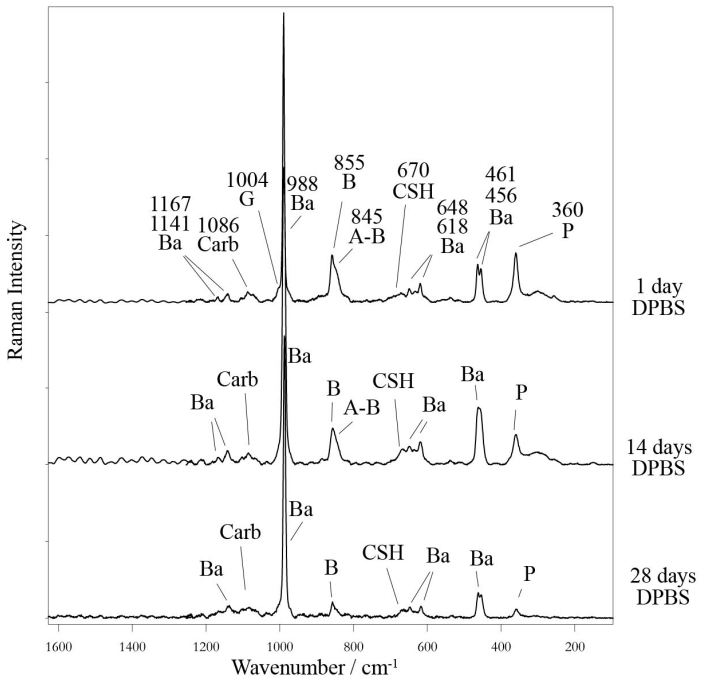

Figure 6.10: Micro-Raman spectra recorded in the inner fractured section of wTC-Ba after 1 day, 14 and 28 days of soaking in DPBS. The bands prevalently due to barium sulphate (Ba), calcium carbonate (Carb), gypsum (G), belite (B), alite (A), hydrated silicate gel (CSH) and portlandite (P) are indicated.

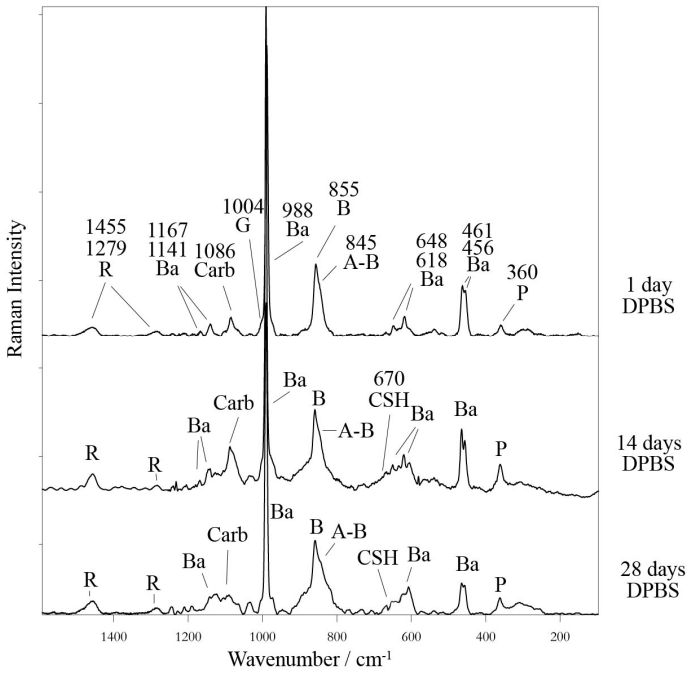

Figure 6.11: Micro-Raman spectra recorded in the inner fractured section of lc-MTA cement after 1 day, 14 and 28 days of soaking in DPBS. The bands prevalently due to barium sulphate (Ba), calcium carbonate (Carb), gypsum (G), belite (B), alite (A), poly(HEMA-co-TEGDMA) resin (R), hydrated silicate gel (CSH) and portlandite (P) are indicated.

After 1 day of ageing, in the spectra of both cements, the bands of anhydrite at 1016 and 677 cm^{-1} disappeared, according to the high hydration rate of this component. Ettringite (characterized by a Raman band at 990 cm^{-1}) was undetectable due to the overlapping of the barium sulphate band. The decrease of the relative intensity of the alite shoulder at 845 cm^{-1} with respect to the main belite band at 855 cm^{-1} confirmed the slower hydration of the latter.

The marker band of portlandite at 360 cm^{-1} and the the weak broadening near 670 cm^{-1} attributable to hydrated silicates phase [14-16] were detected in both the cements, confirming the formations of the typical hydration products of the cements. The portlandite

band was never detected on the surface of the cements, due to its release into the storage medium which increased its pH (see below).

In lc-MTA, the resin bands at about 1455 and 1279 cm^{-1} were always observed.

Figure 6.12 shows the IR spectra recorded in the inner fractured section of wTC-Ba and lc-MTA after 1 day and 28 days of soaking in DPBS and DMEM.

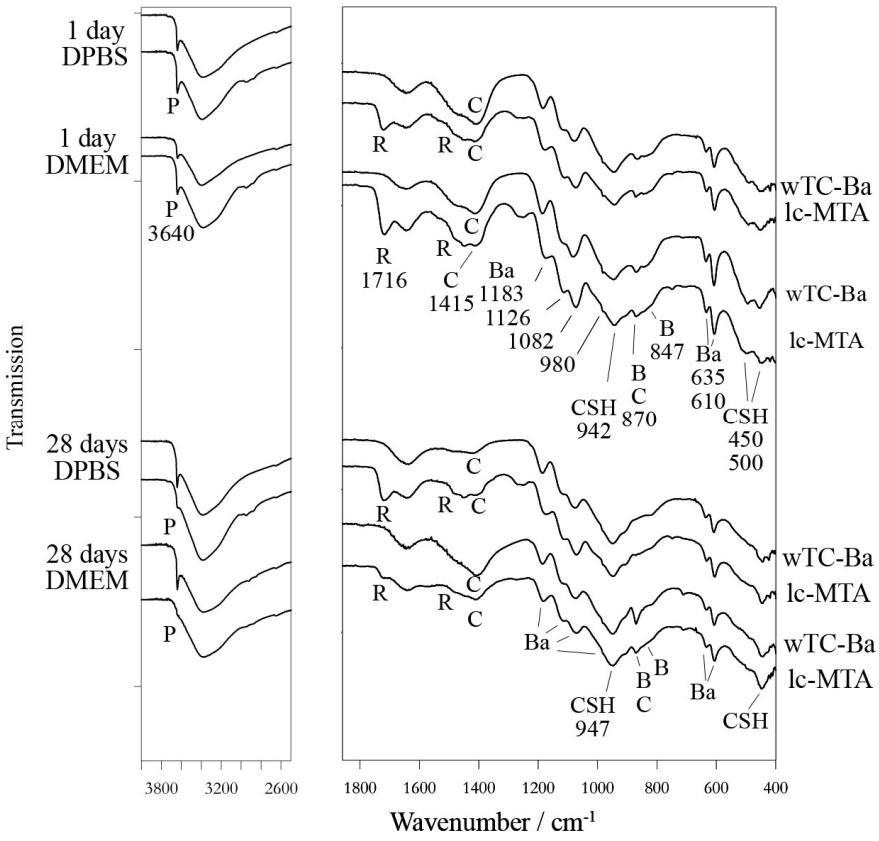

Figure 6.12: IR spectra recorded in the inner fractured side of wTC-Ba and lc-MTA cement after 1 day and 28 days of soaking in DPBS and DMEM. The bands prevalently due to barium sulphate (Ba), calcium calcite (C), belite (B), alite (A), poly(HEMA-co-TEGDMA) resin (R) and hydrated silicate gel (CSH) are indicated.

The marker band of portlandite at 3640 cm^{-1} was detected in the spectra of both cements at every ageing time in both media, as well as the bands of calcite (1415 cm^{-1} and

occasionally 870 cm^{-1}). Ettringite was undetectable also by IR spectroscopy, due to the overlapping of the barium sulphate bands.

The already described trend of the CSH band at about 940 cm^{-1} indicated the progress of the hydration process.

For lc-MTA the bands of the poly(HEMA-co-TEGDMA) resin at about 1716 and 1451 cm^{-1} were observed up to 28 days of soaking in both media.

Bioactivity of the resin matrix

To evaluate the possible bioactivity of the pure resin, poly-HEMA, poly-TEGDMA and poly(HEMA-co-TEGDMA) polymers were soaked for 28 days in a metastable calcifying medium, according to Chirila et al. [8,9].

The resin samples were transparent before soaking and showed a superficial opacity after 4 weeks, , particularly evident for poly-HEMA.

Figures 6.13, 6.14 and 6.15 show the IR spectra recorded on the surface of the pure polymers before and after 28 days of ageing in the calcifying medium.

The bands at about 1025, 600 and 560 cm^{-1} revealed that all the samples were covered by an apatite deposit: the detection of the bands of the polymeric components indicated a layer of apatite thinner than 2 µm. Poly-HEMA also showed the band at 963 cm^{-1} suggesting a thicker deposit (Figure 6.13). On the basis of the relative intensity of the apatite bands, it can be deduced that the thickness of the deposit decreased along the series:

poly-HEMA > poly(HEMA-co-TEGDMA) > poly-TEGDMA.

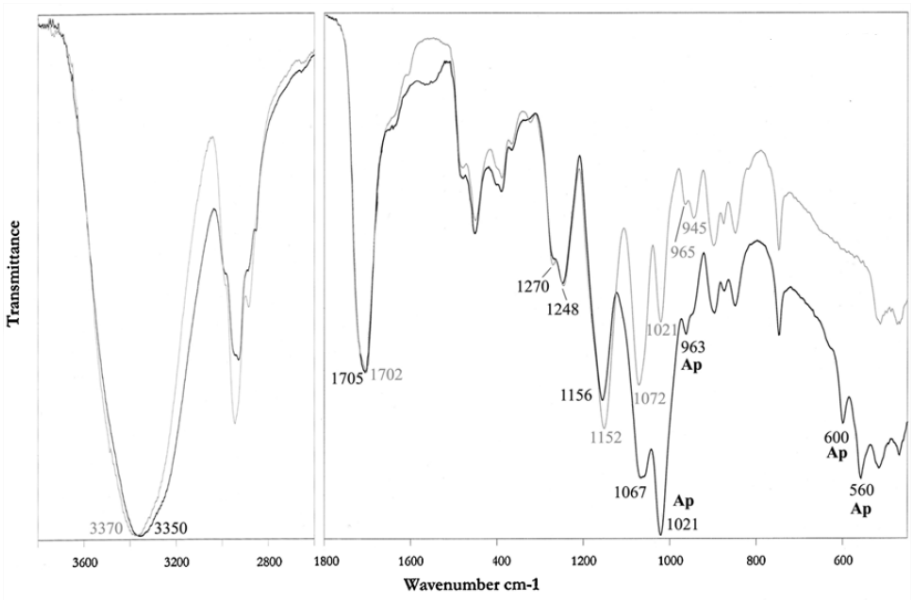

Figure 6.13: IR spectra recorded on the surface of pure poly-HEMA before (grey) and after 28 days of ageing according to Chirila et al. (black). The bands due to apatite (Ap) and oxygen-containing groups are indicated.

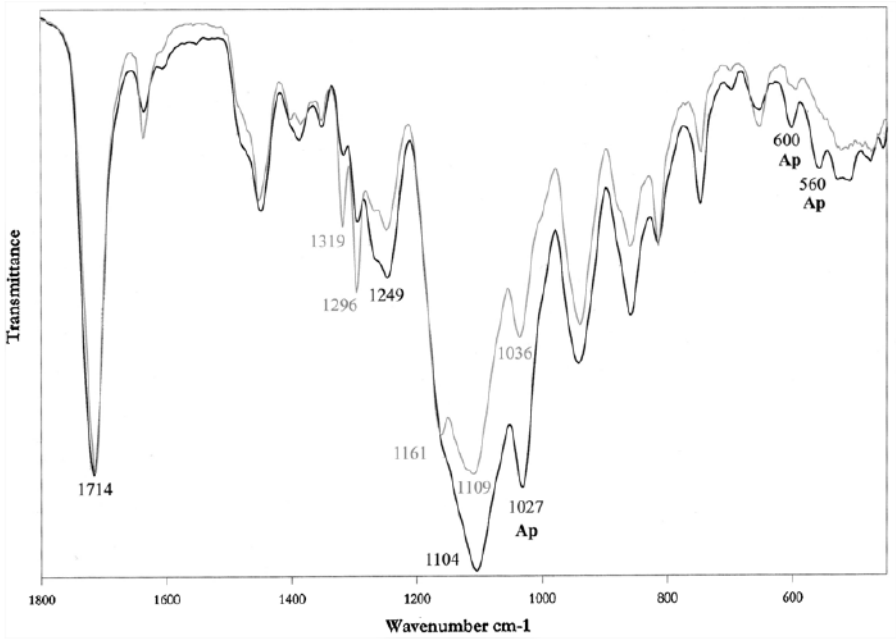

Figure 6.14: IR spectra recorded on the surface of pure poly-TEGDMA before (grey) and after 28 days of ageing according to Chirila et al. (black). The bands due to apatite (Ap) and oxygen-containing groups are indicated.

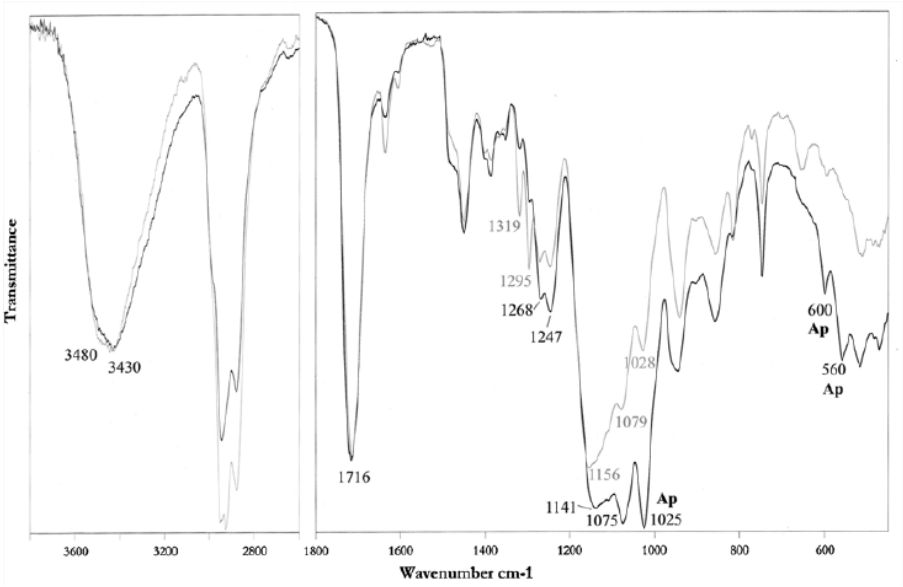

Figure 6.15: IR spectra recorded on the surface of pure poly(HEMA-co-TEGDMA) before (grey) and after 28 days of ageing according to Chirila et al. (black). The bands due to apatite (Ap) and oxygen-containing groups are indicated.

With regards to the most bioactive polymer (i.e. poly-HEMA), upon apatite deposition, some polymer bands underwent wavenumber shifts and/or intensity changes. The oxygen-containing groups appeared the most involved in the changes, as revealed by the trend of the bands at about 3350 cm^{-1} (OH stretching vibration), 1700 cm^{-1} (C=O stretching vibration), 1270–1248–1150cm^{-1} (C–O–C stretching vibrations), 1070 cm^{-1} (C–O stretching vibration). Since control and soaked samples were characterized by similar polymerization degrees (band at 1640 cm^{-1}), these spectral variations can be ascribed to the chelation of calcium ions.

Analogous considerations could be made for poly-TEGDMA and poly(HEMA-co-TEGDMA) (Figure 6.14 and 6.15), but the different polymerization degrees observed for soaked samples and controls do not allow to assign the spectral changes to calcium chelation only.

pH measurements of the ageing media

Tables 6.1 and 6.2 reported the pH values of the DPBS and DMEM solutions, respectively, at different ageing time for wTC-Ba and lc-MTA.

	1 day	**7 days**	**14 days**	**28 days**
wTC-Ba	12.3	12.2	9.9	9.1
lc-MTA	11.8	12.1	9.2	9.4

Table 6.1: pH of DPBS after immersion of wTC-Ba and lc-MTA for 1 day, 7, 14, and 28 days.

	1 day	**7 days**	**14 days**	**28 days**
wTC-Ba	9.9	9.5	9.1	9.2
lc-MTA	9.3	9.8	9.7	9.4

Table 6.2: pH of DMEM after immersion of wTC-Ba and lc-MTA for 1 day, 7, 14, and 28 days.

With regards to DPBS, both the cements showed alkaline pH (about 12) since 1 day of ageing up to 7 days. Since 14 days of soaking, the DPBS solution progressively exhibited a pH decrease up to 28 days (near 9.2).

The pH of the DMEM medium showed meanly lower values in the first 7 days.

6.4 Discussion

Blood contamination is inevitable through all clinical procedures in oral and root-end apical surgery and may increase the risk for a complete wash-out of the material during its setting phase.

The incorporation of light-curable resins to root-end materials represents an innovative approach. The reduction of setting time allows to prevent the cement wash-out, improving the clinical success. The lc-MTA cement showed both initial and final setting times of about 2 min while for wTC-Ba the initial and final setting times were 31 and 57 min, respectively [17]**.**

The effect of the addition of barium sulphate and poly(HEMA-co-TEGDMA) resin to the experimental wTC formulation was investigated by micro-Raman and IR spectroscopy.

Vibrational analysis indicated that the bioactivity of wTC in DPBS was not negatively influenced by the addition of barium sulphate (wTC-Ba): as shown by the micro-Raman spectra recorded on the surface of the soaked samples (Figure 4.3 and 6.4), the cement formed a B-type carbonated apatite deposit of increasing thickness during the ageing period. On the basis of the already used I_{960}/I_{855} Raman intensity ratio, it can be affirmed that on wTC and wTC-Ba, the apatite layer thickened at the same rate. This result was confirmed by the IR spectra (Figures 4.5 and 6.6), which on both cements indicated the presence of a deposit thicker than 2 μm after 14 days of soaking.

The incorporation of poly(HEMA-co-TEGDMA) induced an enhancement of bioactivity: on lc-MTA, the IR spectra (Figure 6.7) demonstrated the formation of a B-type carbonated apatite deposit thicker than 2 µm already after 1 day of soaking in DPBS. The trend of the Raman spectra suggested the formation of thicker apatite deposits on lc-MTA at all the ageing times (Figures 6.4 and 6.5).

Several chemical aspects influence the formation of the apatitic deposit.

The micro-Raman and IR spectra recorded in the inner fractured section of the aged samples (Figures 6.11 and 6.12) confirmed the formation of the typical hydration products of MTA cements (i.e. $Ca(OH)_2$ and the CSH phase). As discussed in the previous chapters (Figure 3.16), thanks to the alkaline pH of the solutions (Table 6.1), also in lc-MTA negatively charged $Si–O^-$ groups of CSH may represent a catalytic site for apatite nucleation.

The presence of the organic phase in lc-MTA introduces an additional interface that can be considered to explain the improved bioactivity of lc-MTA.

Bioactivity experiments showed that the most hydrophilic polymer (i.e. poly-HEMA) is also the most bioactive: on the basis of the deposit thickness revealed by IR spectra (Figures 6.13, 6.14 and 6.15), the ability to induce apatite deposition after a 4-week immersion in a metastable calcifying medium decreased along the series: poly- HEMA> poly(HEMA-co-TEGDMA) > poly-TEGDMA.

The IR spectra corresponding to poly-HEMA showed that upon apatite deposition (Figure 6.13), the bands assignable to OH, C=O, C–O–C and C–O groups underwent wavenumber shifts and intensity changes. This trend can be explained by considering that oxygen containing groups (hydroxyl and ester groups in poly-HEMA) may chelate calcium ions

present in the surrounding medium inducing apatite deposition, as proposed in Figure 6.16. This process occurs on poly-TEGDMA thanks to analogous interactions between calcium ions and oxygen atoms from ester and ether groups. Apatite deposition on poly(HEMA-co-TEGDMA) can be explained as a combination of the two mechanisms.

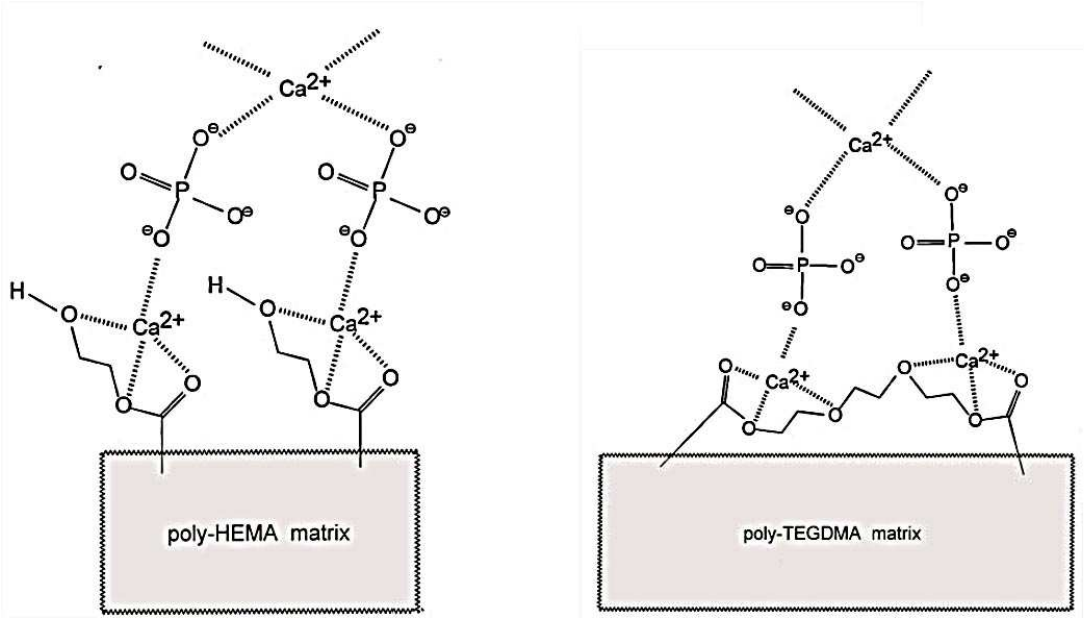

Figure 6.16: (left) Chelation of calcium ions by hydroxyl, ester and ether groups from poly-HEMA and induced nucleation of an apatite phase; (right) Chelation of calcium ions by ester and ether groups from poly-TEGDMA and induced nucleation of an apatite phase.

The bioactivity differences observed between wTC-Ba and lc-MTA upon ageing in DPBS were confirmed after ageing in DMEM, although the nature of the formed deposit was significantly different, being constituted by an amorphous calcium phosphate. As shown in Tables 6.1 and 6.2, the DMEM medium attained, in the first week of soaking, pH values lower than DPBS (i.e. <10 *versus* about 12): it can be suggested that these lower pH conditions and, above all, the presence of a lower phosphate content in the DMEM medium (0.91 *versus* 9.56 mM) retard the precipitation of a crystalline phase. Besides, as

discussed in chapter 1, the amorphous calcium phosphates are the most commonly reported precursors in the *in vivo* formation of HA.

6.5 Conclusions

The present study demonstrated that the bioactivity of the wTC cement was not affected by the addition of barium sulphate (wTC-Ba).

The experimental lc-MTA light curable cement possesses improved apatite forming ability in DPBS: after soaking in DMEM, the formation of an amorphous calcium phosphate deposit was observed on both wTC-Ba and lc-MTA confirming the potential bioactivity in a protein containing environment.

The enhanced bioactivity of lc-MTA in DPBS can be explained also in relation to the calcium-chelation ability of the poly-(HEMA-co-TEGDMA) resin that may induce the heteronucleation of apatite on the cement surface.

6.6 References

1. M.L. Porter, A. Berto, C.M. Primus, I. Watanabe. J. Endod. 2010, **36,** 524.
2. A. Costantini, G. Luciani, G. Annunziata, B. Silvestri, F. Branda. *J. Mater. Sci. Mater. Med.* 2006, **17,** 319.
3. A. Costantini, G. Luciani, B. Silvestri, F. Tescione, F. Branda. *J. Biomed. Mater. Res. Part B. Appl. Biomater.* 2008, **86B,** 98.
4. L.F. Boesel, S.C.P. Cachinho, M.H.V. Fernandes, R.L. Reis. *Acta Biomater* 2007, **3,** 175.
5. L.F. Boesel, R.L. Reis. *Prog Polym Sci* 2008, **33,** 180.

6. J.P. Montheard, M. Chatzopoulos, D. Chappard. *J. Macromol. Sci. Macromol. Rev.* 1992, **32,** 1.

7. I.M. Barszczewska-Rybarek. *Dent. Mater.* 2009, **25,** 1082.

8. T.V. Chirila, Z. Zainuddin, D.J.T. Hill, A.K. Wittaker, A. Kemp. *Acta Biomater.* 2007, **3,** 95.

9. T.V. Chirila, D.A. Morrison, Z. Gridneva, A.J. Garcia, S.T. Platten, B.J. Griffin, et al. *J. Mater. Sci. Lett.* 2005, **24,** 4987.

10. L. V. Haley, T. A. Mattioli, D. R. Wiles. *J. Raman Spectrosc.* 1987, **18,** 101.

11. H.W. Van der Marel and H Beutelspacher, Atlas of Infrared Spectroscopy of Clay Minerals and their Admixtures, Elsevier, Amsterdam, 1976.

12. F.A. Andersen, L. Brecevic, *Acta Chem. Scand.* 1991, **45,** 1018.

13. E.T. Stepkowska, J.M. Blanes, C. Real and J.L. Perez-Rodriguez, *J. Therm. Anal. Cal.* 2005, **82,** 731.

14. M. Tarrida, M. Madon, B. Le Rolland, P. Colombet, *Adv. Cem. Based Mater.* 1995, **2,** 15.

15. J. Bensted, *Cem. Concr. Res.* 1977, **7,** 161.

16. R. J. Kirkpatrick, J. L. Yarger, P. F. McMillan, P. Yu, X. Cong, *Adv. Cem.BasedMater.* 1997, **5,** 93.

17. M.G. Gandolfi, P. Taddei, F. Siboni, E. Modena, G. Ciapetti, C. Prati. *Dent Mater.* 2011, **27,** e134.

CHAPTER 7 - DENTIN REMINERALIZATION BY MTA-BASED CALCIUM SILICATE CEMENTS

7.1 Introduction

Dentin is a complex tissue, which contains apatite as mineral phase, collagen and other proteins, and water [1-2]. Initial carious lesions affect the mineral phase of dentin and expose the collagen fibers creating the conditions for a fast destruction of the entire dentin network [2].

The development of restorative materials able to induce the remineralization of demineralized/carious dentin is an important requirement for operative and preventive dentistry. At present no restorative materials with proven capability to induce dentin remineralization are available on the market.

The remineralization of demineralized dentin (*bioremineralization*) is the process of restoring its mineral phase through the formation of inorganic mineral-like materials [3].

Recently, experimental remineralizing resin-based calcium phosphate cements (ion-leaching composites) have been proposed as restorative materials to induce dentin remineralization [4-6].

Biomimetic remineralization of dentin has been investigated by different methods using ion-containing solutions or ion-leaching silicon-containing materials: solutions containing Ca^{2+}, SiO_4^{4-}, F^- or PO_4^{3-} ions [7], bioactive glasses placed on dentin [8**]**, remineralization solutions supplemented with a bioactive glass **[9]** and remineralizing solutions containing the ions leached from ultrafine bioactive glass particles [10**]**, glass-ionomer cements containing a bioactive glass in dog restorations [11], MTA cement layered on the dentin surface [12], Portland cement blocks immersed in a biomimetic analogue consisting of simulated body fluid added with polyacrylic acid acid [13].

In most of these studies dentin was immersed in solutions containing ions leached from different silicate-based materials without dentin-material contact, and consequently long times (14 days to 1 month) are required to achieve the remineralization of dentin.

The aim of this study was to test the remineralization of dentin by experimental MTA-based cements using a setup involving a dentin-material contact, with the aim to mimic clinical conditions.

7.2 Materials and Methods

The composition of the experimental wTC-Ba and lc-MTA cements is reported in section 6.2.

Vitrebond was used as HEMA-PAA-containing control base material: its composition and preparation are reported in section 3.2.

The dentin-remineralization ability (bioremineralization of demineralized dentin) has been evaluated as the capability to induce the formation of apatite on previously demineralized human dentin. Human dentin slices (5 ± 2 mm side and 0.8±0.1 mm thick, surface area 30 mm^2 + 24 mm^2 = 54 mm^2) from molar teeth extracted for orthodontic/surgical reasons were prepared at Laboratory of Biomaterials, Department of Odontostomatological Science, University of Bologna (Prof. C. Prati and Dr. M.G. Gandolfi) and demineralized in 15 mL of EDTA 17% for 2 h at room temperature. Disks of set materials (8 mm diameter and 1.6 mm thick) were prepared using PVC rings as moulds. An innovative setup (*DRT Gandolfi technique*) was used for dentin remineralization: each material disk was maintained in close contact with a demineralized dentin slice using a tailored PVC support and soaked in 15 mL of DPBS at 37°C for 7 days. After this time, the dentin slice

was removed from the support, rinsed with deionized water and then analyzed by ATR/FTIR spectroscopy.

7.3 Results

Demineralized dentin

Figure 7.1 shows the IR spectra recorded on the surface of a dentin slice before and after the demineralization treatment with EDTA.

IR analyses confirmed that the used EDTA treatment was able to remove the mineral phase of dentin to a depth of 2 μm at least (i.e. the depth investigated by ATR/FT-IR spectroscopy); in fact, the spectrum recorded after the treatment (Figure 7.1) showed only the bands due to collagen, while the spectral features typical of the apatite component were no longer observed.

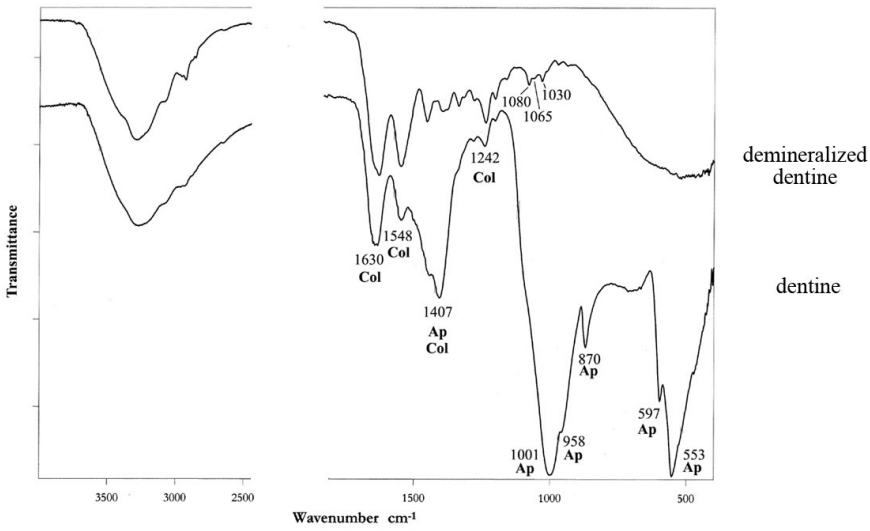

Figure 7.1: IR spectra recorded on the surface of a dentin slice before and after treatment with EDTA 17% for 2 h (apatite-depleted demineralized dentin). The bands prevalently due to collagen (Col) and apatite (Ap) have been indicated.

Demineralized dentin after contact with experimental cements for 7 days in DPBS

Figures 7.2 and 7.3 show the IR spectra recorded on the surface of demineralized dentin after contact with the wTC-Ba and lc-MTA cements for 7 days in DPBS.

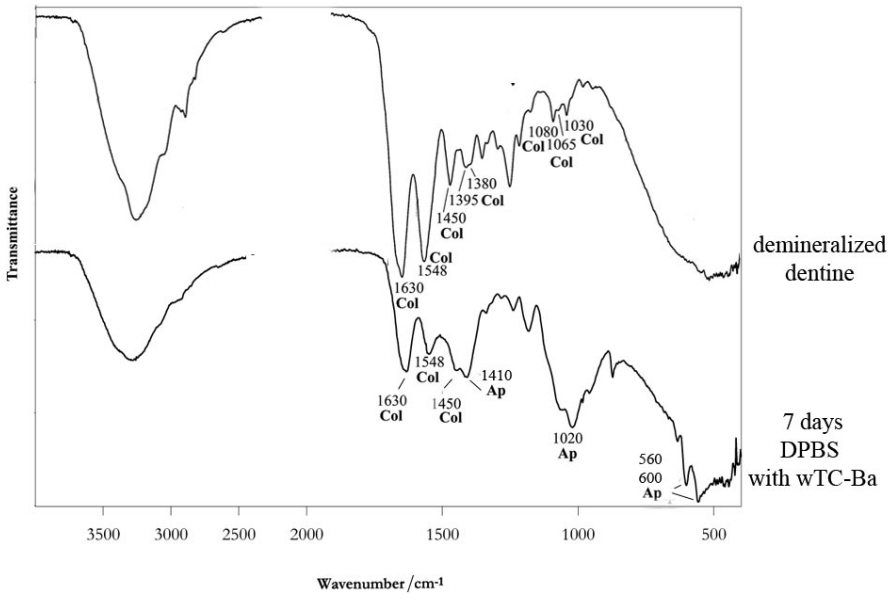

Figure 7.2: IR spectra recorded on the surface of demineralized dentin before and after contact with wTC-Ba for 7 days in DPBS. The bands prevalently due to collagen (Col) and apatite (Ap) are reported.

The demineralized dentin samples treated with the wTC-Ba and lc-MTA cements remineralized, as revealed by the appearance of the apatite bands at about 1400, 1020 and 600 cm^{-1} (Figures 7.2 and 7.3).

To gain more insight into the nature of the apatite phase formed on dentin, the powders formed in the DPBS soaking media where the cements aged in contact with dentin were collected and analyzed. Their IR spectra are reported in Figure 7.4.

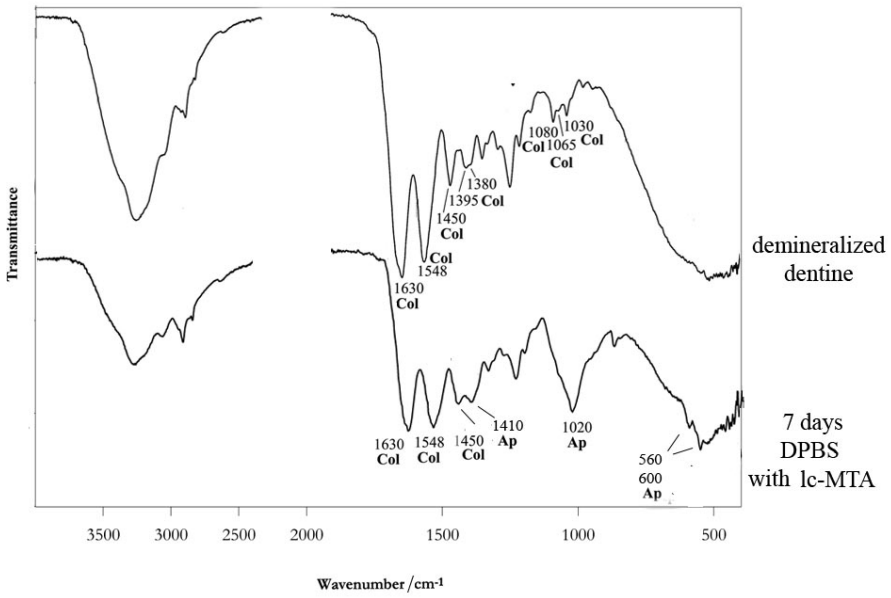

Figure 7.3: IR spectra recorded on the surface of demineralized dentin before and after contact with lc-MTA for 7 days in DPBS. The bands prevalently due to collagen (Col) and apatite (Ap) are reported.

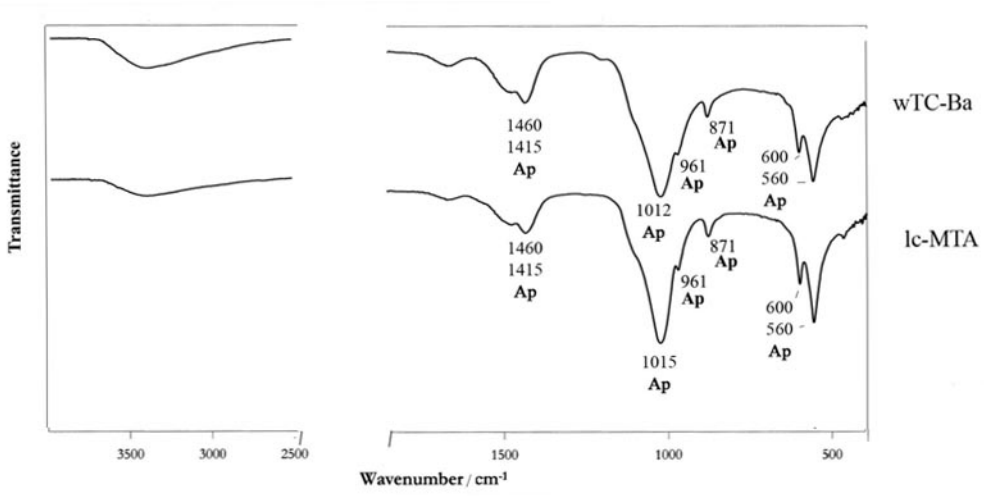

Figure 7.4: IR spectra of the powder isolated from the DPBS medium where wTC-Ba and lc-MTA aged in contact with demineralised dentin for 7 days. The bands prevalently due to apatite (Ap) have been indicated.

The apatite phase formed upon contact with the experimental cements (Figures 7.2 and 7.3), was significantly different from that typical of sound dentin (Figures 7.1) as well as from the apatite powder isolated from the DPBS storage medium (Figure 7.4); in fact, the phosphate asymmetric stretching mode in the above mentioned samples fell at different wavenumber values, i.e. at about 1020, 1001 and 1012-1015 cm^{-1}, respectively.

Figure 7.5 shows the IR spectrum recorded on the surface of demineralized dentin after contact with Vitrebond for 7 days in DPBS.

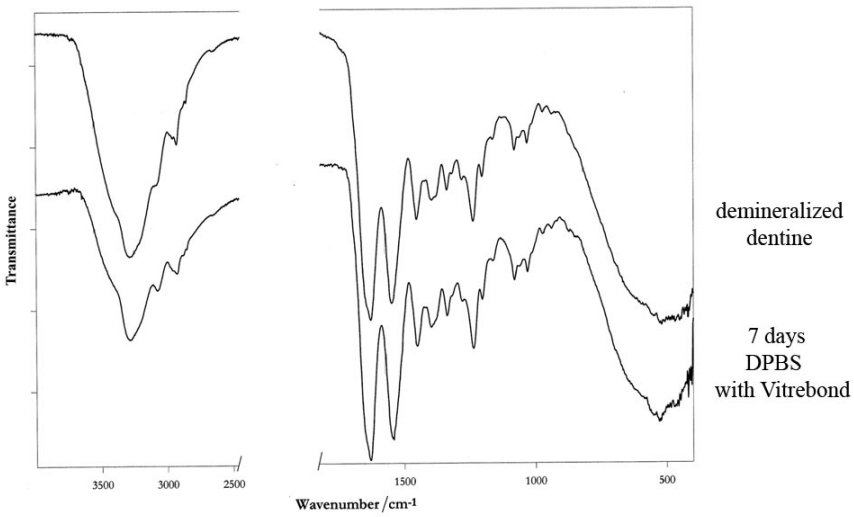

Figure 7.5: IR spectra recorded on the surface of demineralized dentin before and after contact with Vitrebond for 7 days in DPBS.

Minor or no significant spectral changes were observed after treatment with Vitrebond.

7.4 Discussion

The study demonstrated that the presence of the experimental calcium silicate-based composites in contact with demineralized dentin surfaces induced a significant remineralization of the demineralized dentin surface.

The concept of remineralization is based on the reincorporation of mineral (apatite) in dental tissues (dentin or enamel). Remineralization of demineralized/carious dentin occurs by incorporation of mineral ions (calcium, phosphate, fluoride) from the oral fluid or from external sources (specific treatments), through the growth of existing apatite crystals (belonging to remnant crystallites in the subsurface) [14-15]. The mineral precipitated may act as a constant site for further nucleation of mineral promoting a continuous remineralization over time when in presence of environmental mineral ions.

IR spectroscopy gives information on the mineral content (i.e. collagen/apatite ratio) and mineral crystallinity, but is not able to differentiate between the contributions of intra- and extrafibrillar mineral.

In this chapter, IR spectroscopy in the ATR technique has been used to non-destructively verify the efficiency of the demineralization procedure as well as the extent of the remineralization process.

Remineralization of dentin can occur either by the simple precipitation of mineral into the loose demineralized dentin matrix between collagen fibrils (net remineralization) or by the chemical tight association of mineral to the dentin matrix structure (functional remineralization). The simple precipitation of mineral generates an increased mineral content, but may not necessarily provide an optimal interaction with the organic components of the dentin matrix.

The position of the phosphate asymmetric stretching IR band at about 1000 cm^{-1} (Figure 7.2 and 7.3) suggested that the newly formed apatite, although not perfectly coincident with that of sound dentin (Figure 7.1), had a different nature with respect to that isolated from the DPBS storage medium (Figure 7.4).

This result demonstrated that the apatite phase formed on dentin was intimately bound to it, and not simply a phase deposited on its surface.

7.5 Conclusion

The dentin bioremineralization ability of the wTC-Ba and lc-MTA cements was studied using IR spectroscopy. The study demonstrated that these cements induced a significant remineralization of the demineralized dentin surface.

7.6 References

1. S.J. Omelon, M.D. Grynpas. *Chem. Rev.* 2008, **108,** 4694.
2. L.E. Bertassoni, S. Habelitz, J.H. Kinney, S.J. Marshall, G.W. Marshall. *Caries Res.* 2009, **43,** 70.
3. BSI (British Standards Institution). Terminology for the bio-nano interface. PAS132:2007, London, UK.
4. S. Dickens, G. Flaim, S.Takagi. *Dent. Mater.* 2003, **19,** 558.
5. D. Skrtic, J.M. Antonucci, E.D. Eanes. *J. Res. Nat. Inst. Stand. Technol.* 2003, **108,** 167.
6. M.C. Peters, T.C. Fagundes, M.F.L. Navarro, S.H. Dickens. *J. Dent. Res.* 2010, **89,** 286.
7. T. Saito, H. Toyooka, S. Ito, M.A. Crenshaw. *Caries Res.* 2003, **37,** 445.
8. S.E. Efflandt, P. Magne, W.H. Douglas, L.F. Francis. *J. Mater. Sci. Mater. Med.* 2002, **13,** 557.
9. A.P. Forsback, S. Areva, J.I .Salonen. *Act. Odontol. Scand.* 2004, **62,** 14.
10. M. Vollenweider, T.J. Brunner, S. Knecht, R.N. Grass, M. Zehnder, T. Imfeld, et al. *Acta Biomater.* 2007, **3,** 936.
11. H. Yli-Urpo, M. Narhi, T. Narhi. *Biomaterials* 2005, **26,** 5934.
12. N.K. Sarkar, R. Caicedo, P. Ritwik, R. Moiseyeva, I. Kawashima. *J. Endod.* 2005, **31,** 97.
13. F.R. Tay, D.H. Pashley. *Biomaterials* 2008, **29,** 1127.
14. J.D. Featherstone. *Nutr. Q.* 1990,**14,** 5.
15. J.M. ten Cate, J.D. Featherstone. *Crit. Rev. Oral. Biol. Med.* 1991, **2,** 283.

Part III

CHAPTER 8 ALUMINA-ON-ALUMINA HIP IMPLANTS: SEVERE WEAR CASES

8.1 Introduction

Total hip arthroplasty (THA) is one of the most successful surgical procedures with relatively low complication. Although ultra-high molecular weight polyethylene (UHMWPE) is a widely used hip bearing prosthesis, particles detached from this material can cause wear and osteolysis. To solve these problems, different couplings of inert materials have been developed in THA [1-3].

The main reason for failure in hip replacements is the wear caused by the contact stresses on the implants. Ceramics are ideally suited to joint prostheses, because of their hardness and excellent biocompatibility. The introduction of ceramics in the manufacture of components for total joint replacement drastically reduced the wear rate of implants, as described in chapter 1.

The characterization of worn ceramic hip retrievals would be helpful in driving future improvements in design and materials. In a recent study, Affatato et al. have examined the surfaces of some retrieved ceramic specimens in order to compare the damage caused by *in vivo* wear with that observed in *in vitro* tested bearings [4].

Wear surfaces can be classified into two types considering the wear surface profile: wear that produces a relatively smooth wear surface is defined as “mild wear”, while wear that produces a relatively rough worn surface as “severe wear”. More precisely, in the mild wear region, the worn surface shows very fine debris and the roughness is smaller than the grain size, while the severe wear region is dominated by intergranular fracture and pull-out of grains and the surface roughness is in the order of grain size.

Despite the good clinical wear performance of alumina femoral heads, some cases of severe wear were observed combined with visible volume and roundness loss.

In this chapter, the wear damage of severely worn alumina femoral heads is assessed at microscopic level using micro-Raman and fluorescence spectroscopy.

These techniques allow to characterize the wear of the femoral heads at a molecular level according to a piezospectroscopic technique, proposed in the late 1970s [5] and widely applied to the study of alumina [6-11]. The piezospectroscopic effect is defined as the shift of the characteristic frequencies of spectral bands, be they Raman, IR or fluorescence bands, in response to an applied strain or stress.

In this work we concentrated on the analysis of the R_1 and R_2 fluorescence bands of alumina as well as its Raman band at about 419 cm^{-1}.

As described in section 2.3, the R_1 and R_2 fluorescence bands are due to the radiative electronic transitions of the Cr^{3+} ions (present as impurity) which substitute the Al^{3+} ions in the Al_2O_3 lattice. When the lattice of ions surrounding the Cr^{3+} is distorted, for instance by an applied stress, the crystal field potential at the site of the Cr^{3+} ion is altered, which, in turn, alters the energies of the electronic transitions (piezospectroscopic effect). Thus, the analysis of the fluorescence spectrum of Cr^{3+}-containing alumina can give information on the residual stress state of the sample. Analogously, as a consequence of the distortion of the crystal lattice, the Raman bands of alumina, in particular its strongest component at about 419 cm^{-1}, may undergo detectable wavenumber shifts and broadening.

8.2 Materials and Methods

Retrievals

Three alumina-on-alumina bearings explanted 8 to 21 years after implantation (mean follow-up 14 years) were examined. Retrievals consisted of three heads from three patients (one female and two males) who underwent primary THR at Istituto Ortopedico Rizzoli, Bologna - Italy, between 1986 and 1994. Mean patient age was 62 years (range 47-73 years at revision surgery). Two different types of alumina were considered: Monoblock Alumina (Bioceramica, SAMO, Bologna-Italy) and Biolox® (Poral, Anca, Cremascoli, Milan-Italy and Ceramtec, Plochinghen, Germany).

Case	***Ceramic material***	***Gender***	***Age (yrs)***	***Date of implant***	***Date of revision***	***Follow-up (yrs)***	***Type of cup***	***Cause of failure***
# 1	Monoblock Alumina (Bioceramica, SAMO, Bologna-Italy)	M	73	1986	2007	21	Cemented	Cup migration
# 2	Biolox® (Poral, Anca, Cremascoli, Milan-Italy)	M	47	1991	2000	8	Uncemented	Cup migration
# 3	Monoblock Alumina (Bioceramica, SAMO, Bologna-Italy)	F	66	1994	2005	11	Cemented (broken at retrieval)	Loosening
# 4	Biolox® (Ceramtec, Plochinghen, Germany)	F	52	1988	2002	14	Uncemented	Loosening

Table 8.1: Details of the analyzed retrievals.

Table 8.1 reports the details about the retrievals. All the femoral heads presented a severe wear with heavy deviation from the original sphericity and approximately half of the surface was mat.

A retrieved femoral head that did not show severe wear was analysed for comparison (identified as #4 in Table 8.1).

All the retrieved femoral heads were initially sterilized using a formaldehyde-based solution and then washed for 10 min with a detergent solution in an ultrasonically washing machine. After which they were rinsed with distilled water for another 15 min, dried with a jet of filtered inert gas (nitrogen), and further dried in a vacuum drying system for 30 min. Finally, the femoral heads were cleaned with acetone.

Fluorescence and Raman spectra

The fluorescence spectra were obtained using an argon laser (Innova Coherent 70) operating at 514 nm to excite the fluorescence and a Jasco NRS-2000C micro-Raman spectrometer equipped with a 160 K frozen digital CCD detector (Spec-10: 100B, Roper Scientific Inc.) to collect the emitted fluorescence. To ensure that no laser heating occurred and contributed to the observed frequency shifts, all measurements were performed at a low laser power (i.e. 1 mW). Since instrumental fluctuations represent another source of possible variation in the measured frequency, a characteristic neon line at 14431 cm^{-1} was used as a frequency calibration standard.

The spectra were recorded in back-scattering conditions with 1 cm^{-1} spectral resolution using an objective lens of 100× magnification. The spectra were recorded in a non-destructive way. A retrieval which did not show severe wear was analyzed for comparison

(sample #4). To obtain a good representation of the stress distribution, 12 spectra at least were collected in different points of the worn area of each femoral head. The same number of spectra was recorded on the unworn border of each component, which was taken as reference.

The bands monitored were at about 14403 cm^{-1} (R_1) and 14433 cm^{-1} (R_2). Their width (expressed as full width at half maximum, FWHM), intensity and frequency were determined by fitting the experimental spectra with mixtures of Lorentzian and Gaussian functions. The fitting was done using a commercial software (OPUS 6.0, Bruker Optik GmbH, Germany).

Micro-Raman spectra were measured in the same areas where fluorescence spectra were taken using the above mentioned instrument, laser, detector and microscope magnification. All the spectra were recorded in back-scattering conditions with 1 cm^{-1} spectral resolution and a power of about 20 mW. The spectra were calibrated by the use of the characteristic neon emission lines. The intensity and FWHM of the Raman band at about 419 cm^{-1} were calculated directly from the spectra using the above mentioned software.

8.3 Results

All the samples contained an adequate Cr^{3+} impurity level for the R_1 and R_2 bands to be recorded with a high signal-to-noise ratio. Figure 8.1 shows the fluorescence spectrum of the unworn region of a femoral head fitted into the R_1 and R_2 at about 14433 and 14403 cm^{-1}, respectively.

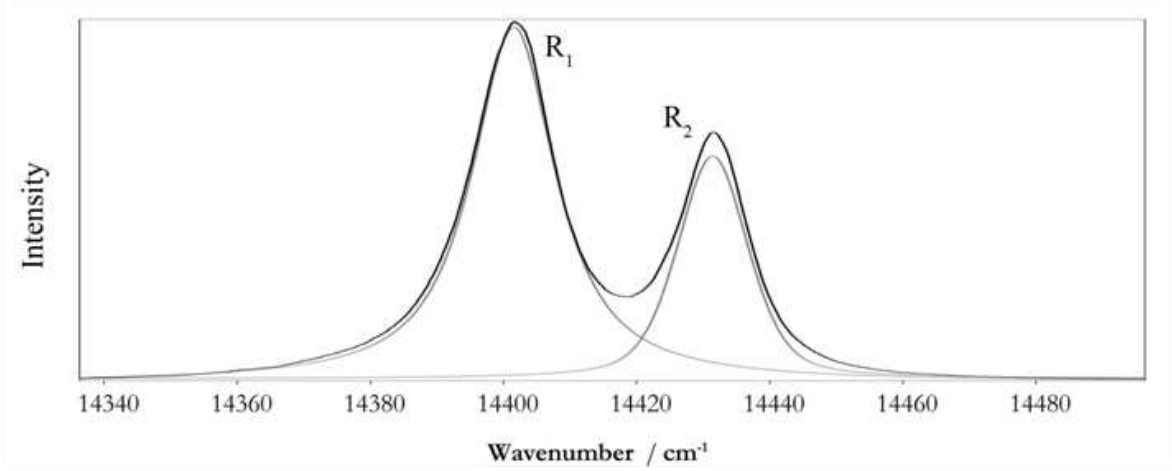

Figure 8.1: Fluorescence spectrum of the unworn region of a femoral head fitted into the R_1 and R_2 components.

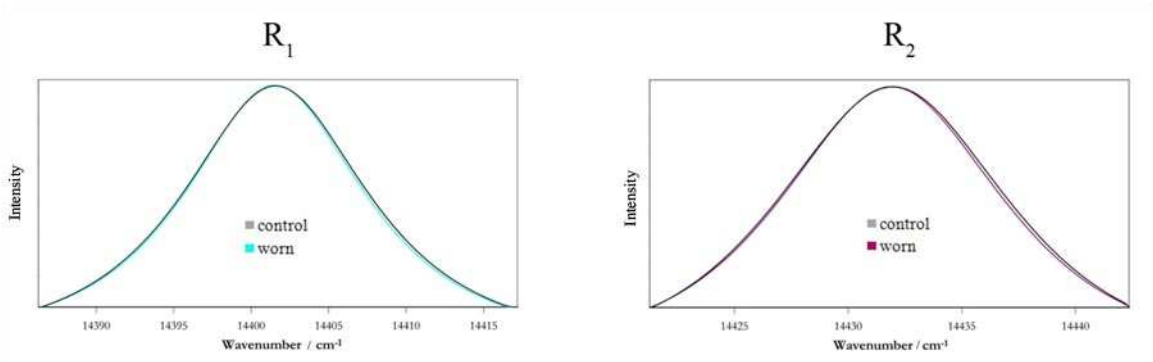

Figure 8.2: Fitted R_1 and R_2 components obtained from the spectra recorded in the unworn (black) and worn (coloured) regions of the femoral head #1.

Figure 8.2 shows the fitted R_1 and R_2 components obtained from the spectra recorded in the unworn and worn regions of the femoral head #1; a significant decrease of the FWHM of both R_1 and R_2 components was observed upon wear. For the samples #2, #3 and #4, no visible spectral changes were observed.

The values of the FWHM of R_1 and R_2 components obtained from the spectra recorded on the unworn and worn areas of the analysed femoral heads are reported in Figure 8.3.

From a quantitative point of view, considering the standard deviation associated to the measurements, significant differences in the R_1 and R_2 FWHM values between unworn and worn areas were observed only for sample #1.

Biolox® components (#2 and #4) showed FWHM values significantly lower than monoblock alumina components (#1 and #3).

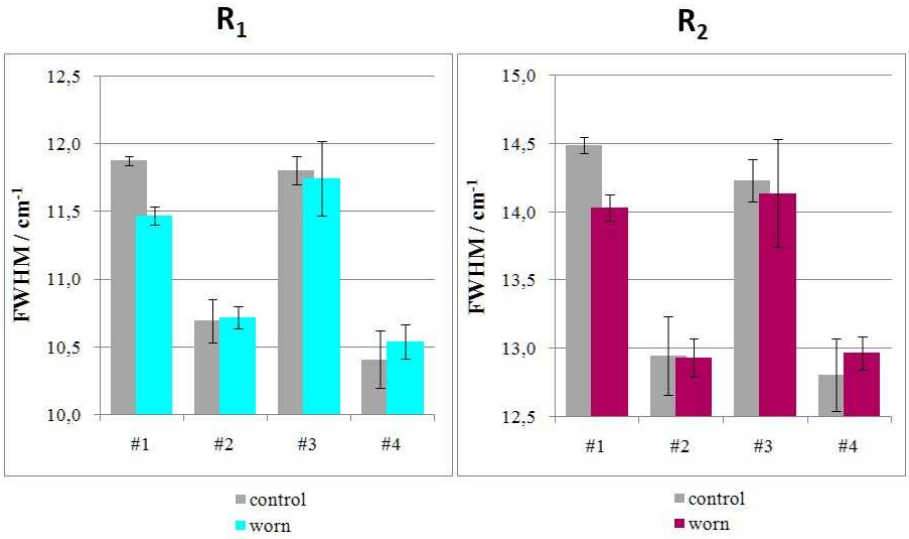

Figure 8.3: Average full width at half maximum **(**FWHM) of the R_1 and R_2 components obtained from the fitting of the fluorescence spectra recorded in the unworn (control) and worn regions of the analyzed femoral heads.

Figure 8.4 shows the Raman spectrum recorded in the unworn region of the femoral head #3. The characteristic bands at about 419 and 380 cm^{-1} were assigned to corundum, according to the literature [12].

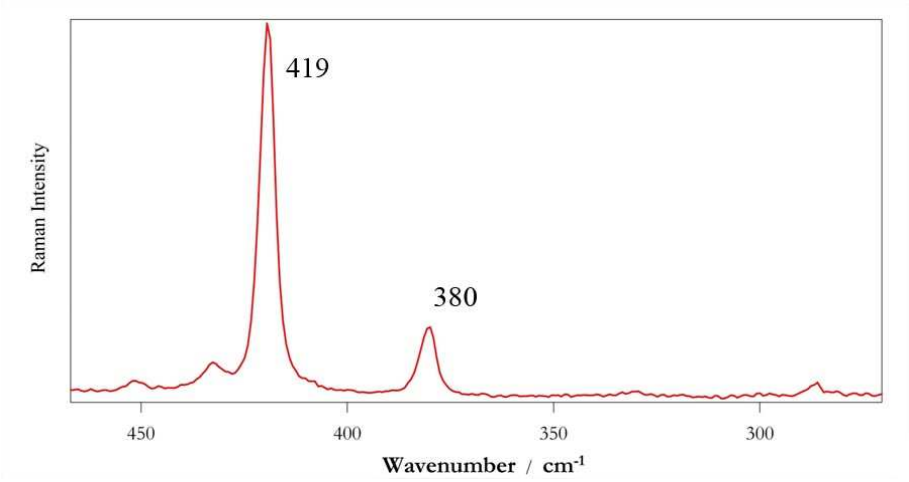

Figure 8.4: Raman spectrum recorded in the unworn regions of the femoral head #3. The main characteristic Raman bands assigned to corundum are displayed.

No significant differences between worn and unworn regions were observed in the Raman of the samples #1, #2 and #4.

Upon wear, a significant broadening and shift in the wavenumber position of the band at 419 cm^{-1} was observed for the sample #3, as displayed in Figure 8.5.

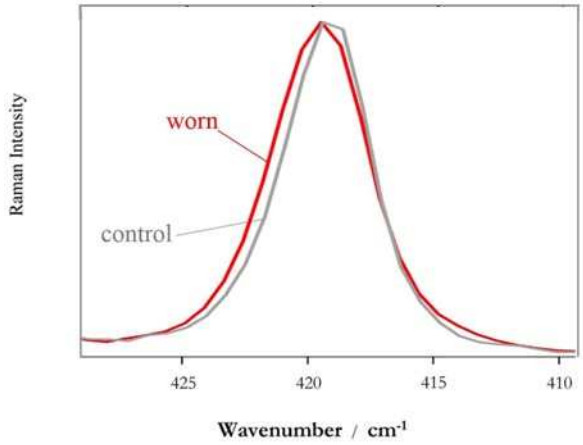

Figure 8.5: Average Raman spectra recorded in the 410-430 cm^{-1} range of the worn (red) and unworn (grey) regions of the femoral head #3.

Figure 8.6 reports the average wavenumber position and FWHM of the Raman band at about 419 cm^{-1}, as obtained from the spectra recorded in the unworn and worn regions of the analysed femoral heads; although nearly all the specimens showed a substantial broadening and shift of the band Raman band upon wear, only in sample #3 this behaviour appeared significant.

In this sample, going from the control region to the worn region, the above mentioned band showed an up-shift from 419.1±0.2 cm^{-1} to 419.6±0.3 cm^{-1} and a broadening from 4.2±0.2 cm^{-1} to 4.7±0.2 cm^{-1}.

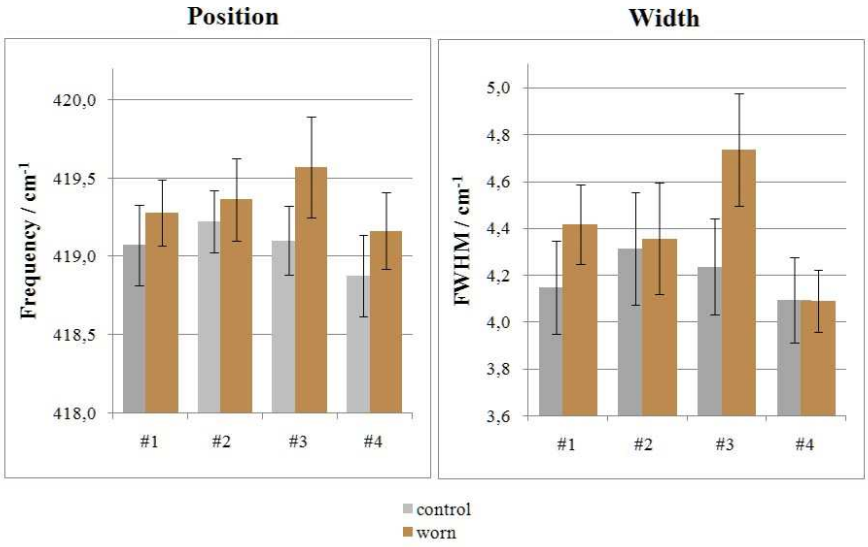

Figure 8.6: Average wavenumber position and FWHM of the Raman band at about 419 cm^{-1}, as obtained from the spectra recorded in the unworn and worn regions of the analysed femoral heads.

8.4 Discussion

This study analysed the wear damage of three femoral heads retrieved from alumina-on-alumina hip prostheses explanted after an average follow-up of 14 yrs of *in vivo* function.

Micro-Raman and fluorescence spectroscopy allowed to characterize the wear of the femoral heads at microscopic level analyzing the morphology of the worn regions.

The positions and widths of the R_1 and R_2 fluorescence bands provided information on the residual stress state of the samples.

No significant differences in the wavenumber position of the R_1 and R_2 bands were observed among the analyzed retrievals. Significant differences in the FWHM of both the fluorescence bands were observed among the unworn areas of the two sets of retrievals (i.e. monoblock alumina and Biolox®) as shown in Figure 8.3: the Biolox® components (#2 and #4) showed noticeably lower FWHM values than the monoblock alumina components (#1 and #3), suggesting a narrower distribution of residual stress in the former.

The FWHM of the R_1 and R_2 bands showed a different trend in the two sets of retrievals upon wear. A general decrease in this parameter was observed for both monoblock alumina components (#1 and #3); however, this trend appeared significant only for femoral head #1. The broadening of the fluorescence band upon wear could indicate the occurrence of microcracking that can reduce the width of the Gaussian residual stress distribution as a consequence of stress dissipation [13]. An analogous result was reported for a fractured alumina femoral head tested under severe conditions **[**14**]**.

As reported in Figure 8.3, Biolox® femoral heads showed a substantial constancy (#2) or slight decrease of the FWHM of both bands; however, the latter change did not appear significant. No significant wavenumber shifts were observed in any of the femoral heads by effect of wear.

Raman results confirmed that the monoblock alumina components were more degraded than the Biolox® components; the femoral head #3 showed the most significant changes in both the position and FWHM of the Raman band at about 419 cm^{-1} (Figures 8.4 and 8.5).

The volumetric wear of the analysed retrievals was assessed by Dr. S. Carmignato at the Department of Management and Engineering of the University of Padova, using a coordinate measuring machine (CMM).

The spectroscopic trends appeared in agreement with the CMM results since the samples that showed the most significant wear-induced changes in fluorescence and Raman bands (i.e. #1 and #3, respectively) were those characterized by the highest volumetric wear. In the light of the spectroscopic results, it can be affirmed that the femoral heads characterized by the most severe wear underwent the most significant stress at a molecular level.

8.5 Conclusions

This study analysed at a microscopic level the severe wear damage of three retrieved alumina femoral heads.

Differences in the distribution of residual stresses among monoblock alumina and Biolox® components were revealed by fluorescence spectroscopy.

The occurrence of microcracking can be suggested for monoblock alumina upon severe wear. Raman results confirmed that the monoblock alumina components were more degraded than the Biolox® ones.

The comparison of volumetric wear measurements and spectroscopic results showed that the femoral heads characterized by the most severe wear underwent the most significant

stress at a molecular level.

8.6 References

1. J.J. Callaghan, J.M. Cuckler, J.I. Huddleston, J.O. Galante. *J. Am. Acad. Orthop. Surg.* 2008, **16,** S33.
2. C. Pattyn, K.A. De Smet. *Orthopedics* 2008, **31,** 1078.
3. D.P. Rhoads, K.C. Baker, R. Israel, P.W. Greene. *J. Arthropl.* 2008, **23,** 25.
4. S. Affatato, F. Traina, M. De Fine, S. Carmignato, A. Toni. *J. Bone Joint Surg. Br.* 2012, **94B,** 37.
5. L. Grabner. *J. Appl. Phys.* 1978, **49,** 580.
6. J. Hue, D.R. Clarke. *J. Am. Ceram.* Soc. 1995, **78,** 1347.
7. R. Krishnan, R. Kesavamoorthy, S. Dash, A.K. Tyagi, B. Raj. *Scripta Mater.* 2003, **48,** 1099.
8. P. Taddei, S. Affatato, C. Fagnano, A. *Toni, J. Mat. Sci.* 2006, **41,** 399.
9. S. Affatato, R. Torrecillas, P. Taddei, M. Rocchi, C. Fagnano, G. Ciapetti, A. Toni, *J. Biomed. Mater. Res. B Appl. Biomater.* 2006, **78B,** 76.
10. P. Taddei, S. Affatato, R. Torrecillas, C. Fagnano, P. Ferrieri, A. Toni, *J. Mater. Sci.* 2006, **41,** 5310.
11. J. Chevalier, P. Taddei, L. Gremillard, S. Deville, G. Fantozzi, J. F. Bartolomé, C. Pecharroman, J. S. Moya, L.A. Diaz, R. Torrecillas, S. Affatato, *J. Mech. Behav. Biomed. Mater.* 2011, **4,** 303.
12. S.P.S. Porto, R.S. Krishnan. *J. Chem. Phys.* 1967, **47,** 1009.
13. M. Ortiz, S. Suresh. *J. Appl. Mech.* 1993, **60,** 77.
14. P. Taddei, S. Affatato, C. Fagnano, A. Toni. *J. Mater. Sci.* 2006, **41,** 399.

CHAPTER 9 - RETRIEVAL ANALYSIS OF THREE GENERATIONS OF BIOLOX® FEMORAL HEADS

9.1 Introduction

Alumina was introduced about 40 years ago, with good clinical results. The first generation of alumina ceramics for hip joints, obtained from chemically purified and grounded corundum powders sintered in air, was marketed since 1974 with the trade name of Biolox®. It was used for femoral heads, monolithic sockets, and liners for modular acetabular cups accordingly to ISO 6474 and other international regulations.

The alumina quality is influenced by several factors such as grain size, density and purity. The grain size of alumina influences the wear rate that decreases with decreasing grain size [1].

In the 1990ies alumina hip joints were improved with the introduction of Biolox® *forte*, whose mechanical characteristics were highly enhanced thanks to innovations in the production process. Biolox® *forte* has become commercially available since 1995; this material was produced using an improved raw material, which had a smaller grain size, lower level of impurities and was sintered in air. Biolox® *forte* has a density of 3.98 g/cm^3, compared to 3.96 g/cm^3 for Biolox® and grain sizes of 3.2 μm compared to 4.2 μm for Biolox®, in addition to an enanched flexural strength.

Biolox® *forte* is bioinert and is highly resistant to all chemical reactions as a result of its high purity and the strong chemical bonding of its crystalline structure.

At present, there is no other material available on the market for joint couplings that is equal to Biolox® *forte* for wear, biocompatibility, chemical stability, and allergenicity.

With the exception of diamond, Biolox® *forte* constitutes the hardest material known; thanks to this property, it can remain undamaged if scratched during implantation.

The last generation of ceramic materials for hip joint prostheses is represented by Biolox® *delta:* it was introduced to the market in 2000 as ceramic biocomposite material intended for special medical applications requiring the highest performance, which was not previously possible using alumina ceramics: an example are the extra-long femoral heads with a diameter of 22 mm for which the poor toughness of alumina represented a seriuos limitation.

Biolox® *delta* is a hot isostatic pressed zirconia-toughened alumina composite material specifically engineered to obtain substantially improved mechanical properties.

This material exhibits an extremely high fracture toughness and a much higher capacity than other ceramic materials to resist the onset of cracking and to arrest the propagation of cracks [2]. The Biolox® *delta* ceramic has been developed with the aim to combine the best characteristics of both alumina and zirconia (the excellent strength and toughness of alumina and the higher performances of alumina in terms of wear, chemical and hydrothermal stability).

Biolox® *delta* consists of an alumina matrix (about 75% wt) providing the material hardness and wear resistance, in which particles of Y-TZP (about 24% wt) are dispersed to improve the mechanical properties; the composite also contains 1% of Cr_2O_3, added into the formulation to counterbalance the reduction of hardness caused by the introduction of zirconia. The presence of such an amount of chromium oxide also confers the charachteristic ruby-pink coloration to the material.

Under stress conditions (e.g. at the crack tip), the Y-TZP particles exhibit a t-m phase transition, according to the mechanism described in chapter 1, which enhances material

fracture resistance. In addition to normal transformation-toughening, a second toughening mechanism is expected to be active with the addition of SrO; this oxide induces the formation of strontium aluminate platelets ($SrAl_{12-x}Cr_xO_{19}$) during the sintering step of the production process. Due to their size, these flat, elongated crystals prevent any cracks from advancing by dissipating crack energy. In fact, when the crack reaches one of these crystals, it needs extra energy to go round it; in the absence of this, the crack does not propagate.

This chapter deals with the examination of wear phenomena in 15 explanted ceramic-on-ceramic (COC) hip joints (Biolox®, Biolox® *forte*, and Biolox® *delta*) retrievals, evaluating the residual stress state in the worn femoral heads using a fluorescence piezospectroscopic technique.

9.2 Materials and Methods

Retrievals

Fifteen ceramic-on-ceramic (COC) bearings explanted 1 month to 26 years after implantation (mean 9 years) were examined (case #15 was not considered in the computation of mean folluw-up). Retrievals consisted of femoral heads obtained from 15 patients who underwent primary THA at Istituto Ortopedico Rizzoli between 1982 and 2009. Among the explanted specimens, there were 5 from male patients and 10 from female patients with a median age of 64 years (range 35 to 86 years) at revision surgery. Details about this population are shown in Table 9.1. The explanted specimens consisted of five alumina Biolox®, five alumina Biolox® *forte*, and five alumina Biolox® *delta*. The main reasons for failure of the index of arthroplasty were dislocations (27.6%) and aseptic loosening (22.1%) of the acetabular component in all design components. Due to the

scarce number of available specimens and different types of ceramic used, partial and limited reports are available in literature. Biolox® *forte* and *delta* ceramics were introduced for THA applications in 1995 and 2000, respectively; long-term *fu* studies (with average *fu* >10 *yrs*) were possible only for the first alumina generation (Biolox®) and in this context, only the femoral heads were considered.

The femoral heads were treated as described in Chapter 8.

Alumina generation	**Implant year**	**Gender**	**Age (yrs)**	**fu (yrs)**	**Weight (Kg)**	**Case**
Biolox®	1982	M	51	26	60	#01
Biolox®	1986	F	74	21	70	#02
Biolox®	1988	F	66	14	65	#03
Biolox®	1991	M	52	8	68	#04
Biolox®	1994	F	86	12	70	#05
Biolox® *forte*	1997	F	35	3	70	#06
Biolox® *forte*	2000	F	47	7	50	#07
Biolox® *forte*	2001	M	73	7	88	#08
Biolox® *forte*	2005	M	59	3	55	#09
Biolox® *forte*	2006	F	49	2	60	#10
Biolox® *delta*	1999	F	77	8	78	#11
Biolox® *delta*	2003	F	48	5	57	#12
Biolox® *delta*	2006	F	78	3	85	#13
Biolox® *delta*	2009	F	85	1	78	#14
Biolox® *delta*	2009	M	80	1 month	73	#15

Table 9.1: Details of the retrievals studied.

Fluorescence measurements

The fluorescence spectra were obtained using the instrumental setup described in chapter 8 with the exception of the microscope objective: a lens of 10× magnification was used. This configuration provided a laser spot size larger than the grain size of the ceramics, assuring that the fluorescence was being averaged over a large number of grains.

The spectra were recorded in a non-destructive way on five femoral heads of each generation; to obtain a good representation of the stress distribution, 12 spectra at least were collected in different points of the worn area of each femoral heads. The same number of spectra were recorded on the unworn border of each component, which was taken as reference. A new Biolox® *delta* femoral head dated back to 2009 was analysed for comparison.

The bands parameters of the R_1 and R_2 fluorescence components were computed as described in chapter 8.

9.3 Results

Figures 9.1 and 9.2 report the average fluorescence spectra recorded on the control unworn areas of all the analysed Biolox®, Biolox® *forte* and Biolox® *delta* femoral heads. Significant differences can be observed between the three sets of femoral heads with regards to the intensity (Figure 9.1) and FWHM (Figure 9.2) of the R_1 and R_2 bands, while the wavenumber position of the fluorescence bands remained practically constant.

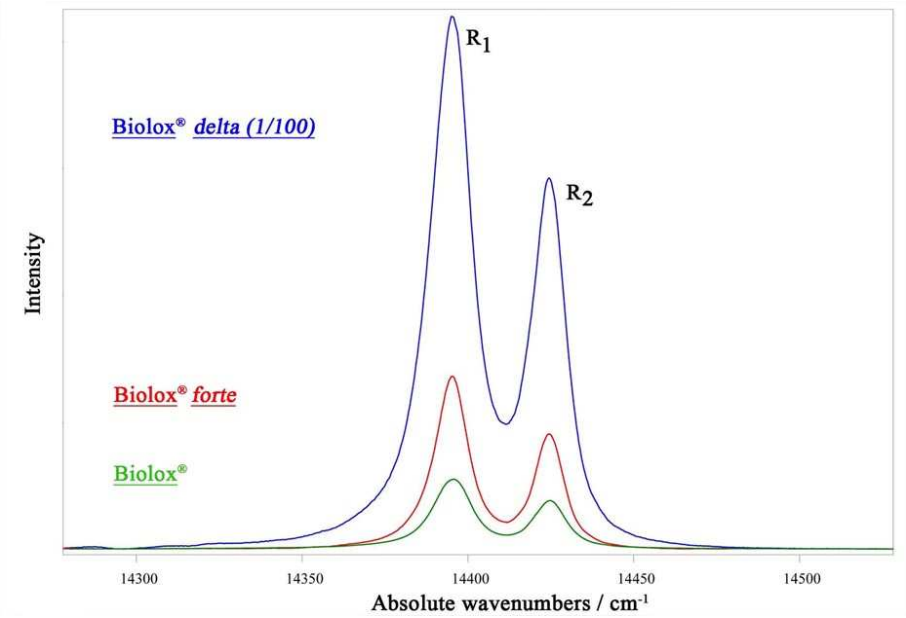

Figure 9.1: Average fluorescence spectra recorded on the control unworn areas of all the analysed Biolox® (green), Biolox® *forte* (red) and Biolox® *delta* (blue) femoral heads. The relative intensities of R_1 and R_2 components in the three materials are highlited.

The R_1 and R_2 components were obviously significantly stronger in Biolox® *delta* than in Biolox® and Biolox® *forte* femoral heads, due to the presence of the Cr_2O_3 additive. Biolox® *forte* showed a slightly higher fluorescence than Biolox®, due to its better surface finishing.

Figure 9.2 and Table 9.2 show the comparison between the average FWHM values of the R_1 and R_2 components of the three material generations.

Control areas of the three sets of femoral heads appeared significantly different also in the FWHM of the R_1 and R_2 bands. Biolox® *forte* showed the lowest values for both these markers of residual stress distribution, while Biolox® and Biolox® *delta* appeared comparable to each other.

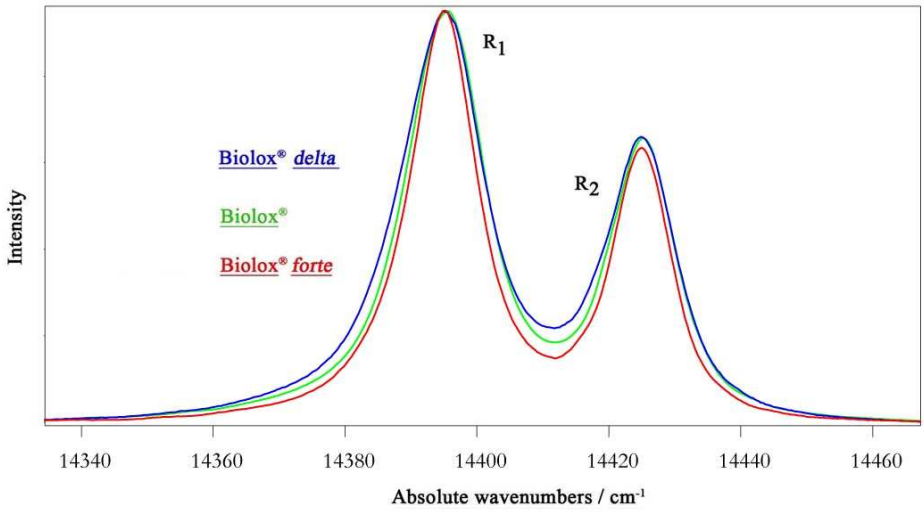

Figure 9.2: Average fluorescence spectra recorded on the control unworn areas of all the analysed Biolox® (green), Biolox® *forte* (red) and Biolox® *delta* (blue) femoral heads. The spectra were normalized to the intensity of the R_1 component.

	FWHM (cm^{-1})			
	R_1	S.D.	R_2	S.D.
Biolox® *delta*	14.9	±0.7	12.6	±0.4
Biolox® *forte*	12.8	±0.5	11.0	±0.2
Biolox®	14.2	±0.6	12.2	±0.4

Table 9.2: Average full width at half maximum (FWHM ± standard deviation) of the R_1 and R_2 bands obtained by fitting the experimental fluorescence spectra reported in Figures 9.1 and 9.2.

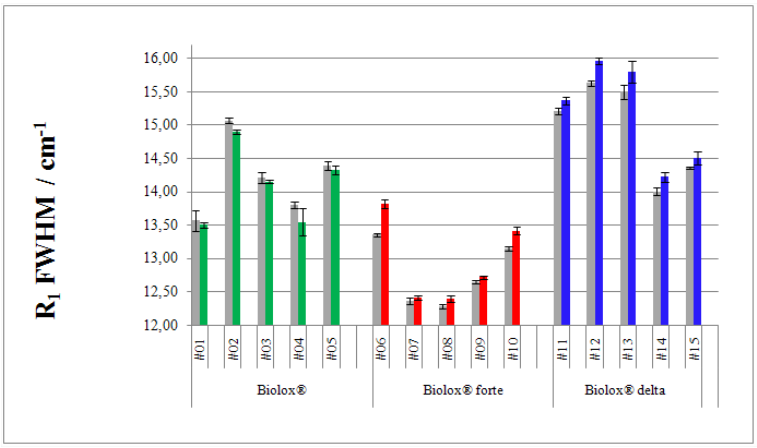

Figure 9.3: Average full width at half maximum (FWHM ± standard deviation) of the R_1 band as obtained by fitting the experimental fluorescence spectra recorded in worn (coloured) and control (grey) regions of each retrieval. The data reported are mean values referring each to 12 spectra.

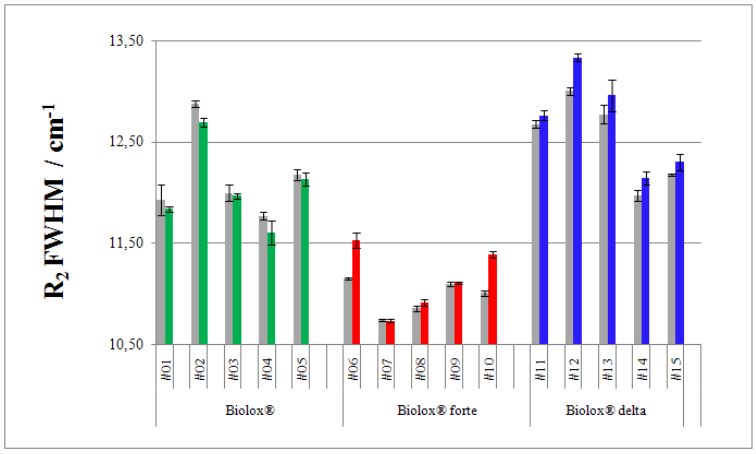

Figure 9.4: Average full width at half maximum (FWHM ± standard deviation) of the R_2 band as obtained by fitting the experimental fluorescence spectra recorded in worn (coloured) and control (grey) regions of each retrieval. The data reported are mean values referring each to 12 spectra.

The worn areas of the femoral heads showed significant differences if compared with their respective control areas, especially in the FWHM of the R_1 and R_2 bands (Figures 9.3 and

9.4**)**. No wavenumber shifts were observed in any of the femoral heads. From a general point of view, the standard deviation associated to the mean FWHM values of both R_1 and R_2 bands in the worn areas was often higher than in the control areas, indicating a higher dispersion due to wear.

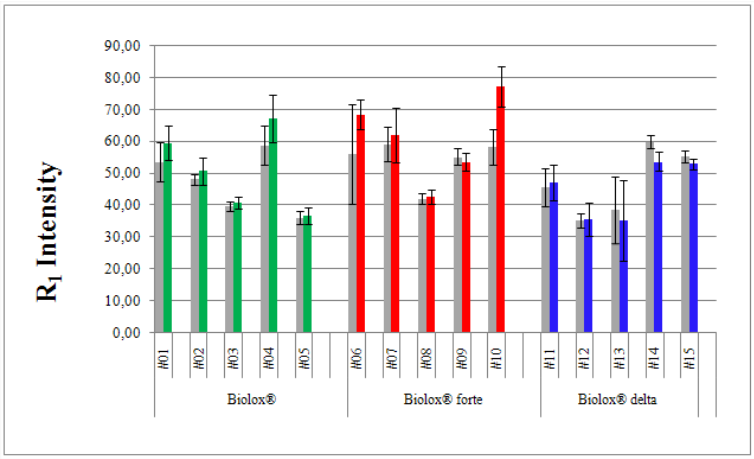

Figure 9.5: Average intensity of the R_1 band as obtained by fitting the experimental fluorescence spectra recorded in worn (coloured) and control (grey) regions of each retrieval. The data reported are mean values referring each to 12 spectra. The Biolox® *delta* values are reported scaled with a factor of 100.

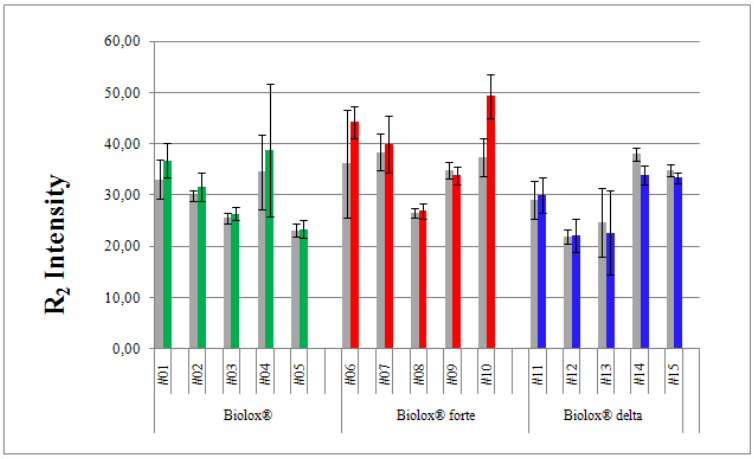

Figure 9.6: Average intensity of the R_2 band as obtained by fitting the experimental fluorescence spectra recorded in worn (coloured) and control (grey) regions of each

retrieval. The data reported are mean values referring each to 12 spectra. The Biolox® *delta* values are reported scaled with a factor of 100.

Figures 9.5 and 9.6 show the trend of the fluorescence intensity upon wear. A general (even if rarely significant) increase of fluorescence intensity was observed in both Biolox® and Biolox® *forte* sets, probably due to polishing related to wear. From this point of view, Biolox® *delta* showed a different behaviour: no increase in fluorescence intensity was observed in the worn areas of the femoral heads.

With regards to Biolox®, all the femoral heads showed a general decrease of the FWHM of both R_1 and R_2 bands, although this change appeared significant only for sample # 02; this result did not appear surprising in the light of the massive wear experimented by this retrieval. Biolox® *forte* and Biolox® *delta* showed a different behaviour at fluorescence measurements; actually, all these femoral heads underwent a general FWHM increase, which appeared significant for several retrievals.

9.4 Discussion

The fluorescence measurements allowed to detect several differences in the three sets of retrievals.

As shown in Figure 9.1, the intensity of the R_1 and R_2 fluorescence bands provided information on surface finishing: Biolox® *forte* showed a slightly higher fluorescence than Biolox®, due to its better surface finishing, according to manufacturer claims.

Fluorescence measurements already proved suitable to investigate density and surface finishing of ceramic components [3-6]; high fluorescence intensity is indicative of a

material with low porosity, since pores act as scattering centres of the incident laser beam and are responsible for a lower fluorescence intensity.

In the unworn area of the retrievals, the FWHM of the R_1 and R_2 bands increased going from Biolox® *forte* to Biolox® and Biolox® *delta*. This result would suggest a narrower distribution of residual stress in the former, while Biolox® and Biolox® *delta* appeared comparable to each other (Figure 9.2 and Table 9.2).

As shown in Figures 9.5 and 9.6, upon wear, the intensity and the FWHM of the R_1 and R_2 bands changed in different ways in the three sets of retrievals, suggesting different wear mechanisms. The increase in the fluorescence intensity observed in the Biolox® and Biolox® *forte* retrievals suggests that the friction generated at the articulating surface generated a significant polishing effect. This phenomenon improved the quality of the surface, thus increasing fluorescence [3]; on the contrary, no significant changes in the fluorescence intensity upon wear were observed in Biolox® *delta* retrievals, suggesting a negligible change in the surface finishing. Also the FWHM of the R_1 and R_2 bands showed a different trend in the three sets of retrievals upon wear: a significant increase in this parameter was observed for both Biolox® *forte* and *delta* (Figures 9.3 and 9.4), suggesting a wider range of residual stress values [3]. On the contrary, in the worn area of the Biolox® components both R_1 and R_2 bands sharpened upon wear, probably due to microcracking [7]. This results could appear in disagreement with the findings reported in chapter 8 that indicate that Biolox® retrievals did not show microcracking also under severe wear conditions. This mismatching can be explained by the different microscopy objectives used: the 10× magnification lens assures that the fluorescence was being averaged over a large number of grains, while the 100× lens generates a spot smaller (about 1 μm) than

Biolox® grain size (4.2 μm). It is reasonable to suppose that microcracking may be less detectable with the instrumental configuration used in previous chapter.

9.6 Conclusions

The wear of three generation of ceramic retrievals (Biolox®, Biolox® *forte*, and Biolox® *delta*) was examinated using a fluorescence piezospectroscopic technique.

The fluorescence measurements suggested different wear mechanisms in the three sets of retrievals. Microcracking was predominant in Biolox®, while in Biolox® *forte* and Biolox® *delta* a wider range of residual stress values was observed upon wear. Surface polishing was observed only in Biolox® and Biolox® *forte*.

9.6 References

1. A.K. Mukhopadhyaya, M. Yiu-Winga. *Wear* 1993, **162-164**, 258.

2. Ceramtec. BIOLOX® delta – Nanocomposite for Arthroplasty. 2011.

3. M.A. Garcia, S.E. Paje, J. Llopis. *Mater. Sci. Engineer.* 2002, **A325,** 302.

4. R. Krishnan, R. Kesavamoorthy, S. Dash, A.K. Tyagi, B. Raj. *Scripta Mater.* 2003, **48,** 1099.

5. J. Chevalier, P. Taddei, L. Gremillard, S. Deville, G. Fantozzi, J.F. Bartolomé, et al. *J. Mech. Behav. Biomedi. Mater.* 2011, **4,** 303.

6. P. Taddei, S. Affatato, R. Torrecillas, C. Fagnano, P. Ferrieri, A. Toni. *J. Mater. Sci.* 2006, **41,** 5310.

7. M Ortiz, S Suresh. *J. Appl. Mech.* 1993, **60,** 77.

CHAPTER 10 - RAMAN AND FLUORESCENCE INVESTIGATIONS ON RETRIEVED BIOLOX® *DELTA* FEMORAL HEADS

10.1 Introduction

Biolox® *delta* is currently extensively used as prosthetic components for total hip replacement in consequence of its high strength, wear resistance and stability, non-toxicity and biocompatibility *in vivo* [1,2].

Ageing of zirconia is the negative consequence of the transformation ability of the tetragonal phase involved in the toughening mechanism. The presence of water molecules (or body fluids) on the surface of tetragonal zirconia may induce its progressive transformation into the monoclinic phase.

The occurrence of the t-m transformation in Biolox® *delta* and Y-TZP components is a still debated subject [3-5]. The manufacturer claims that Biolox® *delta* was specifically developed with the aim of avoiding ageing phenomena; actually, earlier studies on Biolox® *delta* femoral heads did not report any significant t-m phase transformation after environmental exposure to water vapour [6,7]. More recent investigations have shown that Biolox® *delta* femoral heads underwent significant phase changes after *in vitro* aging accelerated tests [8,9]. Actually, the latter studies have reported no strength decrease, no roughening and a minimal surface damage.

This chapter is aimed at correlating the data here obtained for the first time on Biolox® *delta* retrievals with those reported in the literature on *in vitro* ageing.

The first goal was the Raman spectroscopic analysis of several Biolox® *delta* femoral retrievals to evaluate the occurrence of a t-m zirconia transformation. Several Raman

quantitative methods have been proposed in the literature to monitor this transformation [10] based on the fact that the monoclinic and tetragonal polymorphs of zirconia have characteristic Raman bands, whose intensity is proportional to their concentration. While Raman spectroscopy has been widely applied to the study of *in vitro* aged and fractured zirconia-containing components [8,11] at our knowledge, this is the first Raman study on Biolox® *delta* retrievals.

As a second goal, the fluorescence results reported in chapter 9 were correlated to Raman findings.

10.2 Materials and Methods

Retrieved Biolox® delta femoral heads

A total of six retrieved Biolox® *delta* (CeramTec AG, Plochingen, Germany) femoral heads were investigated. Five retrievals are those presented in chapter 9: a supplementary femoral head was analysed. The samples are here reordered on the basis of the implant year. They were all revised after periods comprised between 1 month and 8 years after implantation (average follow-up 3.2 years) from Biolox® *delta*-on-Biolox® *delta* hip joints, as summarized in Table 10.1.

The retrievals were obtained from six patients who underwent primary THA at Istituto Ortopedico Rizzoli between 1999 and 2009. Mean patient age was 72 years (range 57-85 years).

All the femoral heads were treated as described in chapter 8.

Case	Implant year	Gender	Age (yrs)	*Follow-up* (yr)	Weight (Kg)
#01	1999	F	77	8	78
#02	2003	F	48	5	57
#03	2006	F	78	3	85
#04	2007	F	67	2	60
#05	2009	F	85	1	78
#06	2009	M	80	1 month	73

Table 10.1: Details on the Biolox® *delta* retrievals analysed in the present study.

In vitro experiments

To simulate extreme wear conditions, a new unworn Biolox® *delta* femoral head (dated back to 2009) was intentionally fractured at the Laboratorio di Tecnologia Medica (Istituto Ortopedico Rizzoli) to reproduce the stresses induced by the rupture of the implant. The femoral head was coupled with a homologous acetabular cup and the bearing was run into a hip joint simulator (Shore Western, Los Angeles, CA, USA) for 1×10^5 cycles without lubrication. After this treatment, the femoral head was put on an Instron 8502 machine to determine the breaking point. A speed of 0.1 mm per minute was applied and the femoral head was broken after a load of approximately 30 KN. Six fragments of the head (identified as F1, F2..., F6) were analysed in their fractured sections by Raman and

fluorescence spectroscopy. The articulating surface of one fragment was mapped by Raman spectroscopy.

Raman and Fluorescence spectroscopy

Micro-Raman spectra were obtained using the same instrument reported in chapter 8 employing a microscope of 10× magnification and a pinhole with an aperture diameter of 3000 µm. Under these conditions the laser spot size was larger than the grain size of the ceramics, assuring that the spectra were being averaged over a large number of grains. All the spectra were recorded in back-scattering conditions with 5 cm^{-1} spectral resolution and a power of about 35 mW. The spectra were recorded in a non-destructive way on the surface of the six retrievals; to obtain a good representation of the stress distribution, 12 spectra were collected in different points of the worn area of each femoral head. The same number of spectra was recorded on the unworn border of each component, which was taken as reference. A new Biolox® *delta* femoral head dated back to 2009 was analysed for comparison. With regards to the fractured femoral head, 12 spectra were recorded in the section of each fragment. The articulating surface of one fragment was mapped by measuring the Raman spectra at increasing distance moving orthogonally to the edge generated by the break, with steps of 20 µm.

The zirconia monoclinic phase was quantified as volume fraction (V_m) according to the following equation, proposed by Katagiri *et al.*[30]:

$$V_m = \frac{I_m^{181} + I_m^{190}}{2.2 \times I_t^{147} + I_m^{181} + I_m^{190}}$$

where $I_m^{181} + I_m^{190}$ and I_t^{147} were the areas of the monoclinic doublet at about 181 and 190 cm^{-1} and the tetragonal band at 147 cm^{-1}, respectively. This equation was preferred to the

widely applied method proposed by Clarke and Adar [11], which was found to underestimate the fraction of the monoclinic phase [10].

To estimate the depth of extension of the t-m transformation, several tests employing a confocal setup were performed. The worn region of two retrievals was analysed using a microscope of 100× magnification and confocal pinholes with aperture diameters progressively smaller (3000, 200 and 50 μm). No statistically significant differences in the calculated values of V_m were observed under the different instrumental setup conditions (i.e. with different pinholes, which correspond to different sampling depths). This result suggests that the t-m transformation was a massive process involving a thick material area. In the light of these findings, to obtain a higher signal-to-noise ratio, the spectra were recorded using a microscope of 10× magnification and the largest pinhole (i.e. with an aperture diameter of 3000 μm).

The fluorescence spectra were recorded as reported in chapter 9. The bands parameters of the R_1 and R_2 fluorescence components were computed as described in chapter 8.

10.3 Results

Micro-Raman spectra

Figure 10.1 shows the Raman spectra of the crystalline phases present in the composite.

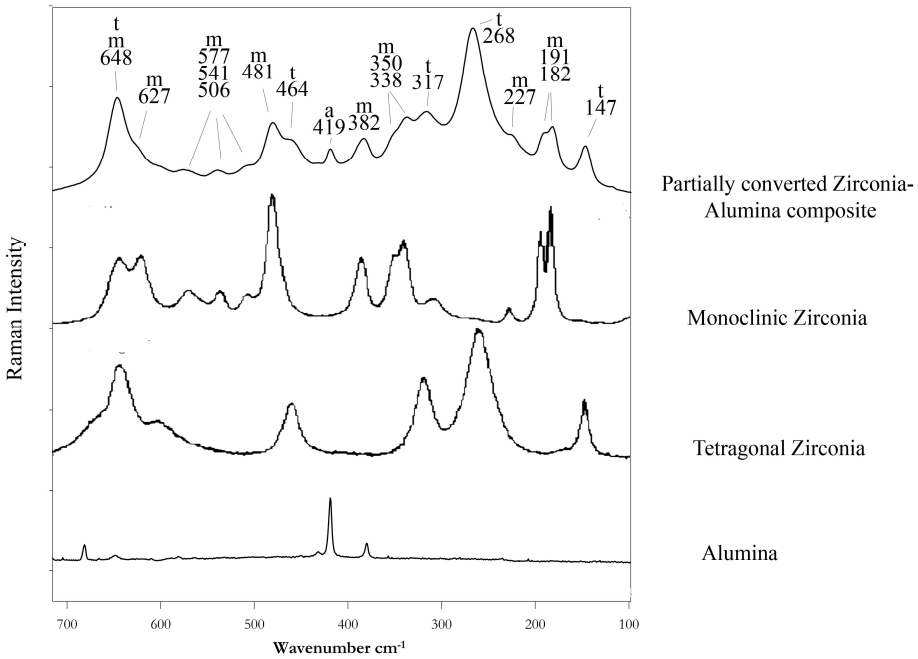

Figure 10.1: Raman spectra of the crystalline phases present in the composite.

With the exception of the weak band at 419 cm^{-1} ascribable to alumina [12], all the observed bands, assigned according to the literature [13,14], were due to the Raman scattering of tetragonal and monoclinic zirconia polymorphs.

The marker bands of tetragonal zirconia at 648, 464, 317, 268 and 147 cm^{-1} together with those due to the monoclinic polymorph at 627, 577, 541, 506, 481, 382, 350, 338, 227, 191 and 182 cm^{-1} were detected.

Figures 10.2 and 10.3 show the average micro-Raman spectra recorded on the unworn control and worn surfaces of retrievals #2 and #4, implanted in 2003 and 2007, respectively.

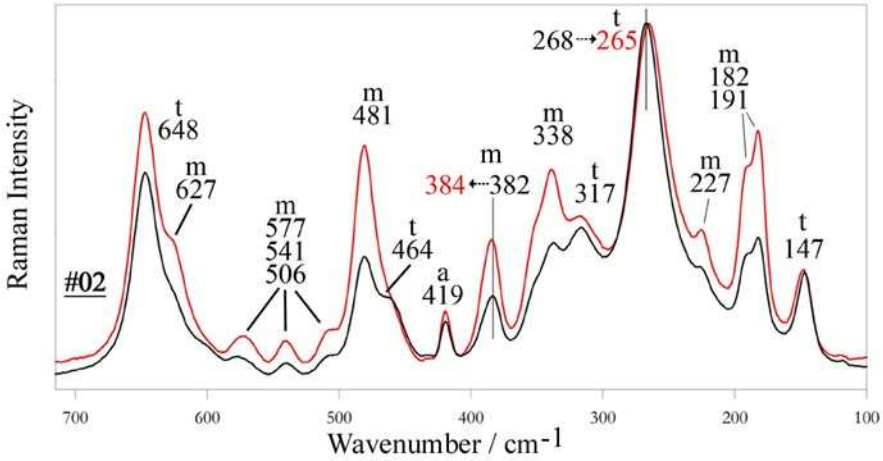

Figure 10.2: Average micro-Raman spectra recorded in the unworn control area (black) and worn region (red) of retrieval #2 (dated back to 2003, follow-up 5 years). The bands assigned to tetragonal zirconia (t), monoclinic zirconia (m) and alumina (a) are reported.

Upon wear, the t-m transformation increased the monoclinic zirconia content inducing significant spectral changes: the worn area of the retrievals #2 (Figure 10.2) showed a significant strengthening of the bands due to monoclinic zirconia. At the same time, some bands underwent significant wavenumber shifts and broadening; this is the case of the spectral components observed in the unworn region at 268 cm^{-1} (tetragonal) and 382 cm^{-1} (monoclinic) which shifted to 265 and 384 cm^{-1}, respectively, in the worn area.

The effect of wear was significantly less pronounced in retrieval #4 (Figure 10.3), more recently implanted; no significant shifts in the above mentioned bands were observed.

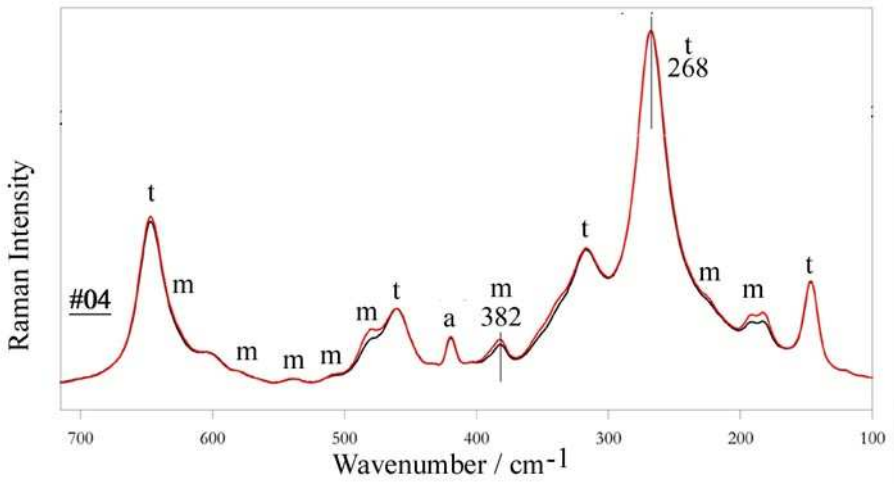

Figure 10.3: Average micro-Raman spectra recorded in the unworn control area (black) and worn region (red) of retrieval #4 (dated back to 2007, follow-up 2 years). The bands assigned to tetragonal zirconia (t), monoclinic zirconia (m) and alumina (a) are reported.

It is interesting to note that the fracture of the femoral head induced evident changes in the above described spectral features, even more pronounced than in retrieval #2. The average micro-Raman spectrum recorded in the section of the F5 fragment showed with the highest intensity the bands due to monoclinic zirconia. Moreover the above mentioned bands at 268 and 382 cm^{-1} significantly shifted in wavenumber values and broadened, due to the undergone stress.

Figure 10.4 shows the comparison of the micro-Raman spectra recorded before and after the intentionally *in vitro* breaking of a new femoral head.

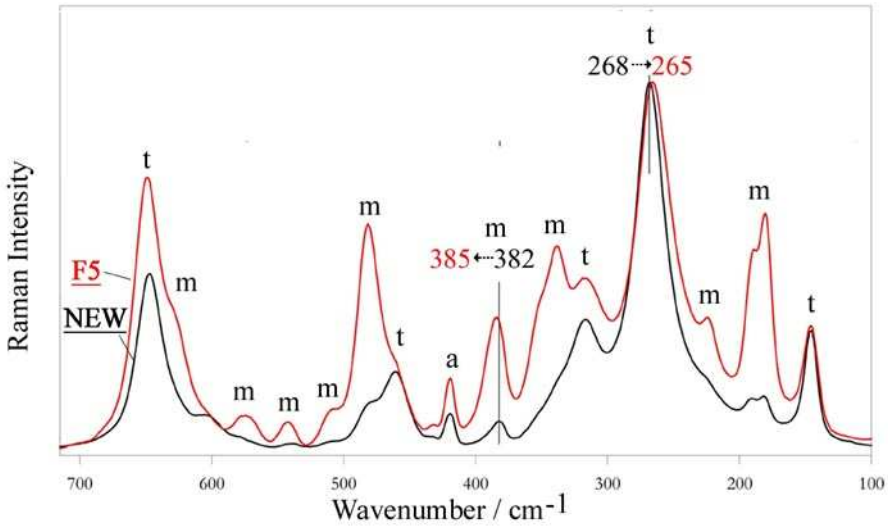

Figure 10.4: Average micro-Raman spectrum recorded in the section of the F5 fragment (red) obtained by intentionally *in vitro* breaking a new femoral head dated back to 2009 (black). The bands assigned to tetragonal zirconia (t), monoclinic zirconia (m) and alumina (a) are reported.

The bands at 147 and 191-182 cm^{-1} allowed to calculate the V_m monoclinic volume fraction, according to the Katagiri equation. The obtained results are reported in Figure 10.5.

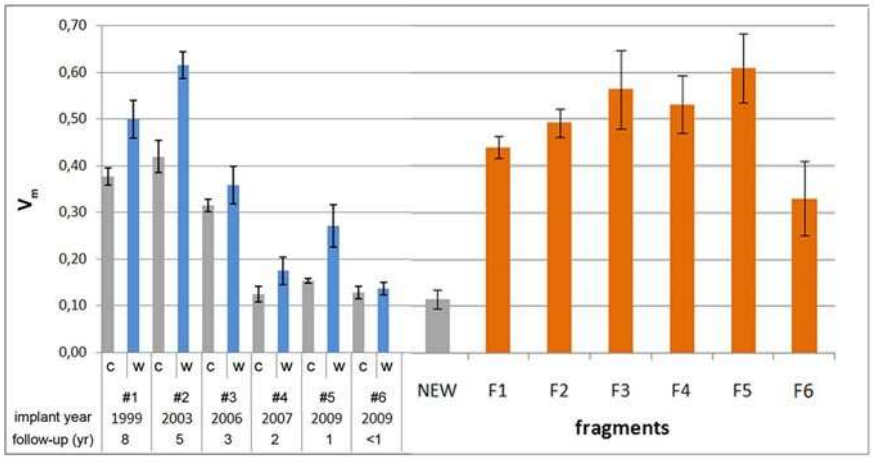

Figure 10.5: Average monoclinic zirconia volume fraction (V_m) data as obtained from the micro-Raman spectra recorded in the control unworn (c, grey), worn regions (w, blue) of

the analysed retrievals and in the sections of the six fragments obtained by intentionally *in vitro* breaking a new femoral head dated back to 2009. The V_m value of a new unworn sample dated back to 2009 is reported for comparison.

The monoclinic volume fraction calculated in the unworn region of the sample #2 was 0.42 ± 0.03: upon wear, a noticeable increase in the V_m value (0.62 ± 0.03) was observed.

Sample #4 appeared characterised by significantly lower V_m values in both unworn and worn regions (0.13 ± 0.02 and 0.17 ± 0.03, respectively) in agreement with the less pronounced spectral changes.

On the other hand, the pronounced variation of the spectral features observed in Figure 10.4 was confirmed by the strong increase of the V_m values upon fracture: an increment from 0.11 ± 0.02 (new femoral head) to 0.61 ± 0.07 was observed.

Figure 10.6 shows the trend of the wavenumber position and FWHM of the bands most significantly shifted upon wear as a function of the monoclinic content (V_m).

The wavenumber position of the bands at about 268 cm^{-1} (tetragonal) and 382 cm^{-1} (monoclinic) and their FWHM well correlated with the V_m value calculated both in the retrievals (unworn control and worn regions) and the sections of the fragments of the *in vitro* fractured component. The slope of the regression lines reported in Figure 10.6 was of the same order of magnitude for the two sets of samples, excepted than for the FWHM of the band at about 382 cm^{-1}: this spectral feature increased with V_m more steeply in the retrievals than in the section of the fragments.

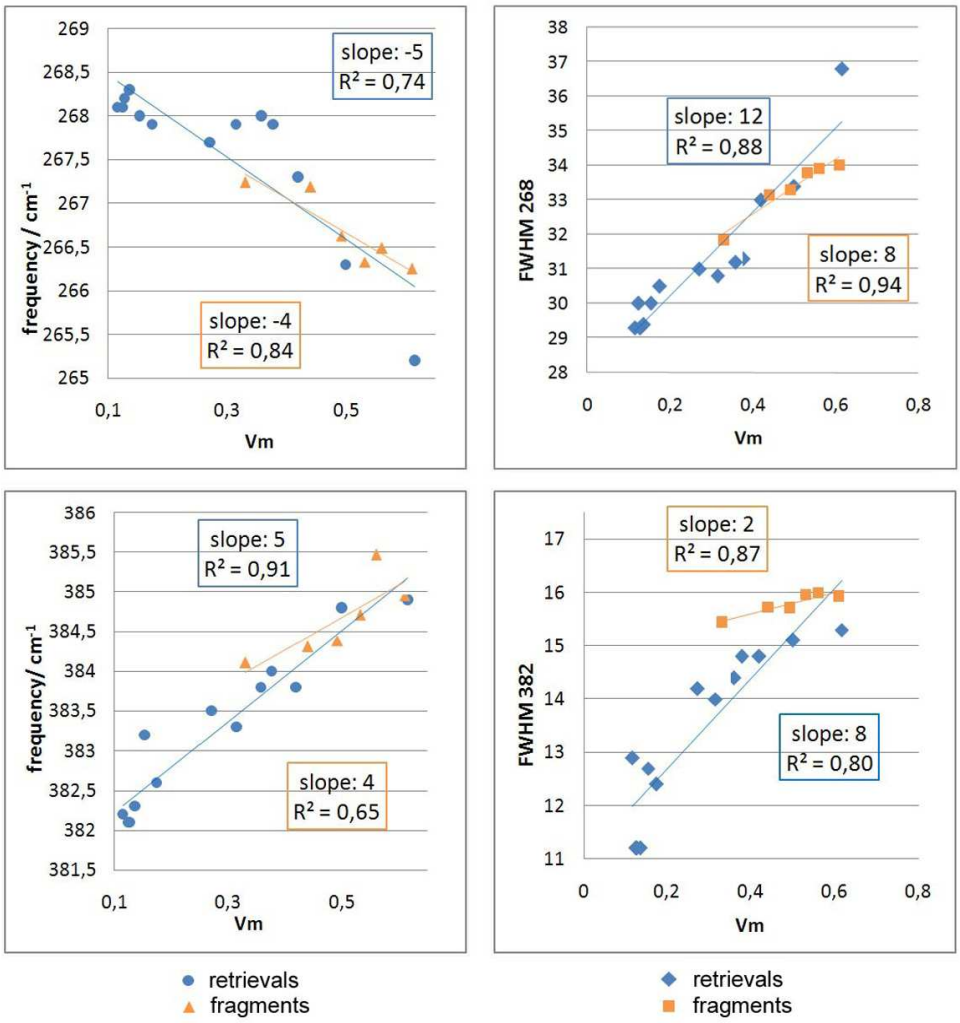

Figure 10.6: Trend of the wavenumber position and FWHM of the bands at about 268 cm^{-1} (tetragonal zirconia) and 382 cm^{-1} (monoclinic zirconia) as a function of the monoclinic content (V_m). Blue symbols refer to the data obtained in the control unworn and worn regions of the analysed retrievals; orange symbols refer to the data obtained in the sections of the six fragments analysed (*in vitro* fractured head).

Optical images of the articulating surface topography of two areas belonging to the *in vitro* fractured head are shown in Figure 10.7A-B. Figure 10.7C shows the trend of the monoclinic volume fraction (V_m) as a function of the distance from the fracture edge in six different areas of the fragment inspected by Raman spectroscopy.

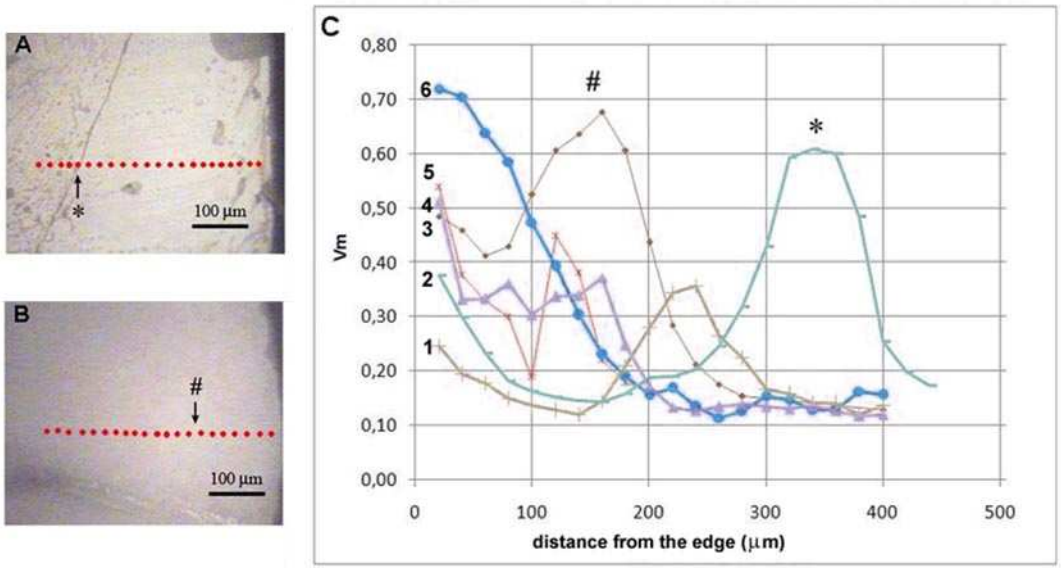

Figure 10.7: (**A**) and (**B**): Optical images of the articulating surface topography of two areas belonging to the fragment inspected by Raman spectroscopy (*in vitro* fractured head). The red points indicate where Raman spectra were taken (i.e. at steps of 20 µm moving orthogonally to the fracture edge). (**C**): Trend of the monoclinic volume fraction (V_m) as a function of the distance from the fracture edge in six different areas (numbered from 1 to 6) of the fragment inspected by Raman spectroscopy.

The *in vitro* fracture of the new femoral head induced significant changes in the V_m values also on the surface of the sample. As can be easily seen from the graph, V_m did not monotonically decrease going away from the edge of the fracture, but often reached a maximum.

Fluorescence spectra

Figure 10.8 reports the full-width at half-maximum (FWHM ± standard deviation) of the R_1 and R_2 bands as obtained from the fitting of the fluorescence spectra of the retrieval #4, here reported for the first time, the new femoral head (control) and the sections of the six

fragments of the *in vitro* fractured head. The values corresponding to the other retrievals are reported in Figures 9.3 and 9.4.

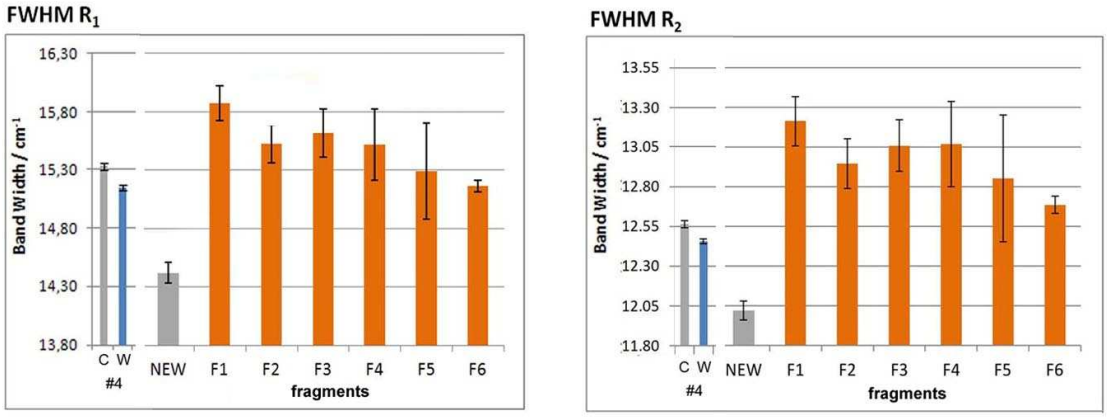

Figure 10.8: Average full-width at half-maximum (FWHM ± standard deviation) of the R_1 and R_2 bands as obtained from the fitting of the fluorescence spectra of the retrieval #4, the new femoral head dated back to 2009 and the sections of the six fragments (*in vitro* fractured head).

As can be seen from the histograms, the worn areas of both the retrievals and fragments showed significant differences in the FWHM of the R_1 and R_2 bands if compared with their respective control areas, while no wavenumber shifts in any of the analysed samples were observed. As discussed in the previous chapter, from a general point of view, the standard deviation associated to the mean FWHM values of both R_1 and R_2 bands in the worn areas was often higher than in the control areas, indicating a higher dispersion due to wear.

Figure 10.9 shows the optical images of the surface appearance of the new femoral head and the F2 and F5 fragments.

Figure 10.9: Optical images of the surface appearance of the new femoral head and the F2 and F5 fragments.

The standard deviation increase can be related to the surface appearance of the samples; comparing Figures 10.8 and 10.9, it appeared that the homogeneous surface finishing typical of a new femoral head results in a low standard deviation associated to the corresponding measurements, while the worsening of the surface finishing in fragment F2 (and even more in fragment F5) determined a progressive increase in the standard deviation associated to the corresponding measurements.

Upon wear all the retrievals (with the only exception of sample #4) and all the fragments showed a general increase of the FWHM of both R_1 and R_2 bands with respect to the control regions.

Figure 10.10 shows the trend of the FWHM of the R_1 and R_2 fluorescence bands as a function of the monoclinic content (V_m) obtained by Raman spectroscopy.

The FWHM of both the fluorescence bands are correlated with the V_m values obtained by Raman spectroscopy both in the retrievals (unworn control and worn regions) and the sections of the fragments of the *in vitro* fractured component. A better correlation was obtained for the R_1 band; the slopes of the two regression lines were practically the same for the two R_1 and R_2 bands.

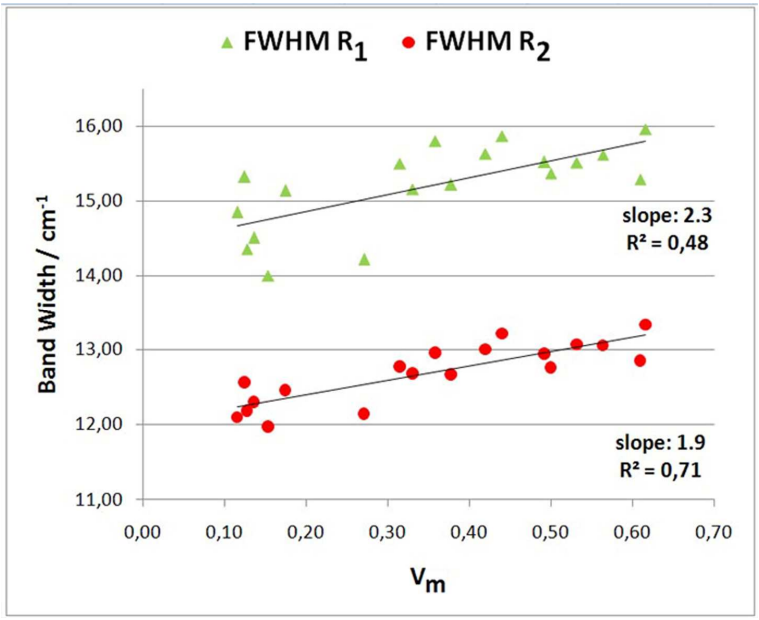

Figure 10.10: Trend of the FWHM of the R1 and R2 fluorescence bands as a function of the monoclinic content (V_m) obtained by Raman spectroscopy.

Raman spectroscopy has been widely used for investigating the mechanism of the t-m transformation. The Mehl-Avrami-Johnson law has been found to correctly describe the dependence of the V_m monoclinic content on ageing time [8,9,11]:

$$V_m = 1 - (1 - V_m^o) \exp - (bt)^n$$

where t is the ageing time, b is a parameter that depends on both growth and nucleation rates of the monoclinic nuclei, V_m^0 is the fraction of monoclinic phase in the material at the beginning of the ageing test, and n is an exponent that was found to range between 0.3 and 4.

In Figure 10.10, $\ln(\ln(1-V_m^o / 1-V_m))$ was plotted against ln(t) according to the above reported equation, where t was the follow-up and V_m and V_m^0 were the values of the monoclinic volume fraction in the worn and unworn control areas of each retrieval, respectively. The n value was calculated as the slope of the best regression line obtained from the experimental data and was found to be 0.60.

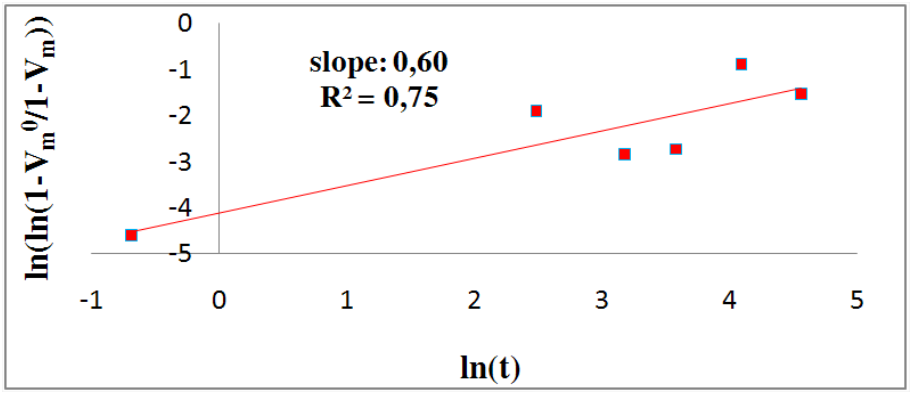

Figure 10.11: Plot of ln(ln(1-V_m^o /1-V_m)) *versus* ln(t), where V_m^o and V_m were the average data obtained from the Raman spectra of the worn and unworn areas of the Biolox® *delta* retrievals

As reported by previous studies [15], n values close to 4 reveal a preponderant contribution to the kinetics of transformation from the growth of pre-existing monoclinic nuclei, while the nucleation rate is dominant at small n values. A value between 3 and 4 indicates a nucleation and 3D-growth behaviour and was observed for unconstrained zirconia (3Y-TZP), where no matrix prevents the transformation [16]. A value of 1, according to the Mehl-Avrami-Johnson law [17], refers to nucleation only. As previously observed by Deville *et al.* [16], values as low as that observed in the present study would suggest that the growth stage is absent and the nucleation stage is not occurring as freely as it would in unconstrained zirconia: the alumina matrix prevents the propagation of the transformation as well as the nucleation of the monoclinic phase.

10.4 Discussion

Raman spectroscopy was used to monitor the monoclinic zirconia content in the six analysed Biolox® *delta* retrievals. It is well known that the t-m transition compromises the mechanical strength of the material [15,3] as well as its long term lifetime and stability

[16,18]. Moreover, water may trigger the transformation *in vivo*, so that both wear and hydrothermal degradation could increase the transition rate.

For this reason, the study of the monoclinic zirconia content is of key importance in the study of zirconia-based ceramics.

Figure 10.2 shows the V_m values obtained on the unworn and worn regions of the retrievals under study. The unworn control area of the most recent retrievals (i.e. #4, #5 and #6) was characterised by V_m values very close to that obtained for a new femoral head dated back to 2009 (0.13 ± 0.02). This result helps us to clarify the role of the *in vivo* environment in the occurrence of the t-m transformation and suggests that the *in vivo* permanence of the implant for 2 years at least (i.e. for the time corresponding to the most durable femoral head, i.e. #4) did not trigger to significant extents a material degradation.

This result is in agreement with the earlier studies on Biolox® *delta* femoral heads in which the authors did not report any significant t-m phase transformation after environmental exposure to water vapor [6,7]. Moreover, on the basis of our result, it can be assumed that the unworn border of the retrievals was a suitable control area for comparison.

The data reported in Figure 10.2 indicate that the monoclinic zirconia content is different in Biolox® *delta* samples implanted (and reasonably manufactured) in different years. The V_m values obtained from the spectra recorded in the unworn control region of the retrievals ranged between 0.31 ± 0.01 and 0.42 ± 0.03 (i.e. between 31 and 42 vol%) until 2006 (retrievals #1, #2 and #3) and decreased to about 0.1 (i.e. 10 vol %) since 2007. These findings indicate that the manufacturer progressively improved the material composition, attaining progressively lower monoclinic zirconia contents.

This hypothesis was confirmed by the comparison with the Raman results reported by Pezzotti *et al.* on a new Biolox® *delta* femoral head dated back before 2006 [8]. The Raman spectrum reported by these authors showed the bands of the monoclinic zirconia

phase significantly stronger than in the spectrum reported in Figure 10.4 for our new femoral head dated back to 2009. The aforementioned authors have quantified the monoclinic content of their new Biolox® *delta* femoral head according to Clarke and Adar [11] and have reported a value of about 20 vol%. Considering that the method by Clarke and Adar underestimates the monoclinic zirconia content, as reported by other authors [10], the amount of this phase should have been even higher and in agreement with our data.

The V_m data obtained on the worn areas of the retrievals (Figure 10.2) allowed to clarify the role of wear in the t-m phase transformation; actually, Ma and Rainforth [19] have demonstrated the occurrence of tribochemical wear in Biolox® *delta* components subjected to reciprocating sliding wear tests. The earliest components, in particular retrievals #1 and #2 (i.e. those characterised by the highest monoclinic contents in the control area), showed a significant increase in the V_m values upon wear, suggesting that the stress generated at the articulating surface caused a t-m phase transformation. However, it is interesting to note that an analogous behaviour was observed also for retrievals #4 and #5, which were characterised by lower V_m values in their unworn control areas. On the contrary, no significant increase in the V_m value was observed in the retrieval #6, due to its short implant time (1 month). The results reported in the present study would suggest that the t-m phase transformation was mainly due to wear rather than *in vivo* ageing. In the light of the above reported results, Raman spectroscopy proved a valid tool to investigate on a microscopic level the surface deterioration of retrieved Biolox® *delta* femoral heads upon wear. Besides quantifying the t-m phase transformation, this technique proved suitable to characterize the associated residual stresses stored within the tetragonal and monoclinic zirconia phases. Previous studies have established a clear correlation between the degree of phase transformation and the residual stress magnitude, [20,21] which is in turn related to

wear. According to the above mentioned piezospectroscopic effect, some Raman bands underwent significant frequency shifts and broadening upon wear. As can be seen in Figures 10.3 and 10.5, the bands that showed the most pronounced changes were located at about 268 cm^{-1} (tetragonal zirconia) and 382 cm^{-1} (monoclinic zirconia); their wavenumber position and FWHM were found to linearly change with the V_m value (Figure 10.6). Actually, since the phase transformation induces a volume increase in the monoclinic crystals, the higher the percentage of transformed phase the higher the residual stress in the system. From this point of view, V_m can be considered an index of the residual stress magnitude. The data reported in Figure 10.6 showed that both the considered bands underwent a FWHM increase with increasing V_m values. On the contrary, their wavenumber position displayed a different trend with increasing V_m: the components at 382 cm^{-1} shifted to higher wavenumber values, while the 268 cm^{-1} band downwards in agreement with another study [22].

With regard to the transformation involved in the potential prosthesis break, in 2010, Lombardi *et al.* have reported the case of a fractured Biolox® *delta* femoral head which showed a 33% monoclinic transformation and an increase in surface roughness [23].

The data presented shows that the *in vitro* fracture of a new Biolox® *delta* femoral head induced even more dramatic V_m changes, both on the articulating surface (Figure 10.7C) and in the sections (Figures 10.2 and 10.5) of the analysed fragments. The data reported in Figure 10.7C showed that the surface extension of the t-m transformation was significantly higher than that reported by other authors [11] who have observed a faster decrement of the monoclinic content (within few microns) moving from the edge. The Raman spectra recorded in the section showed that a significantly more extended region is interested by the t-m transformation (tens-hundreds of microns); a number of inspected areas showed a maximum in the V_m trend at several micrometers from the edge (Figure 10.7C).

Sometimes, this maximum coincides with a crack on the articulating surface (area 2, see Figure 10.7A), in other cases it did not (area 3, see Figure 10.7B); in the latter area, the large amount of monoclinic phase (V_m about 0.65) at about 150 μm from the edge (Figure 4C) could be ascribed to the propagation of the t-m conversion from the fracture edge.

With regard to the kinetics aspects of the t-m trasformation the n value found (0.60) by the plotting of $\ln(\ln(1-V_m^o /1-V_m))$ *versus* ln(t) (Figure 10.11) was in good agreement with that obtained by Pezzotti *et al.* (i.e. 0.68)[8] and Chevalier *et al.* (i.e. 0.78) [9] for accelerated *in vitro* ageing treatments in autoclave. On the basis of this agreement, the *in vitro* accelerated ageing protocols proposed in the literature to simulate the effects of the *in vivo* wear can be considered validated.

The results obtained on the FWHM of the R_1 and R2 fluorescence bands reflected the Raman data. From a quantitative point of view, the good agreement between fluorescence and Raman data was confirmed by the graphs reported in Figure 10.10; the areas characterized by higher contents of monoclinic zirconia showed broader fluorescence bands (i.e. higher FWHM values). Actually, the trend of the FWHM of both R_1 and R_2 fluorescence bands (Figures 9.3, 9.4 and 10.8) was very similar to that observed for the V_m values (Figure 10.2), although the retrieval #4 showed a different behaviour. With regards to the unworn control region of the retrievals, the earliest retrievals were characterised by significantly higher FWHM of both the bands than the most recent ones (Figures 9.3, 9.4 and 10.8), according to the V_m data (Figure 10.2). In the worn region of all the retrievals except #4, a significant increase in these parameters was observed (Figures 9.3, 9.4 and 10.8); a higher FWHM is indicative of a wider range of residual stress values [24]. On the contrary, in the worn area of the retrieval #4, both R_1 and R_2 bands sharpened upon wear; micro-cracking could be a possible explanation for this trend.

As shown in Figure 10.8, both R_1 and R_2 bands of the fluorescence spectra recorded in the section of the fragments of the *in vitro* fractured head underwent a significant broadening.

10.5 Conclusions

Fluorescence and Raman spectroscopy proved valid tools to investigate the material properties of Biolox® *delta* femoral heads as well as their changes upon *in vivo* wear. The obtained results showed that a progressive improvement of the material properties has occurred in the period comprised between 1999 and 2009.

The data here presented showed that wear was the main cause of the t-m zirconia transformation for the considered retrievals; the *in vivo* permanence for two years at least did not definitely increase the monoclinic content of Biolox® *delta* components.

The Raman results obtained validated the *in vitro* accelerated ageing protocols proposed in the literature to simulate the effects of the *in vivo* wear, because the mechanism operating *in vivo* was found to be the same active *in vitro*.

The *in vitro* fracture of a new femoral head appeared to be an extreme wear condition that determined the most significant changes in the residual stress state and monoclinic content both in the section of the fragments and on their surface. The micro-Raman mapping of the articulating surface showed that the t-m transformation involved a region much more extended than as reported in the literature.

10.6 References

1. J. Li, G. W. Hastings, in *Biomaterial Properties*, (Eds.: J. Black, G. Hastings), Chapman & Hall,London, 1999, pp. 341-354.

2. G. Willmann. *Orthopedics* 1998, **21,** 173.

3. J. Chevalier. *Biomaterials* 2006, **27,** 535.

4. S. Deville, J. Chevalier, C. H. Dauvergne, G. Fantozzi, J. F. Bartolome, S. Moya, R. Torrecillas, J. T. Sato, M. Shimada. *J. Am. Ceram. Soc.* 1985, **68,** 356.

5. I. Clarke, M. Manaka, D. D. Green, *J. Bone Joint Surg. Am.* 2003, **85,** 73.

6. W. Burger, H. G. Richter, *Key Eng. Mater.* 2001, **192-195,** 545.

7. G. M. Insley, R. M. Streicher, *Key Eng. Mater.* 2004, **192-195,** 781.

8. G. Pezzotti, K. Yamada, S. Sakakura, R. P. Pitto, *J. Am. Ceram. Soc.* 2008, **91,** 1199.

9. J. Chevalier, S. Grandjean, M. Kuntz, M. Pezzotti, *Biomaterials* 2009, **30,** 5279.

10. J. A. Muñoz Tabares, M. J. Anglada, *J. Am. Ceram. Soc.* 2010, **93,** 1790.

11. D. R. Clarke, F. Adar, *J. Am. Ceram. Soc.* 1982, **65,** 284.

12. S. P. S. Porto, R. S. Krishnan, J. Chem. Phys. 1967, **47,** 1009.

13. C. M. Philippi, K. S. Mazdiyasni, *J. Amer. Ceram. Soc.* 1971, **54,** 254.

14. M. Ishigame, T. Sakurai, *J. Amer. Ceram. Soc.* 1977, **60,** 367.

15. J. Chevalier, B. Cales, J. M. Drouin, *J. Am. Ceram. Soc.* 1999, **82,** 2150.

16. S. Deville, J. Chevalier, C. H. Dauvergne, G. Fantozzi, J. F. Bartolome, S. Moya, R. Torrecillas, *J. Am. Ceram. Soc.* 2005, **88,** 1273.

17. J. W. Christian, The theory of transformation in metals and alloys, Pergamon Press, Oxford, UK,1965.

18. J. Chevalier, L. Gremillard, S. Deville, *Annu. Rev. Mater. Res.* 2007, **37,** 1.

19. L. Ma, W. M. Rainforth, *Trib. Int.* 2010, **43,** 1872.

20. I. C. Clarke, G. Pezzotti, S. Sakakura, N. Sugano, *Key Eng. Mater.* 2003, **240-242,** 777.

21. B. Dietrich, K. F. Dombrowski, *J. Raman Spectrosc.* 1999, **30,** 893.

22. G. Pezzotti, A. A. Porporati, *J. Biomed. Optics* 2004, **9,** 372.

23. A. V. Lombardi Jr, K. R. Berend, B. E. Seng, I. C. Clarke, J. B. Adams, *Clin. Orthop. Relat. Res.*2010, **468,** 367.

24. M. A. Garcia, S. E. Paje, J. Llopis, *Mater. Sci. Eng.* 2002, **A325,** 302.